Universität Rostock
Traditio et Innovatio

Quantum Optical Measurement of Arbitrary Fourth-Order Field Moments via Balanced Homodyne Correlation

Dissertation submitted to the Faculty of Mathematics and Natural Sciences of the University of Rostock in fulfilment of the requirements for the degree of doctor rerum naturalium

by Milena Gödecke, born on August 19th, 1995 in Bremerhaven, Germany

Supervised by Prof. Dr. rer. nat. Boris Hage, University of Rostock

Rostock, April 17th, 2025

https://doi.org/10.18453/rosdok_id00005556

Gutachter:
Prof. Dr. Boris Hage, Universität Rostock, Institut für Physik
Prof. Dr. Janik Wolters, Deutsches Zentrum für Luft und Raumfahrt e.V. (DLR Berlin), Institut für Optische Sensorsysteme

Einreichung: 17.04.2025
Verteidigung: 07.08.2025

Abstract

Balanced homodyne correlation (BHC) allows the measurement of moments of creation and annihilation operators with unequal or equal powers. In contrast to previous homodyne correlation methods a strong local oscillator can be used, increasing signal to noise ratio and giving access to higher order moments. These moments are required in the study of general correlation properties and have applications in nonclassicality criteria. As in previous correlation methods, the detection efficiency only acts as a scaling factor, making BHC particularly suited for scenarios where losses are unavoidable.

In this work we implement balanced homodyne correlation measurements for the first time. Our realisation with eight detectors gives access to field moments up to fourth order. We create the required beam splitter cascade in a stable and compact waveguide chip with femtosecond laser writing, and use a photodiode array to detect the tightly spaced outputs. We verify our set-up with squeezed states and coherent states. The measured correlation moments scale with squeezing strength as theoretically predicted and exhibit the expected loss behaviour. Measurements with coherent states show the correlation moments to be independent of coherent displacement.

Kurzzusammenfassung

Mit der *balancierten Homodynkorrelation* (BHC) können Momente von Vernichtungs- und Erzeugungsoperatoren mit ungleichen oder gleichen Potenzen gemessen werden. Im Unterschied zu vorherigen Homodynkorrelations-Methoden kann ein starker Lokaloszillator verwendet werden, wodurch das Signal-zu-Rausch-Verhältnis erhöht wird und höhere Moment zugänglich werden. Diese Momente werden für die Untersuchung allgemeiner Korrelationseigenschaften benötigt und können in Nichtklassizitäts-Kriterien verwendet werden. Wie bei vorherigen Korrelationsmethoden wirkt die Detektionseffizienz nur als Skalierungsfaktor, so dass BHC besonders geeignet ist für Szenarien in denen Verluste unvermeidbar sind.

In dieser Arbeit werden balancierte Homodynkorrelations-Messungen zum ersten Mal realisiert. Mittels unserer Umsetzung mit acht Detektoren können Feldmomente bis zur vierten Ordnung gemessen werden. Die benötigte Strahlteiler-Kaskade wird mit einem Femtosekundenlaser direkt in einen stabilen und kompakten Wellenleiterchip geschrieben. Zur Detektion der acht eng beieinanderliegenden Ausgänge verwenden wir ein Photodioden-Array. Zur Überprüfung unseres Aufbaus verwenden wir gequetschte Zustände und kohärente Zustände. Die gemessenen Korrelationsmomente skalieren mit dem Quetschgrad gemäß der theoretischen Vorhersage und zeigen das erwartete Verlustverhalten. Messungen mit kohärenten Zuständen zeigen, dass die Korrelationsmomente unabhängig von der kohärenten Verschiebung sind.

Contents

List of Acronyms

AC Alternating Current

AR Anti-Reflection

BHC Balanced Homodyne Correlation

BHD Balanced Homodyne Detection

DC Direct Current

DMA Direct Memory Access

EOM Electro-Optic Modulator

FIFO First-In-First-Out

FPGA Field Programmable Gate Array

HBT Hanbury Brown and Twiss

HR High-Reflection

LO Local Oscillator

ND Neutral Density

OPA Optical Parametric Amplifier

PBS Polarising Beam Splitter

PCB Printed Circuit Board

PDH Pound-Drever-Hall

PPKTP Periodically Poled Potassium Titanyl Phosphate

SMD Surface-Mounted Device

VI Virtual Instrument

1. Introduction – From Radio Stars to Balanced Homodyne Correlation

In 1932 the physicist and radio engineer Karl Jansky investigated the origins of radio frequency static which might interfere with radio communications. The signals seemed to fall into three groups. The signals in the first two groups came from near or distant thunderstorms, while the origin of the "steady hiss type static" in group three remained unknown [Jan32; Jan33]. The signal seemed to come from a fixed position in the center of the Milky Way galaxy and soon over a hundred sources of extraterrestrial radio-frequency radiation were identified. Their investigation, however, remained an issue. With radio wavelengths orders of magnitude longer than optical wavelengths, the resolution of available astronomical interferometers was suspected to not suffice to measure the angular diameter of the radio stars. The astronomers Hanbury Brown, Jennison and Das Gupta proposed and successfully tested a new type of interferometer, in which the intensities from two antennas would be correlated, rather than interfering their amplitudes. In this case the signal running between the antennas could be conveyed over a longer distance, allowing a higher resolution [HJG52; HT54].

If it was possible to measure the size of *radio* sources by intensity correlation, however, why would it not be possible to apply the same method to *optical* stars, using photomultiplier tubes instead of radio-frequency detectors? Correlations in the arrival of photons had not been studied, so Hanbury Brown and Twiss conducted a laboratory experiment first, in which they split the light from a mercury-vapor lamp into two coherent beams and measured their intensity fluctuations with photomultiplier tubes. They found strong positive correlations between the noise signals and concluded that the arrival of photons in coherent beams was correlated and the correlation was preserved during detection [HT56a]. Soon after, they built an optical stellar intensity interferometer and successfully measured the angular size of Sirius [HT56b].

At the same time new sources of microwave and optical radiation, the maser and later the laser [ST58; Mai60], made unprecedented levels of coherence available which enabled the new field of nonlinear optics [Fra^{+}61; Boy08]. To account for the newly found correlations and the new levels of coherence Roy Glauber developed a "Quantum Theory of Optical Coherence" [Gla63a], allowing the description and characterisation of n-fold photon coincidence experiments and n-th order coherence using correlation functions of normally ordered complex field strength operators. In a follow-up paper he gave quantum optical explanations for the statistical properties of different light sources [Gla63b], including the bunching effect Hanbury Brown and Twiss observed for a thermal light source.

Correlation functions and photon coincidence measurements have become corner stones of quantum optics. In 1977 Kimble et. al. have used photon coincidence counting to show the *anti-bunched* emission of photons from sodium atoms undergoing resonance fluorescence, a purely quantum mechanical effect with no classical explanation [KDM77]. Further, criteria for nonclassicality based on correlation functions were developed [AT92]. Here the hallmark quantum feature of a narrower than Poissonian photon number distribution (sub-Poissonianity) as described by the Mandel Q Parameter [Man79] was generalised. Photon coincidence methods are also used as standard tools in the preparation and characterisation of sources of single photons [DW87; Mic$^+$00; San$^+$02], photon pairs [BW70; HOM87], and multi-photon states [OSu$^+$08] (see also [LO05; Lai$^+$22] for review articles).

Next to coincidence counting and effects such as anti-bunching and sub-Poissonianity, which relate to the countable and discrete particle nature of light, there are measurements and nonclassical effects associated with the continuous wave nature of light. Even in a vacuum state, i.e. when the expected photon number is zero, small amplitude fluctuations exist. These so-called vacuum fluctuations are a fundamental feature of the quantised field. For the vacuum field, or the field generated by an ideal laser, the vacuum fluctuations carry the same magnitude independent of phase. While it is not possible to remove the vacuum fluctuations altogether, their magnitude can be rearranged between conjugate quadratures, i.e. typically between the amplitude and the phase of the wave, allowing higher-than-vacuum-level precision in one of them, at the expense of increased uncertainty in the other. This feature is realised in the highly nonclassical quadrature squeezed state [Yue76]. Soon after its proposal methods were developed to generate and measure squeezing.

Homodyne detection, in which the signal field to be measured is combined with a coherent local oscillator (LO) field of the same frequency at a beam splitter [SYM79], already allowed phase selective measurement of quadrature variance, but suffered from LO excess noise. This limitation was overcome in balanced homodyne detection (BHD), in which both outputs of the beam splitter are measured and subtracted [YC83]. Thereby LO noise is suppressed, enabling quadrature fluctuation measurements with high signal to noise ratio (SNR) and thus the detection of squeezing.

Slusher et. al. demonstrated weak squeezing from four wave mixing using sodium atoms in 1985 [Slu+85], and Wu et. al. showed 3 dB of squeezing from degenerate parametric down conversion soon after in 1986 [Wu+86]. A bridge from wave properties to particle properties can be found in the determination of correlation moments from quadrature measurements using pattern functions [Ric96] and in the determination of time dependent correlation functions from double BHD measurements [Gro+07].

A bridge in the other direction, from correlation measurements to field properties, was found by Ou et. al. in their proposal to measure squeezing by a correlation experiment [OHM87]. In the scheme nowadays often called *homodyne cross correlation* the signal to be measured is combined with a LO and measured by two detectors similar to BHD, but instead of taking the difference of the photocurrents the signals are multiplied. As a result uncorrelated detector noise does not affect the squeezing measurement. A very similar scheme, nowadays often labeled *homodyne intensity correlation*, was proposed by Vogel to measure the weak squeezing from the resonance fluorescence of a single trapped ion, where detection efficiencies are low [Vog91]. Next to the measurement of squeezing also *anomalous moments* of intensity-amplitude correlations, and sub-Poissonian statistics would be measured simultaneously and could be separated due to their different dependencies on the LO phase. An in-depth analysis and comparison of both homodyne correlation methods was published soon after [Vog95], pointing out that in these methods less-than-unity detection efficiencies only act as a multiplicative factor. This poses a considerable advantage over BHD in cases of limited efficiency, since in BHD imperfect detection leads to a convolution of the measured field strength distribution with Gaussian noise, so that finer quantum features are lost. A shared disadvantage of the homodyne correlation methods is, however, that classical noise of the local oscillator is not cancelled out. Therefore these methods were discussed for weak local oscillators on the order of the signal field strength only, limiting access to higher order moments. [SV06].

Anomalous intensity-amplitude correlations, also referred to as wave-particle correlations, have as well been investigated in conditional homodyne detection [Car+00], in which a balanced homodyne measurement is performed conditionally upon the detection of a photon. It has been used to observe the time evolution of the field radiated by single atoms undergoing Rabi oscillations after the emission of a photon [Fos+00; Fos+02; Ger+09].

The homodyne cross correlation scheme was used for the electronic-noise free measurement of squeezing from the optical Kerr effect and parametric down conversion [Kri+08; Kri+09].

Homodyne cross correlation measurements with an unbalanced beam splitter were used to prove nonclassicality of a phase quadrature squeezed state for nearly all phases, including phase regions where no squeezing is seen [Küh+17]. With the homodyne intensity correlation scheme both anti-bunching and squeezing were observed simultaneously in the light emitted by a quantum dot [Sch+15].

More complex homodyne correlation techniques tailored for nonclassicality characterisation have been developed, based on normally ordered moments of quadratures [SRV05], and based on different operator moments, including moments of creation and annihilation operators of equal or unequal powers [SV05].

Balanced homodyne correlation, a method proposed by Shchukin and Vogel in 2006, finally overcomes the weak-LO limitation of homodyne correlation methods [SV06]. While in BHD the influence of LO noise was eliminated by the subtraction of the photocurrents, here the same effect is reached by the alternating summation of the measured multi-detector correlations in a binomial scheme in the post-processing. With strong LOs allowed, the advantages of BHD and homodyne correlation are combined, enabling the measurement of moments of creation and annihilation operators with unequal or equal powers up to high orders, with strong signal to noise ratio. Similar to previous methods imperfect detection only acts as a scaling factor. The general correlation properties thus measurable have direct applications in the characterisation of nonclassicality [Vog08].

In this work we implement balanced homodyne correlation measurements for the first time[1]. We utilise femtosecond laser direct writing [Dav+96; Miu+97; SB01] to realise the required beam splitter cascade in a stable and compact waveguide chip, and detect the eight outputs with a photodiode array. Thereby moments of creation and annihilation operators up to fourth order, with equal or unequal operator powers, can be measured. We verify our set-up using amplitude quadrature squeezed light, proving that the measured correlation functions scale with squeezing strength as expected and show the anticipated loss behaviour. Using coherent states we show the measured noise correlation moments to be independent of coherent displacement.

In chapter 2 we give the theoretical basis for this work by introducing the quantised field and particular states of it, correlation functions as discussed by Glauber, and the theory of balanced homodyne correlation with an extension to the realistic experimental scenario. We will then describe our experimental set-up in chapter 3, in particular the waveguide chip, the photodiode-array detector and the multi-beam coupling. In chapter 4

[1] To the best of our knowledge.

we describe the correlation measurements performed with amplitude quadrature squeezed states and coherent states, explain our analysis process and discuss the results. Finally, in chapter 5, we summarise our work and give an outlook on future research opportunities enabled by our implementation of balanced homodyne correlation.

2. Theory

In this chapter we will introduce the quantum optical theory required for this work. We start from a classical, general solution of the free electromagnetic field, discuss differences arising from canonical quantisation and introduce Fock states, the coherent state and the squeezed state. Next, we will discuss elements of Glauber's quantum theory of optical coherence, from the ideal photon counter to (n-fold) coincidence measurement and correlation functions. A brief explanation of balanced homodyne detection will follow. We will then explain the balanced homodyne correlation scheme as proposed by Shchukin and Vogel, which allows the measurement of general correlation functions up to high orders. We will add the experimentalist's view to the picture, discussing the realistic case of non-ideal splitting ratios and uneven transmissions as well as the influence of losses in the signal beam. At last, we will calculate the correlation functions of squeezed vacuum states, which we will use as test states to verify our set-up.

2.1. Quantised Field of Light

We start our discussion with a discrete mode solution for the space and time dependent electric field vector $\mathbf{E}(\mathbf{r}, t)$ in free space

$$\mathbf{E}(\mathbf{r}, t) = i \sum_k \left(\frac{\hbar \omega_k}{2 \epsilon_0} \right)^{1/2} \left[a_k \mathbf{u}_k(\mathbf{r}) e^{-i\omega_k t} - a_k^* \mathbf{u}_k^*(\mathbf{r}) e^{i \omega_k t} \right], \tag{2.1}$$

which can be found from Maxwell's equations via mode expansion of the vector potential. Explicit derivations can be found in many standard textbooks of quantum optics, e.g. [WM08], which is used here.

The field is found by summation over all possible discrete modes k, with one mode being characterised by its frequency ω_k and a mode function $\mathbf{u}_k(\mathbf{r})$ containing both the spatial distribution of amplitude and phase, as well as the polarisation. The mode functions form a complete orthonormal set and fulfil the wave equation. They depend on the boundary conditions and both standing and travelling waves can be found from appropriate conditions [WM08].

So far we have made no explicit assumption whether the field is classical or quantum. If the amplitudes a_k and a_k^* are complex numbers, the field described will be classical, adding or subtracting a single photon will make no conceivable difference to the field and the order of doing so is irrelevant. The field exists as an isolated entity and we, the observer, are free to take measurements of the field strength and derived quantities without changing it. All of this is only possible in a domain in which the individual photon energy $\hbar\omega_k$ is insignificant with respect to the overall intensity of the field [Gla63a].

A quantised field is found if the amplitudes are chosen to be mutually adjoint operators $\hat{a}_k$ and $\hat{a}_k^\dagger$, obeying the bosonic commutation relations

$$\left[\hat{a}_k, \hat{a}_{k'}\right] = \left[\hat{a}_k^\dagger, \hat{a}_{k'}^\dagger\right] = 0, \qquad \left[\hat{a}_k, \hat{a}_{k'}^\dagger\right] = \delta_{kk'}. \tag{2.2}$$

Three different cases can be distinguished here. First, for two-fold application of the same operator $\hat{a}$ or $\hat{a}^\dagger$, the ordering is irrelevant, irrespective of which modes they apply to. Second, for operators relating to different modes, $\hat{a}_k$ and $\hat{a}_{k'}^\dagger$ commute. Third, if $\hat{a}_k$ and $\hat{a}_k^\dagger$ belong to the same mode, their commutator $[\hat{a}_k, \hat{a}_k^\dagger] = 1$ no longer vanishes, meaning their order of application matters.

As we will introduce in the next section, these operators are the annihilation and creation operators, subtracting or adding a photon to the field. Thereby, in the quantum scenario, the discrete nature of absorption and emission is considered, and further, their order is of relevance. Measurements, e.g. by photoabsorption, are no longer separate from the field in question.

The Hamiltonian of the field in Eq. (2.1) can be shown to be

$$\hat{H} = \sum_k \hbar\omega_k \left(\hat{a}_k^\dagger \hat{a}_k + \frac{1}{2}\right), \tag{2.3}$$

where the energies of the individual modes are summed up, with the energy in mode k given by the the photon energy $\hbar\omega_k$ multiplied by the number of excitations, which is the number of photons ($\hat{n}_k = \hat{a}_k^\dagger \hat{a}_k$) in mode k plus a half-excitation taking into account vacuum fluctuations inherent to quantised fields.

At last, we want to point out that the field in Eq. (2.1) is real valued and can be rewritten as

$$\mathbf{E}(\mathbf{r}, t) = \mathbf{E}^{(+)}(\mathbf{r}, t) + \mathbf{E}^{(-)}(\mathbf{r}, t), \tag{2.4}$$

where the positive frequency field $\mathbf{E}^{(+)}(\mathbf{r}, t)$ contains all contributions oscillating as $e^{-i\omega_k t}$ with $\omega_k > 0$, and the negative frequency field $\mathbf{E}^{(-)}(\mathbf{r}, t)$ contains those varying as

$e^{i\omega_k t}$. The positive and negative frequency fields are intrinsically complex and cannot be measured directly. However, as Glauber points out, they are more than a mathematical trick. They carry meaning due to their association with photon absorption and emission and play a central role in his description of the ideal photodetector working on absorption. As we will see later, Glauber's ideal detector is found to be a square-law detector, measuring the average of $\hat{\mathbf{E}}^{(-)}(\mathbf{r},t)\hat{\mathbf{E}}^{(+)}(\mathbf{r},t)$, and not the square of the real field, $\mathbf{E}^2(\mathbf{r},t)$ [Gla63a].

2.2. Quadratures and Phase Space Representation

To obtain a linear, measurable field quantity we will now introduce quadrature operators. From their non-vanishing commutator relation we will find a minimum-uncertainty condition and introduce the phase-space as a handy visualisation of different states. To declutter our notation we will now focus on a single mode k and drop the mode index.

The real-valued and hence measurable quadrature operators are found as a linear combination of the annihilation and creation operator, similar to the real and imaginary part of the complex amplitude

$$\hat{X}_1 = \hat{a} + \hat{a}^\dagger \tag{2.5}$$

$$\hat{X}_2 = \frac{1}{i}\left(\hat{a} - \hat{a}^\dagger\right), \tag{2.6}$$

where, by convention, $\hat{X}_1$ is called amplitude quadrature and $\hat{X}_2$ is called phase quadrature. More generally, a rotated quadrature is defined as

$$\hat{\chi}(\varphi) = \hat{a}e^{-i\varphi} + \hat{a}^\dagger e^{i\varphi}, \tag{2.7}$$

from which the amplitude or phase quadrature are retrieved for $\varphi = 0$ or $\varphi = \pi/2$, respectively [GK05; VW06; BR19; WM08].

The commutator of amplitude and phase quadrature (or more generally of two rotated quadratures out of phase by $\pi/2$) is

$$\left[\hat{X}_1, \hat{X}_2\right] = 2i. \tag{2.8}$$

According to Heisenberg's uncertainty principle then, they cannot be defined sharply at the same time [Hei27; Ken27]. From the generalised uncertainty relation [Rob29]

$$\mathrm{Var}\hat{A} \cdot \mathrm{Var}\hat{B} \geq \frac{1}{4}\left|\left\langle \left[\hat{A}, \hat{B}\right] \right\rangle\right|^2 \tag{2.9}$$

the product of their variances follows as

$$\mathrm{Var}\hat{X}_1 \cdot \mathrm{Var}\hat{X}_2 \geq 1, \tag{2.10}$$

where in the case of the equal sign a minimum-uncertainty state is found.

So far the field in Eq. (2.1) was fully described by the complex amplitudes (in the classical case) or the annihilation and creation operator (in the quantum case). We shall now rewrite the field as

$$\hat{\mathbf{E}}(\mathbf{r}, t) = \left(\frac{\hbar\omega}{2\epsilon_0}\right)^{1/2} \mathbf{e}_u |u(\mathbf{r})| \left[\hat{a} e^{-i\phi(\mathbf{r},t)} + \hat{a}^\dagger e^{i\phi(\mathbf{r},t)}\right] \tag{2.11}$$

$$= \left(\frac{\hbar\omega}{2\epsilon_0}\right)^{1/2} \mathbf{e}_u |u(\mathbf{r})| \left[\hat{X}_1 \cos\phi(\mathbf{r}, t) + \hat{X}_2 \sin\phi(\mathbf{r}, t)\right], \tag{2.12}$$

where we have used a decomposition of the mode function $\mathbf{u}(\mathbf{r}) = \mathbf{e}_u u(\mathbf{r}) = \mathbf{e}_u |u(\mathbf{r})| e^{i\varphi_u(\mathbf{r})}$ into a unit polarisation vector $\mathbf{e}_u$, a scalar amplitude $|u(\mathbf{r})|$, and its space dependent phase $\varphi_u(\mathbf{r})$. Further we have rewritten the phase arguments as $\phi(\mathbf{r}, t) = \omega t - \varphi_u(\mathbf{r}) - \pi/2$.

The field is now interpreted as consisting of a cosine wave, scaled by $\hat{X}_1$, and a sine wave, scaled by $\hat{X}_2$. Knowing the values of the two quadratures fully describes the field and is equivalent to giving a single trigonometric function, e.g. $A\cos(\phi(\mathbf{r}, t) - \theta)$, and knowing its amplitude A and phase-offset θ.

Let us now introduce the phase-space representation of a state of the electric field. As a simple visualisation, the values for the quadratures $\hat{X}_1$ and $\hat{X}_2$ can be drawn into a 2D graph (phasor diagram) with the quadratures as axes, as shown in Fig. 2.1a. A classical, noise free field is completely described by a single point here. Amplitude and relative phase can be read out as $A = \sqrt{X_1^2 + X_2^2}$ and $\theta = \arctan X_2/X_1$. Interference with another field can be solved via vector addition of the phasors.

A quantum field cannot be described by a single point, as amplitude and phase quadrature cannot be measured accurately simultaneously. In the phasor diagram, the quantum

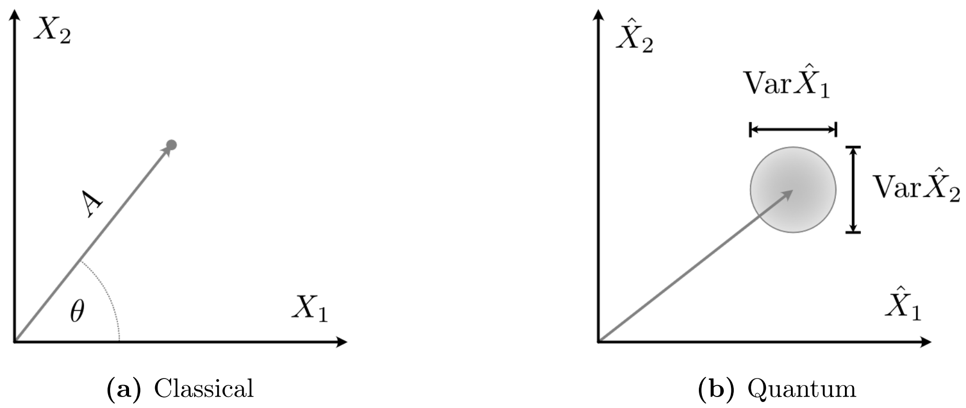

Figure 2.1.: **(a)** Phase space representation of a sharply defined classical field. The point in the phasor diagram is defined by amplitude quadrature X_1 and phase quadrature X_2. Amplitude and phase, as are important for interference, can be read out immediately. **(b)** In the quantum domain the state is characterised by the mean values of $\hat{X}_1$ and $\hat{X}_2$ and their statistical moments, here shown by an area of uncertainty.

field is represented by the mean values of $\hat{X}_1$ and $\hat{X}_2$, with a shaded area scaled as the variances to show the uncertainty, as shown in Fig. 2.1b.

It should be noted that the phasor diagram is only a simplified visualisation of the state. More detailed visual representations are found in the Glauber-Sudarshan P-function, the Wigner function, or the Husimi Q-function, which are outside of the scope of this work (see e.g. [WM08; VW06; GK05; BR19] for further information).

In the description via the quadratures, the amplitude quadrature is often arbitrarily preferred. A single field will be chosen to have a real amplitude α, so that all amplitude is gathered in the amplitude quadrature $\hat{X}_1$ with $\left\langle \hat{X}_2 \right\rangle = 0$. The field is now a cosine wave. For a large enough amplitude, variations in the amplitude quadrature then correspond to a changing cosine amplitude, and fluctuations in the phase quadrature translate to variations in the cosine phase [BR19].

2.3. Quantum States of Light

So far we have treated the quadratures $\hat{X}_1$ and $\hat{X}_2$ or the annihilation operator $\hat{a}$ and the creation operator $\hat{a}^\dagger$ as carrying the information of the field. This view, as described by the Heisenberg picture, is close to the classical description of a field by an observable, e.g. its electric field strength. To calculate quantum mechanical expectation values, however, the operators will have to act on a ket vector $|\psi\rangle$. It is equivalent, and perhaps more usual, to see the state vector as the instance containing all information of the field, as described by the Schrödinger picture. By means of their state vectors, we will now introduce three different quantum states of light relevant to this thesis. The descriptions follow [WM08; GK05; VW06; BR19].

2.3.1. Fock States and the Vacuum State

The first set of states we want to discuss are Fock states. They are characterised by carrying a sharply defined number of photons, and hence are also called number states. Number states are eigenstates of the number operator $\hat{n} = \hat{a}^\dagger \hat{a}$,

$$\hat{n} |n\rangle = n |n\rangle , \tag{2.13}$$

with the integer valued number of photons in the mode, $n = 0, 1, 2, 3, \ldots$, as eigenvalue. As the Hamiltonian of the field contains the number operator, these states are also eigenstates of the Hamiltonian in Eq. (2.3).

The actions of the annihilation and creation operators on the number states are given by

$$\hat{a} |n\rangle = \sqrt{n} |n-1\rangle \tag{2.14}$$

$$\hat{a}^\dagger |n\rangle = \sqrt{n+1} |n+1\rangle . \tag{2.15}$$

The Fock states therefore perfectly illustrate the discrete energy levels of the quantised field and give an intuitive understanding of the annihilation and creation operators as ladder operators.

The number states are orthogonal

$$\langle n|m\rangle = \delta_{nm} \tag{2.16}$$

and form a complete set

$$\sum_{n=0}^{\infty} |n\rangle\langle n| = 1. \tag{2.17}$$

The lowest energy state is the vacuum state $|0\rangle$, from which no further photons can be removed, i.e. $\hat{a} |0\rangle = 0$. While it contains no photons and the expectation value of the electric field is zero, it does show field fluctuations independent of angle φ, as seen from the variance of the general quadrature

$$\mathrm{Var}\hat{\chi}(\varphi)_{|0\rangle} = 1. \tag{2.18}$$

The uncertainty relation of the amplitude and phase quadrature is found as

$$\mathrm{Var}\hat{X}_{1,|0\rangle} \cdot \mathrm{Var}\hat{X}_{2,|0\rangle} = 1, \tag{2.19}$$

showing the vacuum state to be a minimum uncertainty state.

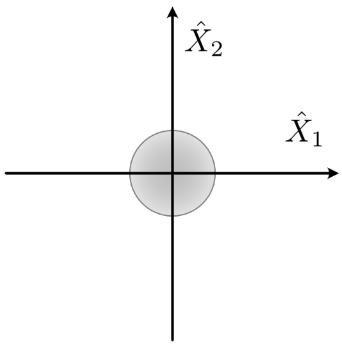

Figure 2.2.: Phase space representation of the vacuum state. The expectation values of both quadratures are zero with equal variances of 1.

Fig. 2.2 shows the phase space representation of the vacuum state. The expectation values of both quadratures are zero, with the probability to find higher values falling off as a Gaussian (see Wigner function of the coherent state with $\alpha = 0$ in [WM08]).

In this work the Fock states are only included for intuition and as an expansion basis. Of all possible number states, only the vacuum state will be important in this thesis.

2.3.2. Coherent States

We will now introduce coherent states. Since they resemble the field generated by a laser most closely, they carry immense practical importance. We will first introduce them as eigenstate of the annihilation operator, and then give an alternative interpretation as states generated by the displacement operator. We will discuss the role of coherent states as the *most classical* quantum state of light and finally introduce its phase space representation.

The coherent state $|\alpha\rangle$ can be found as the right-hand eigenstate of the annihilation operator with the (complex) coherent amplitude α as eigenvalue,

$$\hat{a}\,|\alpha\rangle = \alpha\,|\alpha\rangle\,. \tag{2.20}$$

Naturally then, its adjoint $\langle\alpha|$ is a left-hand eigenstate of the creation operator,

$$\langle\alpha|\,\hat{a}^\dagger = \langle\alpha|\,\alpha^*. \tag{2.21}$$

The mean photon number is found as

$$\langle\alpha|\hat{n}|\alpha\rangle = \langle\alpha|\hat{a}^\dagger\hat{a}|\alpha\rangle = |\alpha|^2. \tag{2.22}$$

The coherent state can be expanded in the Fock basis as

$$|\alpha\rangle = e^{-|\alpha|^2/2}\sum_{n=0}^{\infty}\frac{\alpha^n}{(n!)^{1/2}}\,|n\rangle\,, \tag{2.23}$$

which shows the coherent state to be an infinite superposition of Fock states and emphasises the indefinite photon number of a coherent state.

Unlike Fock states, which even for arbitrarily high excitation show zero mean field strength, coherent states have a non-vanishing expectation value of field strength. Calculating the expectation value of the electric field operator given in Eq. (2.1) (for a single mode) for the coherent state yields

$$\langle\alpha|\hat{\mathbf{E}}(\mathbf{r},t)|\alpha\rangle = \left(\frac{\hbar\omega}{2\epsilon_0}\right)^{1/2}\left[\alpha\mathbf{u}(\mathbf{r})e^{-i\omega t} - \alpha^*\mathbf{u}^*(\mathbf{r})e^{i\omega t}\right], \tag{2.24}$$

i.e. an oscillating electric field as expected of a coherent, classical field with complex amplitude α.

A difference to a classical field is, that the coherent field carries vacuum fluctuations. The variance of the rotated quadrature is

$$\mathrm{Var}\hat{\chi}(\varphi)_{|\alpha\rangle} = 1, \tag{2.25}$$

independent of phase angle and, moreover, independent of the coherent amplitude α. All coherent states are therefore minimum uncertainty states with

$$\mathrm{Var}\hat{X}_{1,|\alpha\rangle} \cdot \mathrm{Var}\hat{X}_{2,|\alpha\rangle} = 1. \tag{2.26}$$

Alternatively to the definition as eigenstate of the annihilation operator, coherent states can be found via the displacement operator

$$\hat{D}(\alpha) = \exp\left(\alpha\hat{a} - \alpha^*\hat{a}\right) \tag{2.27}$$

as a unitary transformation of the vacuum state

$$\hat{D}(\alpha)\left|0\right\rangle = \left|\alpha\right\rangle. \tag{2.28}$$

The coherent state is thereby a displaced vacuum state and, vice-versa, the vacuum state $|0\rangle$ can be seen as a coherent state of amplitude $\alpha = 0$ [VW06]. The displacement operator is unitary with

$$\hat{D}^\dagger(\alpha) = \hat{D}^{-1}(\alpha) = \hat{D}(-\alpha) \tag{2.29}$$

and transforms the annihilation and creation operators according to the Heisenberg picture as

$$\hat{D}^\dagger(\alpha)\hat{a}\hat{D}(\alpha) = \hat{a} + \alpha \tag{2.30}$$

$$\hat{D}^\dagger(\alpha)\hat{a}^\dagger\hat{D}(\alpha) = \hat{a}^\dagger + \alpha^*. \tag{2.31}$$

We will now discuss two aspects that grant the interpretation of coherent states as *most classical* states. First off, and as already seen, the expectation value of the field operator for coherent states reveals oscillations like a classical field. While the coherent state carries vacuum fluctuations unlike the classical field, the fluctuations are the smallest possible quantum noise that could be added, leaving the coherent state closest to the classical field. This oscillating behaviour was emphasised by Erwin Schrödinger, who searched for a stable wavepacket in quantum mechanics that would resemble the classical harmonic oscillator, and found the superposition of number states in Eq. (2.23) as a solution [Sch26].

It was only Glauber who coined the term *coherent state* in 1963. The correlation functions relevant to his theory of coherence are normally ordered products of creation and annihilation operators, e.g. $\hat{a}^\dagger\hat{a}^\dagger\hat{a}\hat{a}$. If a field was to be found in an eigenstate of the operators, the correlation functions would factorise into products of independent functions (here: the eigenvalues α and α^*, i.e. $\alpha^*\alpha^*\alpha\alpha$), and thereby fulfil his conditions for coherence to infinite order. The coherent states as eigenstates of the annihilation operator therefore are states of *full coherence*, and hence came their name. As the factorisation of coherence functions is characteristic of all pre-determined classical fields (e.g. a plane wave), this is taken as further indication of the closeness to classical states [Gla63a].

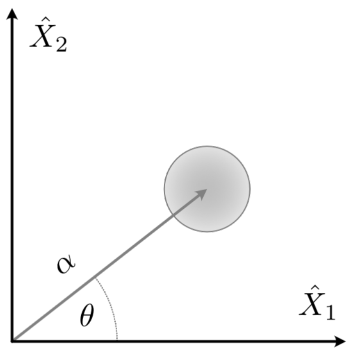

Figure 2.3.: Phase space representation of the coherent state. The expectation values of the quadratures are given as $\langle\hat{X}_1\rangle = 2\,\mathrm{Re}\{\alpha\}$ and $\langle\hat{X}_2\rangle = 2\,\mathrm{Im}\{\alpha\}$. The variances are both 1, independent of coherent excitation.

As we have seen before, coherent states can be interpreted as vacuum states that have been displaced by the coherent amplitude. This is illustrated in Fig. 2.3 where we have moved the circle representing the vacuum state by the coherent excitation α. As noted before, the variances of both quadratures are 1 and moreover independent of the coherent excitation. Therefore the relative noise reduces with growing coherent amplitude – to the point that for large enough α the coherent states appear almost sharply defined, as a classical state would. Further we see that for large enough α a phase θ can be defined which gets sharper with growing amplitude [GK05; VW06].

The fields generated by lasers closely resemble an oscillating classical field with a defined amplitude and phase and can be approximated as coherent states. In this thesis the local oscillator fields, which act as phase references and boost signal to noise ratios, will be described as coherent states.

2.3.3. Squeezed States

The minimum uncertainty states we have introduced so far, the vacuum and the coherent state, show equal variances in all quadratures. Considering the uncertainty relation in Eq. (2.10), however, this is not a necessity. We will now introduce the squeezed state, which shows less fluctuations than the vacuum state in one quadrature. To fulfil the uncertainty relation this decrease in uncertainty for one quadrature will come at the expense of increasing variance in the other quadrature.

Similar to the generation of the coherent state via the displacement operator, the squeezed state too can be generated from the vacuum state via a unitary transformation. Using the squeeze operator

$$\hat{S}(\xi) = \exp\left[\frac{1}{2}\left(\xi^* \hat{a}^2 - \xi \hat{a}^{\dagger 2}\right)\right] \tag{2.32}$$

with the complex squeezing parameter $\xi = re^{i\vartheta}$ containing both squeezing strength ($r = |\xi|$) and angle ($\vartheta = \arg \xi$), a squeezed vacuum state can be found as

$$|\xi, 0\rangle = \hat{S}(\xi) |0\rangle . \tag{2.33}$$

A bright squeezed state, or squeezed coherent state, is generated by additionally applying the displacement operator

$$|\xi, \beta\rangle = \hat{D}(\beta)\hat{S}(\xi) |0\rangle . \tag{2.34}$$

Alternatively, it is possible to first create a coherent state by applying the displacement operator to the vacuum state, and then use the squeezing operator, $\hat{S}(\xi)\hat{D}(\beta') |0\rangle$. To find the same state as before an adjusted coherent displacement β' has to be used. A detailed discussion is found in [VW06; WM08].

The squeeze operator is unitary with

$$\hat{S}^\dagger(\xi) = \hat{S}^{-1}(\xi) = \hat{S}(-\xi) \tag{2.35}$$

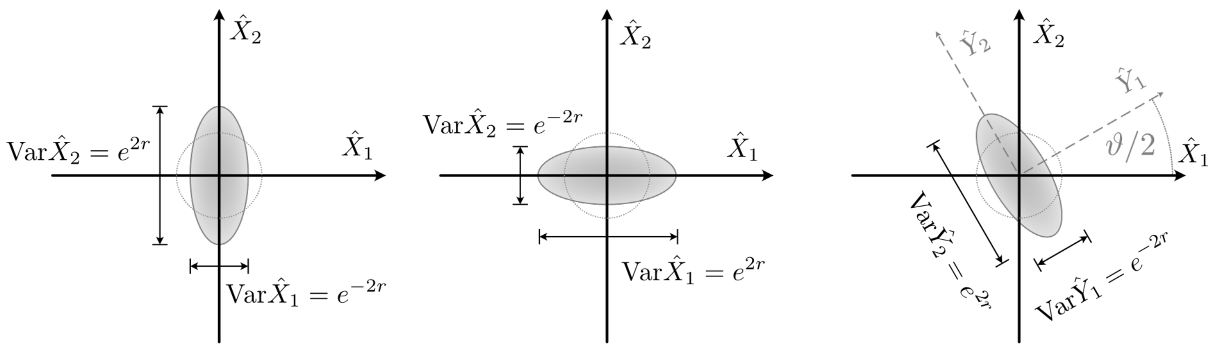

(a) Vacuum with squeezing in $\hat{X}_1$ quadrature

(b) Vacuum with squeezing in $\hat{X}_2$ quadrature

(c) Vacuum with squeezing at arbitrary angle

Figure 2.4.: Vacuum squeezing for different squeezing angles. If the squeezing ellipse is not aligned along the amplitude and phase quadrature axes as shown in **(c)**, it is useful to introduce rotated quadratures $\hat{Y}_1$ and $\hat{Y}_2$ that show minimal and maximal variance.

and transforms the annihilation and creation operator as

$$\hat{S}^\dagger(\xi)\hat{a}\hat{S}(\xi) = \hat{a}\cosh r - \hat{a}^\dagger e^{i\vartheta}\sinh r \tag{2.36}$$

$$\hat{S}^\dagger(\xi)\hat{a}^\dagger\hat{S}(\xi) = \hat{a}^\dagger\cosh r - \hat{a}e^{-i\vartheta}\sinh r. \tag{2.37}$$

Using these transformations, the photon number of a (bright) squeezed state is found as

$$\langle\xi,\beta|\hat{n}|\xi,\beta\rangle = |\beta|^2 + \sinh^2 r \tag{2.38}$$

showing a small increase in photon number through the squeezing. For vanishing coherent amplitude $\beta = 0$, i.e. squeezed vacuum, a small amount of photons $\langle\hat{n}\rangle = \sinh^2 r$ is still found.

We will now discuss squeezing for different squeezing angles ϑ and show the corresponding phase space distributions. For $\vartheta = 0$, noise is reduced in the amplitude quadrature $\hat{X}_1$ and increased in the phase quadrature $\hat{X}_2$, as seen in Fig. 2.4a. The original uncertainty circle of the vacuum state has been squeezed into an upright ellipsis. For $\vartheta = \pi$ the opposite case is realised, see Fig. 2.4b, where the variance in $\hat{X}_2$ is reduced at the cost of more variance in $\hat{X}_1$, yielding a flat ellipse. Fig. 2.4c shows the case of an arbitrary squeezing angle ϑ. Here we can introduce the quadratures $\hat{Y}_1$ and $\hat{Y}_2$, rotated by $\vartheta/2$, which align with the axes of the squeezing ellipsis. Now $\hat{Y}_1$ shows the minimal variance and $\hat{Y}_2$ shows the maximum variance.

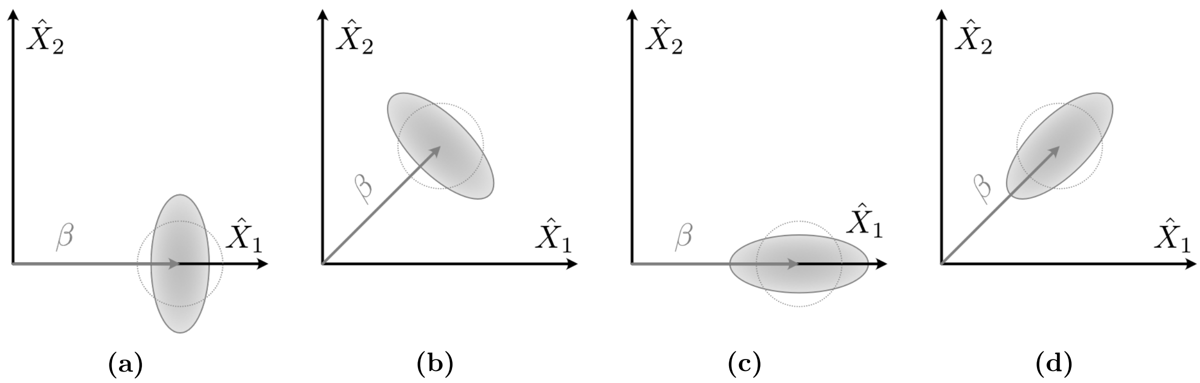

Figure 2.5.: Different scenarios of bright squeezed states with a circle added to show vacuum noise reference. **(a)** amplitude squeezing with coherent amplitude parallel to $\hat{X}_1$, **(b)** amplitude squeezing with arbitrary coherent amplitude, **(c)** phase squeezing with coherent amplitude parallel to $\hat{X}_1$, **(d)** phase squeezing with arbitrary coherent amplitude. Not shown here are states with a squeezing ellipse not aligned with the coherent amplitude.

In all cases, the variances of the quadratures aligning with the squeezing ellipse are given as

$$\mathrm{Var}\hat{Y}_1 = e^{-2r} \tag{2.39}$$

$$\mathrm{Var}\hat{Y}_2 = e^{2r}. \tag{2.40}$$

We shall now look at squeezed coherent states as shown in Fig. 2.5. In 2.5a the short axis of the squeezing ellipsis is aligned with the coherent amplitude β. The magnitude (radius) therefore shows less uncertainty than the phase (angle). We call this an amplitude squeezed state. The same scenario is found in 2.5b, even though the coherent amplitude is no longer aligned with the $\hat{X}_1$ axis. This state could be found via time evolution from the first state and is still an amplitude squeezed state.

In 2.5c the long axis of the squeezing ellipse is aligned with the coherent excitation. Consequently the uncertainty in magnitude will be higher than the uncertainty in phase. We call this a phase squeezed state. The same is found in 2.5d, where the coherent amplitude is no longer parallel to $\hat{X}_1$.

We want to emphasise that amplitude or phase squeezing in this definition in general does not mean reduced variance specifically in the amplitude or phase quadrature. Instead, we may again introduce rotated quadratures $\hat{Y}_1$ and $\hat{Y}_2$, aligned with the squeezing ellipse, that show either minimal or maximal variance as described above.

Squeezed states have found many applications in research and technology. Naturally they can be used to improve measurements limited by vacuum fluctuations, e.g. in microscopy in biology [Cas+21]. Similarly they allow improvements in interferometry [Cav81], with the GEO 600 being the first gravitational wave observatory to employ squeezed light to increase sensitivity and thereby increase the size of the observable universe [Gro+13]. Squeezed light sources also found their way into the LIGO observatory [Aas+13], which would later be the first to successfully detect a gravitational wave [Abb+16].

Further, squeezed states are used in quantum key distribution, enabling secure communication [CLA01; Mad+12]. Another important application is in continuous variable quantum computation [vLWG07; Yok+13; Mar+16].

Squeezed states of light are relevant to this thesis as a test state with known correlation properties to test the implementation of balanced homodyne correlation. We will generate them via optical parametric amplification as discussed in section 3.1.

2.4. Correlation Functions

We have introduced different quantum states and discussed their fluctuation properties. As a new property, we will now turn to correlation. We will start our discussion with selected elements of Glauber's quantum theory of optical coherence from 1963 [Gla63a]. This will help us to get familiar with correlation functions and understand their inherent normal ordering, and it will become easier to comprehend the theory of balanced homodyne correlation later. We will limit our treatment to pure states. A straightforward extension to mixed states via the density operator and the trace is available in the original source.

2.4.1. Ideal Photon Counter and First Order Correlation

Following Glauber, we begin with the discussion of an ideal photon counter, which will lead to the first order correlation function. We consider the measurement of photon flux via *absorption*, as is typical for photoelectric detection. In the absorption of a photon the field undergoes a transition from its initial state $|i\rangle$ to a final state $|f\rangle$. The matrix element of this transition is given as

$$\langle f|\hat{E}^{+}(\mathbf{r},t)|i\rangle \tag{2.41}$$

where we have used the positive frequency electric field which is associated with photon absorption. Since $\hat{E}^{(+)}(\mathbf{r},t)$ and the annihilation operator are proportional, this is equivalent to a (perhaps more modern) description using the annihilation operator. The transition probability consequently becomes

$$T_{if} = \left| \langle f|\hat{E}^{(+)}(\mathbf{r},t)|i\rangle \right|^2 . \tag{2.42}$$

For an ideal detector the total counting rate is proportional to the sum over all final states [Gla63a; WM08]

$$\sum_f T_{fi} = \sum_f \langle i|\hat{E}^{(-)}(\mathbf{r},t)|f\rangle \; \langle f|\hat{E}^{(+)}(\mathbf{r},t)|i\rangle \; = \; \langle i|\hat{E}^{(-)}(\mathbf{r},t)\hat{E}^{(+)}(\mathbf{r},t)|i\rangle \tag{2.43}$$

where we have used the completeness relation $\sum_f |f\rangle\langle f| = 1$. To simplify our notation we will now abbreviate the space-time point $(\mathbf{r},t) = (\mathbf{r}t)$. The expectation value in Eq. (2.43) is the first order correlation function for equal space-time points,

$$\mathcal{G}^{(1)}(\mathbf{r}t,\mathbf{r}t) = \left\langle \hat{E}^{(-)}(\mathbf{r}t)\hat{E}^{(+)}(\mathbf{r}t) \right\rangle . \tag{2.44}$$

By generalising the space-time arguments to different space-time points we find the general first order correlation function

$$\mathcal{G}^{(1)}(\mathbf{r}t,\mathbf{r}'t') = \left\langle \hat{E}^{(-)}(\mathbf{r}t)\hat{E}^{(+)}(\mathbf{r}'t') \right\rangle \tag{2.45}$$

which describes the correlation of light coming from two different space-time points, as found e.g. in Young's double-slit experiment (see e.g. [WM08]). Classical coherence properties can be explained sufficiently with the first order coherence function $\mathcal{G}^{(1)}$ [Gla63a].

2.4.2. Coincidence Rate, Second Order Correlation and n-fold Coincidence

So far we have considered a single detector. The previous considerations can be extended to two detectors, allowing the coincidence measurement of detecting one photon at $(\mathbf{r}t)$ and one at $(\mathbf{r}'t')$. Hanbury Brown and Twiss pioneered this type of measurement in 1956 when they showed positive correlations between the two arms of a split-beam from a mercury arc lamp [HT56a]. The matrix element of this two-fold absorption is given by

$$\langle f|\hat{E}^{(+)}(\mathbf{r}'t')\hat{E}^{(+)}(\mathbf{r}t)|i\rangle \tag{2.46}$$

and the total rate of the transition will be proportional to the sum over all final states

$$\sum_f \left| \langle f|\hat{E}^{(+)}(\mathbf{r}'t')\hat{E}^{(+)}(\mathbf{r}t)|i\rangle \right|^2 = \langle i|\hat{E}^{(-)}(\mathbf{r}t)\hat{E}^{(-)}(\mathbf{r}'t')\hat{E}^{(+)}(\mathbf{r}'t')\hat{E}^{(+)}(\mathbf{r}t)|i\rangle \,. \tag{2.47}$$

We have found the two space-time point correlation function, describing intensity correlations between the fields at the points $(\mathbf{r}t)$ and $(\mathbf{r}'t')$ as measured by Hanbury Brown and Twiss,

$$\mathcal{G}^{(2)}(\mathbf{r}t, \mathbf{r}'t') = \left\langle \hat{E}^{(-)}(\mathbf{r}t)\hat{E}^{(-)}(\mathbf{r}'t')\hat{E}^{(+)}(\mathbf{r}'t')\hat{E}^{(+)}(\mathbf{r}t) \right\rangle . \tag{2.48}$$

As before, we can generalise the space-time arguments to find the general second order correlation function

$$\mathcal{G}^{(2)}(\mathbf{r}_1t_1, \mathbf{r}_2t_2, \mathbf{r}_3t_3, \mathbf{r}_4t_4) = \left\langle \hat{E}^{(-)}(\mathbf{r}_1t_1)\hat{E}^{(-)}(\mathbf{r}_2t_2)\hat{E}^{(+)}(\mathbf{r}_3t_3)\hat{E}^{(+)}(\mathbf{r}_4t_4) \right\rangle , \tag{2.49}$$

which describes field correlations between four space-time points.

We can now add even more detectors to the scheme and measure their n-fold coincidence rate. Following the argument above, the matrix element will be

$$\langle f|\hat{E}^{(+)}(\mathbf{r}_nt_n)\ldots\hat{E}^{(+)}(\mathbf{r}_1t_1)|i\rangle \,, \tag{2.50}$$

and the n-th order correlation function of n-fold intensity correlation will be

$$\mathcal{G}^{(n)}(\mathbf{r}_1t_1, \ldots, \mathbf{r}_nt_n) = \left\langle \hat{E}^{(-)}(\mathbf{r}_1t_1)\ldots\hat{E}^{(-)}(\mathbf{r}_nt_n)\hat{E}^{(+)}(\mathbf{r}_nt_n)\ldots\hat{E}^{(+)}(\mathbf{r}_1t_1) \right\rangle . \tag{2.51}$$

Generalising the space-time arguments we can define the general n-th order correlation function

$$\begin{aligned}\mathcal{G}^{(n)}(&\mathbf{r}_1t_1, \ldots, \mathbf{r}_nt_n, \mathbf{r}_{n+1}t_{n+1}, \ldots, \mathbf{r}_{2n}t_{2n}) = \\ &\left\langle \hat{E}^{(-)}(\mathbf{r}_1t_1)\ldots\hat{E}^{(-)}(\mathbf{r}_nt_n)\hat{E}^{(+)}(\mathbf{r}_{n+1}t_{n+1})\ldots\hat{E}^{(+)}(\mathbf{r}_{2n}t_{2n}) \right\rangle ,\end{aligned} \tag{2.52}$$

describing field correlations between $2n$ space-time points.

In this thesis we will directly measure intensity correlations between four detectors, i.e. $\mathcal{G}^{(4)}(\mathbf{r}_1 t_1, \mathbf{r}_2 t_2, \mathbf{r}_3 t_3, \mathbf{r}_4 t_4)$, and use them to calculate more general correlation functions with uneven powers of positive and negative frequency electric field operators, see Sec. 2.6.

2.4.3. Inherent Normal Ordering

We will now take a closer look at the structure of the correlations functions. The matrix elements in Eqs. (2.41), (2.46) and (2.50), as starting points, only contain the positive frequency electric field operators, or equivalently, the annihilation operators. By the calculation of the transition probability as absolute square and removal of the inner dyad $|f\rangle\langle f|$, the result will always have all positive frequency field operators to the right, and all negative frequency operators to the left. This is equivalent to finding all annihilation operators to the right and all creation operators to the left. Thereby the correlation functions found from absorption of photons are *inherently normally ordered*.

An important consequence from the normal ordering is that the vacuum state shows zero correlation for all orders of correlation function. Thereby unwantedly mixed-in vacuum terms, which cannot be completely prevented in experiment, play no role. In this regard correlation measurements have a considerable advantage in comparison to other methods such as balanced homodyne detection.

2.5. Balanced Homodyne Detection

Before we turn to the goal of this theory chapter, understanding balanced homodyne *correlation*, we need to first address one of its founding measurement techniques – balanced homodyne *detection* (BHD). BHD was developed at the end of the 1970s and the early 1980s to measure the squeezed state's phase-dependent, reduced below or increased above vacuum level, fluctuations. It was understood that combining the signal field to be examined with a strong reference field in a coherent state, the local oscillator (LO), could dramatically increase signal to noise ratio, but at the cost of introducing additional fluctuations from the LO [SYM79]. Especially if the LO carried excess noise above the quantum noise limit, accurate determination of the fluctuations of the squeezed field would become impossible. BHD, as proposed by Yuen and Chan in 1983 [YC83] overcomes this problem by using a 50:50 beam splitter to combine the fields, and subtracting the photocurrents of their outputs. As a result, all LO noise is removed from the resulting signal. BHD has become a standard tool in quantum optics and descriptions are widely available in standard text books, see e.g. [GK05; BR19; VW06]. In this chapter we will give a short derivation of the measurement principle of BHD and briefly discuss its strengths and shortcomings.

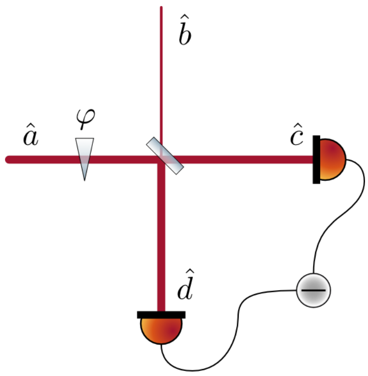

Figure 2.6.: Scheme for balanced homodyne detection.

Fig. 2.6 shows the optical scheme used for BHD. A 50:50 beam splitter is used to combine the signal field, described by the annihilation operator $\hat{b}$, with a strong LO, described by $\hat{a}$. The LO phase φ can be set via a phase shifter. The fields after the beam splitter ($\hat{c}$ and $\hat{d}$) are found from the beam splitter matrix as

$$\hat{c} = \frac{1}{\sqrt{2}}(\hat{a} + \hat{b}) \tag{2.53}$$

$$\hat{d} = \frac{1}{\sqrt{2}}(\hat{a} - \hat{b}). \tag{2.54}$$

The photodetectors in the outputs of the beam splitter measure the photocurrents

$$\hat{n}_c = \hat{c}^\dagger \hat{c} = \frac{1}{2}\left(\hat{a}^\dagger \hat{a} + \hat{a}^\dagger \hat{b} + \hat{b}^\dagger \hat{a} + \hat{b}^\dagger \hat{b}\right) \tag{2.55}$$

$$\hat{n}_d = \hat{d}^\dagger \hat{d} = \frac{1}{2}\left(\hat{a}^\dagger \hat{a} - \hat{a}^\dagger \hat{b} - \hat{b}^\dagger \hat{a} + \hat{b}^\dagger \hat{b}\right). \tag{2.56}$$

The photocurrents are subtracted, with the difference current given as

$$\hat{n}_c - \hat{n}_d = \hat{a}^\dagger \hat{b} + \hat{b}^\dagger \hat{a}. \tag{2.57}$$

We will now linearise the LO's annihilation operator as $\hat{a} \to \alpha + \delta\hat{a}$ where α carries the coherent excitation and $\delta\hat{a}$ contains the remaining fluctuations, and similarly $\hat{b} \to \beta + \delta\hat{b}$.

The difference photocurrent now becomes

$$\hat{n}_c - \hat{n}_d = (\alpha^* + \delta\hat{a}^\dagger)(\beta + \delta\hat{b}) + (\beta^* + \delta\hat{b}^\dagger)(\alpha + \delta\hat{a}) \tag{2.58}$$

$$= \alpha^*\beta + \beta^*\alpha + \alpha^*\delta\hat{b} + \alpha\delta\hat{b}^\dagger + \beta^*\delta\hat{a} + \beta\delta\hat{a}^\dagger + \delta\hat{a}\delta\hat{b}^\dagger + \delta\hat{a}^\dagger\delta\hat{b} \tag{2.59}$$

$$\approx \underbrace{2|\alpha||\beta|\cos(\varphi_b - \varphi_a)}_{\text{I: static interference}} + \underbrace{|\alpha|\delta\hat{\chi}_b(\varphi_a)}_{\text{II: homodyning of signal mode}} + \underbrace{|\beta|\delta\hat{\chi}_a(\varphi_b)}_{\text{III: homodyning of LO}} \tag{2.60}$$

where we have introduced $\varphi_a = \arg\alpha$ and $\varphi_b = \arg\beta$ and have neglected terms quadratic in fluctuations.

The first term describes a static offset caused by the interference of the coherent amplitudes of the states. The second term shows the signal field's fluctuations in a quadrature determined by the phase of the LO, scaled with the LO amplitude $|\alpha|$. The third term concerns fluctuations in the LO's quadrature under the angle of the signal field, scaled with the coherent amplitude of the signal state $|\beta|$.

In an experiment the outputs of the photodiodes will be AC-filtered (high pass filtered). All offsets thereby vanish and only components oscillating or fluctuating at high enough frequencies are measured. Further, the LO magnitude by far surpasses the magnitude of the signal field, $|\alpha| \gg |\beta|$, as is a requirement for BHD. We can therefore approximate the difference photo current as

$$\hat{n}_c - \hat{n}_d \approx |\alpha|\delta\hat{\chi}_b(\varphi_a). \tag{2.61}$$

While the expectation value of $\delta\hat{\chi}_b$ vanishes, we are interested in the variance which is found as

$$\mathrm{Var}\left(\hat{n}_c - \hat{n}_d\right) \approx |\alpha|^2 \,\mathrm{Var}\left(\delta\hat{\chi}_b(\varphi_a)\right). \tag{2.62}$$

We see that BHD allows phase angle resolved measurement of quadrature variance, where the angle can be set arbitrarily by the LO phase. When squeezing is to be measured, the phase angle of minimum or maximum variance can be precisely dialled in. Moreover, the measurement of the signal field's quadrature variance is amplified with the LO's coherent amplitude, allowing for a high signal to noise ratio. The fluctuations carried by the LO only scale with the far weaker amplitude of the signal field, and become insignificant.

If vacuum is unwantedly mixed-in, as is typical in experiments due to non-perfect optical elements, the measured variance will contain a contribution from the vacuum's

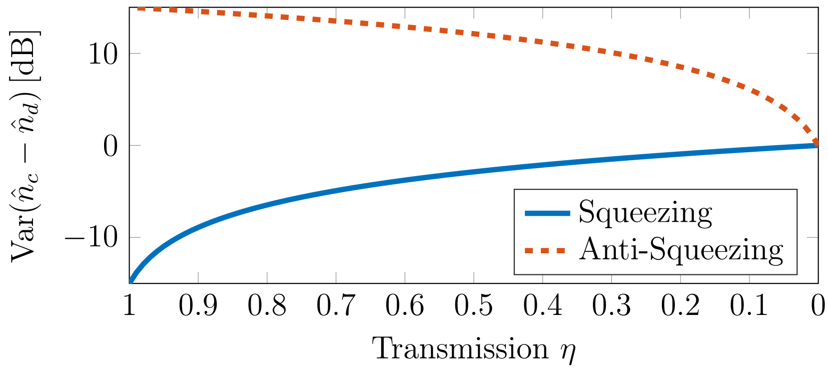

Figure 2.7.: Measurable squeezing and anti-squeezing under varying degrees of losses for originally 15 dB of squeezing and anti-squeezing in the signal. The squeezing (blue solid line) is quickly diminished by even small losses while the anti-squeezing (red dashed line) remains strong until very high losses. All variances are referenced to vacuum fluctuations equal to 0 dB = 1.

fluctuations. We can model this scenario by imagining an additional beam splitter in the signal's input path, with a power transmission of η, where in the case of $\eta = 1$ the ideal, lossless case is realised. The signal beam is transformed via the beam splitter relations as $\hat{b} \rightarrow \sqrt{\eta}\,\hat{b} + \sqrt{1-\eta}\,\hat{v}$, where $\hat{v}$ corresponds to the mixed-in vacuum mode. Repeating the calculations for this case yields the difference current variance

$$\mathrm{Var}(\hat{n}_c - \hat{n}_d) \approx |\alpha|^2 \left[\eta \cdot \mathrm{Var}(\delta\hat{\chi}_b(\varphi_a)) + (1-\eta) \cdot \underbrace{\mathrm{Var}(\delta\hat{\chi}_v(\varphi_a))}_{\equiv 1}\right]. \tag{2.63}$$

The original variance is transmitted with η, while the added-in vacuum fluctuations scale with $1-\eta$. Fig. 2.7 shows the resulting variance for different transmission values η. It becomes apparent that especially the squeezing (the minimum variance of the squeezing ellipse) quickly diminishes in inefficient detection, while the anti-squeezing (the maximum variance of the squeezing ellipse) remains more stable for most efficiencies. If a reconstruction of the phase space distribution of the signal state is performed, inefficient detection translates into the finer features of the state being quickly lost [Vog95].

2.6. Balanced Homodyne Correlation

We now turn to balanced homodyne correlation (BHC). We saw in Sec. 2.4 that coincidence photodetection allows the measurement of correlation functions with *equal powers* of creation and annihilation operators. Due to the inherent normal ordering all vacuum terms vanish. BHD, as discussed in the previous section 2.5, enables the measurement of quadrature variance with high signal to noise ratio due to the use of a strong LO, but suffers from losses.

Homodyne correlation techniques [OHM87; Vog91; Vog95] were proposed to measure squeezing without the influence of detector noise, and to measure squeezing in scenarios where losses cannot be avoided, since losses only act as a scaling factor. Classical LO noise is not cancelled out, however, so homodyne correlation techniques were only considered for weak LOs.

More complex homodyne correlation techniques, allowing the measurement of moments with *equal or unequal powers* of creation and annihilation operators, were proposed for the characterisation of nonclassicality [SV05]. Due to the use of a weak LO, however, only low order moments were accessible.

In BHC, the limitation to weak LOs is overcome by an effective subtraction of photocurrents in the post-processing [SV06]. With a strong LO allowing high signal to noise ratios, *high order moments* with *equal or unequal powers* of creation and annihilation operators can be measured, as are required for the determination of general correlation properties and for certain non-classicality criteria [Vog08]. Losses of the signal beam still only act as a scaling factor. Advantages of BHD and homodyne correlation are thus combined.

2.6.1. Ideal Case

We begin our treatment with the ideal case of perfect splitting ratios and symmetric transmission for all paths, as described in [SV06], complemented with additional explanations to help understanding. Afterwards, we will add our own view as experimentalists and discuss the influence of non-ideal splitting ratios, uneven transmissions and the influence of losses in the signal beam. We use the Heisenberg picture and focus on the propagation of the annihilation operators through the optical system, rather than propagating the state of light.

In Sec. 2.4.2 we discussed the n-th order correlation function with the restriction of equal powers of creation and annihilation operators. We will now allow uneven powers and introduce a more generalised normally ordered correlation function

$$\mathcal{G}^{(n,m)}(x_1, ..., x_n, y_1, ..., y_m) = \left\langle {}^{\circ}_{\circ} \prod_{k=1}^{n} \hat{a}^{\dagger}(x_k) \prod_{l=1}^{m} \hat{a}(y_l) {}^{\circ}_{\circ} \right\rangle, \tag{2.64}$$

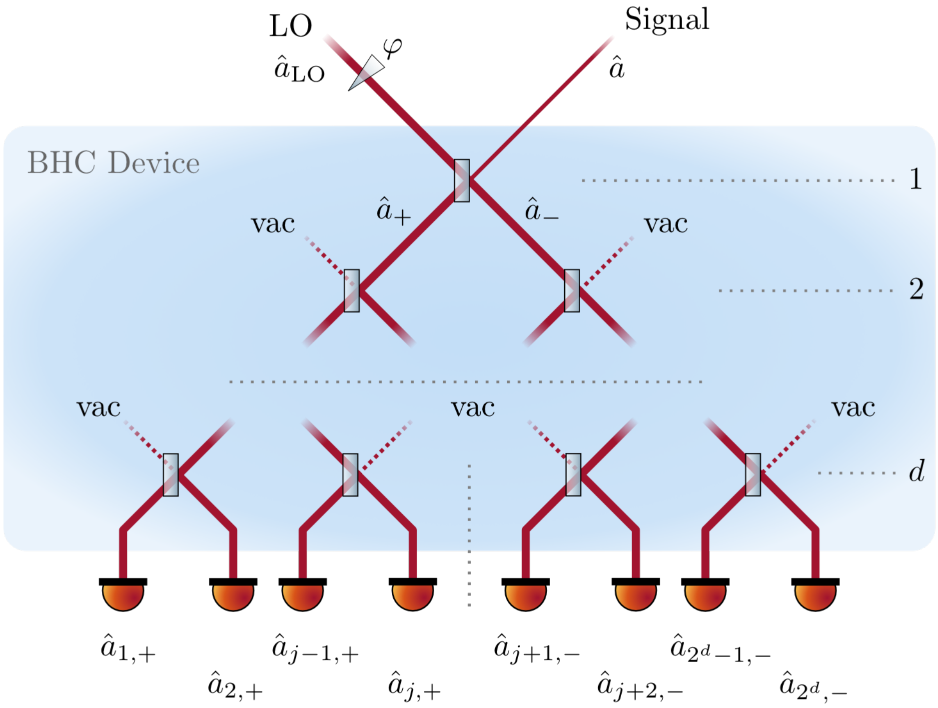

Figure 2.8.: BHC measurement scheme. Signal field and LO are combined at a 50:50 beam splitter, the resulting fields are split at subsequent 50:50 splitters with vacuum as second input. After in total d stages (depth of device), the 2^d outputs are detected by individual photodiodes, allowing determination of moments $\mathcal{G}^{(n,m)}$ with $n+m \leq 2^{d-1}$. Added vacuum terms vanish due to correlative measurement.

where $x_k = (\mathbf{r}_k, t_k)$ and $y_l = (\mathbf{r}_l, t_l)$ denote space-time points and $\circ\!\!\circ\, \hat{O} \,\circ\!\!\circ$ denotes time- and normal ordering, i.e. all creation operators are to the left of all annihilation operators and time arguments increase from left to right for creation operators and vice versa for annihilation operators (operators associated with earlier times have to act on the state before those associated with later times).

In this work we consider the simpler case of equal space-time points $x_1 = ... = x_n = y_1 = ... = y_m = (\mathbf{r}, t)$ (an extension to general space-time point correlations is given in the original publication), with the correlation function reducing to

$$\mathcal{G}^{(n,m)} = \left\langle \hat{a}^\dagger(\mathbf{r}, t)^n \hat{a}(\mathbf{r}, t)^m \right\rangle . \tag{2.65}$$

Fig. 2.8 shows the BHC measurement scheme. The signal field is combined with the LO at the initial 50:50 beam splitter; the LO phase φ is set with a phase shifter. The outputs are subsequently divided by more 50:50 beam splitters, until after d stages the 2^d outputs are detected by photodiodes.

We shall now describe the propagation of the signal field and the LO through the set-up by means of the evolution of their annihilation operators. The combination of fields by the initial 50:50 beam splitter yields the outputs

$$\hat{a}_{\pm} = \frac{1}{\sqrt{2}} \left(\hat{a} \pm \hat{a}_{\mathrm{LO}} \right), \tag{2.66}$$

where the $(\pm)$ phase of the transmitted or reflected LO differentiates the left $(+)$ and the right $(-)$ output. After the path to the j-th photodetector, the resulting annihilation operators read as

$$\hat{a}_{j,\pm} = \frac{e^{i\Phi_j}}{\sqrt{2^{d-1}}} \hat{a}_{\pm} + \mathrm{vac}, \tag{2.67}$$

where, again, $(\pm)$ differentiates between left-hand and right-hand outputs. The further subdivisions of the field have introduced a reduction in amplitude by $1/\sqrt{2^{d-1}}$ with respect to the original beam splitter outputs, and a path dependent phase Φ_j has been added. While additional vacuum terms (vac) have been mixed-in from the open inputs, their contribution to the measured correlation functions vanishes under the normal ordering.

We now directly measure the correlation between sets of $k = 2^{(d-1)}$ detectors, i.e. half of the available 2^d photodiodes. Their correlation is given by

$$\Gamma_{j_1,\ldots,j_k}(\varphi) = \left\langle : \hat{a}^{\dagger}_{j_1} \hat{a}_{j_1} \cdots \hat{a}^{\dagger}_{j_k} \hat{a}_{j_k} : \right\rangle, \tag{2.68}$$

where the normal ordering is an inherent property of the correlative measurement, as discussed in section 2.4.3. It is noted explicitly, that the k-fold correlation function is phase-dependent, hence in the experiment a time-averaged measurement of $\Gamma_{j_1,\ldots,j_k}(\varphi)$ has to be taken for every (discrete) LO angle φ.

Using Eq. (2.67) we can rewrite the photocurrent of a chosen detector j as

$$\hat{a}^{\dagger}_{j,\pm} \hat{a}_{j,\pm} = \left(\frac{e^{i\Phi_j}}{\sqrt{2^{d-1}}} \hat{a}^{\dagger}_{\pm} \right) \left(\frac{e^{-i\Phi_j}}{\sqrt{2^{d-1}}} \hat{a}_{\pm} \right) = \frac{1}{2^{d-1}} \hat{a}^{\dagger}_{\pm} \hat{a}_{\pm} \tag{2.69}$$

and find it to depend only on it being a left- or right-hand side detector, but not on the individual detector chosen. Therefore the k-fold correlation function only depends on the number l of detectors chosen from the left-hand side. Introducing the number operator after the first beam splitter, $\hat{n}_\pm = \hat{a}_\pm^\dagger \hat{a}_\pm$, we can now rewrite Eq. (2.68) as

$$\Gamma_l^{(k)}(\varphi) = 2^{-k(d-1)} \left\langle : \hat{n}_+^l \hat{n}_-^{k-l} : \right\rangle . \tag{2.70}$$

Recalling the binomial formula

$$(x+y)^k = \sum_{l=0}^{k} \binom{k}{l} x^l y^{k-l} \tag{2.71}$$

we explicitly construct a binomial form from Eq. (2.70) by combining one correlation function $\Gamma_l^{(k)}$ for each $l = 0, ..., k$ in a balanced pattern into the BHC signal

$$F^{(k)}(\varphi) = \sum_{l=0}^{k} (-1)^{k-l} \binom{k}{l} \Gamma_l^{(k)} \tag{2.72}$$

$$= 2^{-k(d-1)} \cdot \sum_{l=0}^{k} (-1)^{k-l} \binom{k}{l} \left\langle : \hat{n}_+^l \hat{n}_-^{k-l} : \right\rangle \tag{2.73}$$

$$= 2^{-k(d-1)} \cdot \left\langle : (\hat{n}_+ - \hat{n}_-)^k : \right\rangle . \tag{2.74}$$

Note should be taken of the alternating sign in Eq. (2.72), which yields a subtraction of the number operators of the left and right output of the initial beam splitter in Eq. (2.74). Similar to BHD, all symmetric terms in the outputs, due only to a single input field, are hereby eliminated.

To evaluate the difference of the left- and right hand number operators we start with linearising the LO's operators by replacing $\hat{a}_{\mathrm{LO}} \to \alpha_{\mathrm{LO}} + \delta\hat{a}_{\mathrm{LO}}$, where α_{LO} carries the coherent amplitude and $\delta\hat{a}_{\mathrm{LO}}$ acts on the fluctuations only. Considering the equivalence of a coherent states fluctuations to the vacuum state, we immediately see that all terms containing $\delta\hat{a}_{\mathrm{LO}}$ or its conjugate vanish under normal ordering, similar to the vacuum terms above[1]. Hence we can rewrite the number operators (taken directly after the first beam splitter) as

$$\hat{n}_\pm = \hat{a}_\pm^\dagger \hat{a}_\pm = \frac{1}{2} \left(\hat{a}^\dagger \pm \alpha_{\mathrm{LO}}^* \right) \left(\hat{a} \pm \alpha_{\mathrm{LO}} \right) \tag{2.75}$$

$$= \frac{1}{2} \left(\hat{a}^\dagger \hat{a} \pm \left(\alpha_{\mathrm{LO}} \hat{a}^\dagger + \alpha_{\mathrm{LO}}^* \hat{a} \right) + |\alpha_{\mathrm{LO}}|^2 \right) \tag{2.76}$$

$$= \frac{1}{2} \left(\hat{a}^\dagger \hat{a} \pm |\alpha_{\mathrm{LO}}| \hat{\chi}_\varphi + |\alpha_{\mathrm{LO}}|^2 \right) . \tag{2.77}$$

[1] $\hat{a}_{\mathrm{LO}} |\alpha_{\mathrm{LO}}\rangle \equiv (\alpha_{\mathrm{LO}} + \delta\hat{a}_{\mathrm{LO}}) |\alpha_{\mathrm{LO}}\rangle = \alpha_{\mathrm{LO}} |\alpha_{\mathrm{LO}}\rangle + \underbrace{\delta\hat{a}_{\mathrm{LO}} |\alpha_{\mathrm{LO}}\rangle}_{=0} = \alpha_{\mathrm{LO}} |\alpha_{\mathrm{LO}}\rangle$

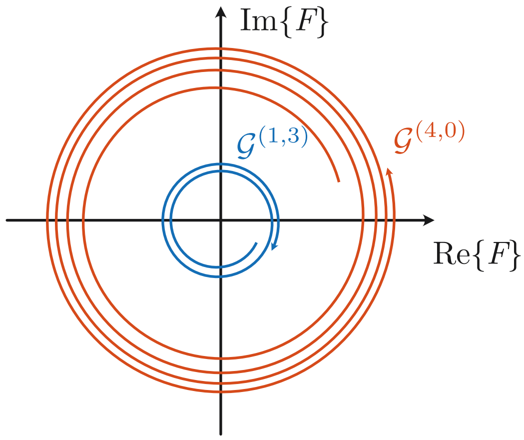

Figure 2.9.: Evolution of different $\mathcal{G}^{(n,m)}$ contributions with varying LO phase from 0 to 2π. $\mathcal{G}^{(1,3)}$ (shown in blue) completes two full clockwise circulations per 2π-evolution of LO phase while $\mathcal{G}^{(4,0)}$ (shown in red) shows 4 counter clockwise rotations. An arbitrary initial phase was added for generality. The change of radius is for illustration only.

In the difference of photo currents, $\hat{n}_+ - \hat{n}_-$, all contributions except the quadrature term cancel out and Eq. (2.74) becomes

$$F^{(k)}(\varphi) = 2^{-k(d-1)} |\alpha_{\mathrm{LO}}|^k \left\langle : \chi_\varphi^k : \right\rangle . \tag{2.78}$$

Under normal ordering and using the binomial formula again, the k-th power of the quadrature operator can be evaluated as

$$\begin{aligned} \left\langle : \chi_\varphi^k : \right\rangle &= \left\langle : \left(\hat{a}^\dagger e^{i\varphi} + \hat{a} e^{-i\varphi} \right)^k : \right\rangle & (2.79) \\ &= \sum_{l=0}^{k} \binom{k}{l} \left\langle \hat{a}^{\dagger l} \hat{a}^{k-l} \right\rangle e^{-i(k-2l)\varphi} & (2.80) \\ &\equiv \sum_{l=0}^{k} \binom{k}{l} \mathcal{G}^{(l,k-l)} e^{-i(k-2l)\varphi}, & (2.81) \end{aligned}$$

where we have identified the sought after correlation function $\mathcal{G}^{(n,m)}$ in the last line. The BHC signal is now given by

$$F^{(k)}(\varphi) = 2^{-k(d-1)} |\alpha_{\mathrm{LO}}|^k \sum_{l=0}^{k} \binom{k}{l} \mathcal{G}^{(l,k-l)} e^{-i(k-2l)\varphi}. \tag{2.82}$$

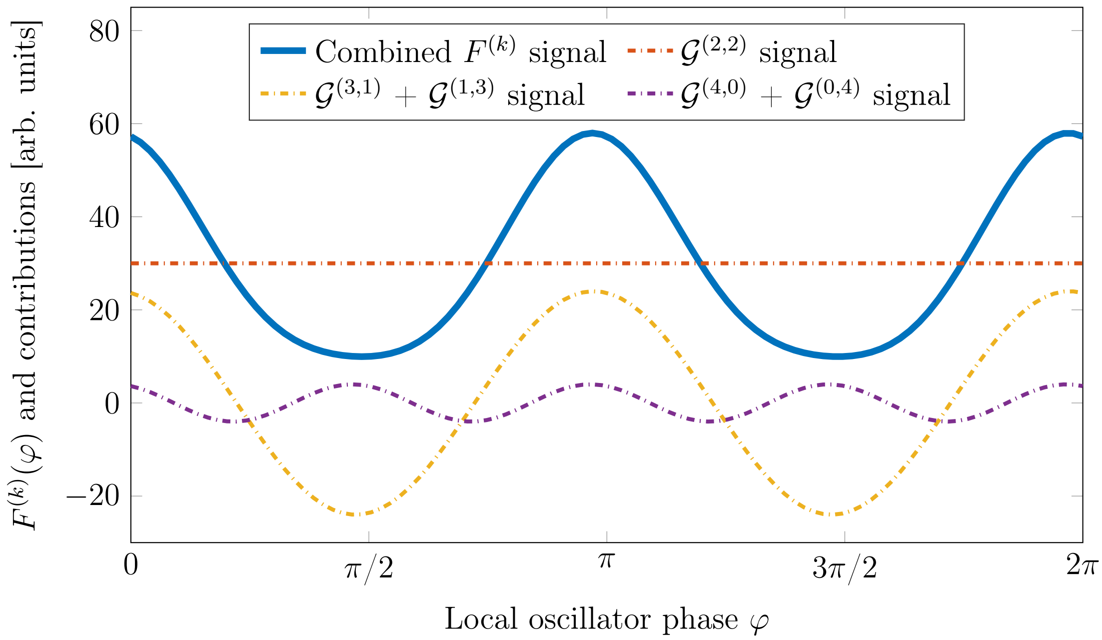

Figure 2.10.: Example of BHC signal evolution $F^{(k)}(\varphi)$ (thick blue line), here for $k = 4$, with changing LO phase. All three contributions to the signal are shown. First, $\mathcal{G}^{(2,2)}$ (dashed-dotted red line) shows no phase dependence. Contributions of odd ordered correlation functions $\mathcal{G}^{(n,m)}$ are grouped together with their adjoint $\mathcal{G}^{(m,n)}$ to create a real valued cosine signal at their mutual frequency. The signal from $\mathcal{G}^{(3,1)}$ and $\mathcal{G}^{(1,3)}$ (dashed-dotted yellow line) shows two oscillations per 2π-rotation of LO phase, while the signal from $\mathcal{G}^{(4,0)}$ and $\mathcal{G}^{(0,4)}$ (dashed-dotted purple line) shows four. An arbitrary phase was added to the $\mathcal{G}^{(n,m)}$ (except $\mathcal{G}^{(2,2)}$, which is real valued) for generality.

While the left-hand side is determined by experiment, the right-hand side gives the interpretation in terms of the correlation moments. All accessible correlation functions $\mathcal{G}^{(n,m)}$, with $m + n \leq k$, are encoded with different oscillation frequencies in the complex plane regarding to changes of the LO phase φ, as shown in Fig. 2.9.

Correlation functions with flipped indices, $\mathcal{G}^{(n,m)}$ and $\mathcal{G}^{(m,n)}$, are complex conjugates, as can be seen from

$$\mathcal{G}^{(m,n)} = \langle \hat{a}^{\dagger m} \hat{a}^n \rangle = \left\langle \left(\hat{a}^{\dagger n} \hat{a}^m \right)^\dagger \right\rangle = \langle \hat{a}^{\dagger n} \hat{a}^m \rangle^\dagger = \left(\mathcal{G}^{(n,m)} \right)^\dagger = \left(\mathcal{G}^{(n,m)} \right)^* . \tag{2.83}$$

The combined contribution of the moments $\mathcal{G}^{(n,m)}$ and $\mathcal{G}^{(m,n)}$ to the BHC signal is then a real valued cosine, e.g.

$$\mathcal{G}^{(3,1)}e^{2i\varphi}+\mathcal{G}^{(1,3)}e^{-2i\varphi}=\left|\mathcal{G}^{(3,1)}\right|\left(e^{i\arg\mathcal{G}^{(3,1)}}e^{2i\varphi}+e^{-i\arg\mathcal{G}^{(3,1)}}e^{-2i\varphi}\right) \tag{2.84}$$

$$=2\left|\mathcal{G}^{(3,1)}\right|\cos\left(2\varphi+\arg\mathcal{G}^{(3,1)}\right). \tag{2.85}$$

Fig. 2.10 shows the contributions from different correlation functions $\mathcal{G}^{(n,m)}$ to the resulting signal $F^{(k)}(\varphi)$ for the case of $m+n=4$.

From Eq. (2.82) it follows that the individual correlation moments $\mathcal{G}^{(n,m)}$ can be retrieved via Fourier transform as

$$\mathcal{G}^{(n,m)}=\frac{2^{k(d-1)}}{|\alpha_{\mathrm{LO}}|^k\binom{k}{n}}\frac{1}{2\pi}\int_0^{2\pi}F^{(n+m)}(\varphi)e^{-i(n-m)\varphi}\,\mathrm{d}\varphi\,. \tag{2.86}$$

2.6.2. Realistic Case

So far we have described the case of ideal 50:50 beam splitters, as is assumed in [SV06]. We will now consider the more realistic case of non-ideal splitting ratios and an individual transmission τ_j towards the j-th photodiode. We will include losses of the signal beam and demonstrate that they only act as an attenuation factor. The goal of this section is to both increase our understanding of the influence of experimental limitations, and to derive which experimental constants need to be considered to calibrate our measured correlation moments later.

We simulate losses in the signal beam during the path from the source to the BHC device by an imaginary beam splitter before the BHC scheme, see Fig. 2.11. The signal field is transformed as

$$\hat{a}\to\sqrt{\eta_{\mathrm{Si}}}\,\hat{a}+\sqrt{1-\eta_{\mathrm{Si}}}\,\hat{b}, \tag{2.87}$$

where η_{Si} is the intensity transmission of the imaginary beam splitter and $1-\eta_{\mathrm{Si}}$ models the introduction of vacuum described by the annihilation operator $\hat{b}$. We can, however, neglect the added vacuum term for correlation measurements due to the normal ordering.

Additionally, we treat losses experienced upon entering the device and on the path towards the first beam splitter with an efficiency η_{pre}, which we assume to apply equally to the signal beam as to the LO for simplicity (see also Fig. 2.11). These losses are relevant

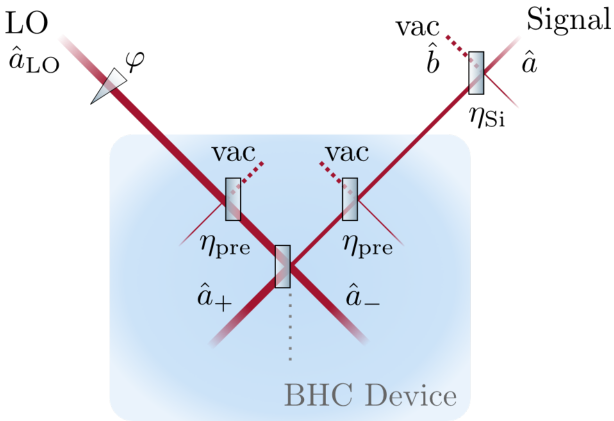

Figure 2.11.: Scheme to model the influence of losses on the signal beam before the BHC device, and on signal beam and LO inside the device before the first beam splitter.

when the BHC device is not made of free space bulk optics, so that input-coupling losses or propagation losses matter. The left-hand and right-hand outputs of the first beam splitter are now

$$\hat{a}_+ = \tau_0\sqrt{\eta_{\mathrm{Si}}\eta_{\mathrm{pre}}}\,\hat{a} + \rho_0\sqrt{\eta_{\mathrm{pre}}}\hat{a}_{\mathrm{LO}} \tag{2.88}$$

$$\hat{a}_- = \rho_0\sqrt{\eta_{\mathrm{Si}}\eta_{\mathrm{pre}}}\,\hat{a} - \tau_0\sqrt{\eta_{\mathrm{pre}}}\hat{a}_{\mathrm{LO}}, \tag{2.89}$$

where τ_0 and ρ_0 are the amplitude transmission and reflection of the first beam splitter, with $|\tau_0|^2 + |\rho_0|^2 = 1$. We assume them to be real valued, with the phase of the beam splitter contained entirely in the minus sign in Eq. (2.89). All introduced loss factors will only act as scaling factors on the measured moments.

The propagated modes arriving at the photodetectors are given by

$$\hat{a}_{j,\pm} = \tau_j e^{i\phi_j}\hat{a}_\pm + \mathrm{vac.} \tag{2.90}$$

Here τ_j is the amplitude transmission after the first beam splitter to the j-th photodiode and includes asymmetric splitting ratios of the subsequent beam splitters as well as individual losses in the different paths. An arbitrary phase ϕ_j along the j-th path is added.

Rather than measuring the photocurrents themselves, in the measurements we record voltages proportional to the photocurrents according to $\hat{V}_j = C_{\mathrm{Diode}}\,\hat{n}_j$, where C_{Diode} contains all detector constants. We assume all diodes to have identical constants for simplicity. The k-fold correlation functions to be measured now read as

$$\Gamma_{j_1,\ldots,j_k}(\varphi) = \left\langle : \hat{V}_{j_1} \cdots \hat{V}_{j_k} : \right\rangle \tag{2.91}$$
$$= C_{\text{Diode}}^k \left\langle : \hat{a}_{j_1}^\dagger \hat{a}_{j_1} \cdots \hat{a}_{j_k}^\dagger \hat{a}_{j_k} : \right\rangle \tag{2.92}$$
$$= C_{\text{Diode}}^k \tau_{j_1}^2 \cdots \tau_{j_k}^2 \left\langle : \hat{n}_+^l \hat{n}_-^{k-l} : \right\rangle \tag{2.93}$$

and show an unwanted dependency on the individual detectors chosen due to the individual transmission coefficients. Without correction, the terms in the binomial construction $F^{(k)}$ would then have individual prefactors and could not be reduced to the difference of left-hand and right-hand photocurrents, as before, thereby adding-in unwanted extra correlation terms.

Experimentally, we will overcome this difficulty by balancing all recorded voltages $\hat{V}_j$ with $\bar{\tau^2}/\tau_j^2$, where $\bar{\tau^2}$ is the arithmetic mean of transmission from the first beam splitter to the diodes, taken over all j. The correlation function now becomes

$$\Gamma'_{j_1,\ldots,j_k}(\varphi) = C_{\text{Diode}}^k \left\langle : \frac{\bar{\tau^2}}{\tau_{j_1}^2} \hat{a}_{j_1}^\dagger \hat{a}_{j_1} \cdots \frac{\bar{\tau^2}}{\tau_{j_k}^2} \hat{a}_{j_k}^\dagger \hat{a}_{j_k} : \right\rangle \tag{2.94}$$
$$= \left(C_{\text{Diode}} \bar{\tau^2} \right)^k \left\langle : \hat{n}_+^l \hat{n}_-^{k-l} : \right\rangle, \tag{2.95}$$

which again allows the binomial construction

$$F'^{(k)}(\varphi) = \sum_{l=0}^{k} (-1)^{k-l} \binom{k}{l} \Gamma_l'^{(k)} \tag{2.96}$$
$$= \left(C_{\text{Diode}} \bar{\tau^2} \right)^k \left\langle : (\hat{n}_+ - \hat{n}_-)^k : \right\rangle. \tag{2.97}$$

We will now discuss the relevance of high-pass (AC) filtering for the case of the unbalanced first beam splitter. Without filtering, the left- and right-hand photon number operators follow from Eqs. (2.88) and (2.89) as

$$\begin{aligned} \hat{n}_+ &= \hat{a}_+^\dagger \hat{a}_+ = \tau_0^2 \eta_{\text{Si}} \eta_{\text{pre}}\, \hat{a}^\dagger \hat{a} + \rho_0 \tau_0 \sqrt{\eta_{\text{Si}}} \eta_{\text{pre}} \left(\alpha_{\text{LO}} \hat{a}^\dagger + \alpha_{\text{LO}}^* \hat{a} \right) + \rho_0^2 \eta_{\text{pre}} |\alpha_{\text{LO}}|^2 \\ \hat{n}_- &= \hat{a}_-^\dagger \hat{a}_- = \rho_0^2 \eta_{\text{Si}} \eta_{\text{pre}}\, \hat{a}^\dagger \hat{a} - \rho_0 \tau_0 \sqrt{\eta_{\text{Si}}} \eta_{\text{pre}} \left(\alpha_{\text{LO}} \hat{a}^\dagger + \alpha_{\text{LO}}^* \hat{a} \right) + \tau_0^2 \eta_{\text{pre}} |\alpha_{\text{LO}}|^2 \end{aligned} \tag{2.98}$$

and consequently the photon number difference reads as

$$\hat{n}_+ - \hat{n}_- = \left(\tau_0^2 - \rho_0^2\right) \eta_{\mathrm{Si}} \eta_{\mathrm{pre}}\, \hat{a}^\dagger \hat{a} + 2\rho_0 \tau_0 \sqrt{\eta_{\mathrm{Si}}} \eta_{\mathrm{pre}} \left(\alpha_{\mathrm{LO}} \hat{a}^\dagger + \alpha_{\mathrm{LO}}^* \hat{a}\right) + \left(\rho_0^2 - \tau_0^2\right) \eta_{\mathrm{pre}} |\alpha_{\mathrm{LO}}|^2. \tag{2.99}$$

In contrast to the ideal case, where only the middle part remained, i.e. the rotated signal quadrature, here additional terms appear describing self-interference of signal and LO respectively due to the missing balance of the first beam splitter. Issues arise in the exponentiation to the power of k, which becomes

$$\begin{aligned}(\hat{n}_+ - \hat{n}_-)^k = {} & \left(\rho_0^2 - \tau_0^2\right)^k \eta_{\mathrm{pre}}^k |\alpha_{\mathrm{LO}}|^{2k} + \\ & + 2^k \rho_0^k \tau_0^k \sqrt{\eta_{\mathrm{Si}}}^k \eta_{\mathrm{pre}}^k |\alpha_{\mathrm{LO}}|^k \hat{\chi}_\varphi^k + \left(\tau_0^2 - \rho_0^2\right)^k \eta_{\mathrm{Si}}^k \eta_{\mathrm{pre}}^k \left(\hat{a}^\dagger \hat{a}\right)^k + \\ + \left(\rho_0^2 - \tau_0^2\right)^{k-1} |\alpha_{\mathrm{LO}}|^{2(k-1)} & \left[2\rho_0 \tau_0 \sqrt{\eta_{\mathrm{Si}}} \eta_{\mathrm{pre}}\, |\alpha_{\mathrm{LO}}| \hat{\chi}_\varphi + \left(\tau_0^2 - \rho_0^2\right) \eta_{\mathrm{Si}} \eta_{\mathrm{pre}}\, \hat{a}^\dagger \hat{a}\right] + \ldots,\end{aligned} \tag{2.100}$$

where other operators than the wanted $\hat{\chi}_\varphi^k$ would be mixed-in and amplified by high powers of the LO amplitude.

We will now include the AC filtering by, first, linearising the signal field annihilation operator in terms of its (static) coherent displacement α and its fluctuations $\delta\hat{a}$, i.e. $\hat{a} \to \alpha + \delta\hat{a}$, and then dropping all constant terms in the photocurrents. With the new signal field number operator

$$\hat{a}^\dagger \hat{a} = \left(\alpha_{\mathrm{Si}}^* + \delta\hat{a}^\dagger\right) \left(\alpha_{\mathrm{Si}} + \delta\hat{a}\right) \tag{2.101}$$

$$= |\alpha_{\mathrm{Si}}|^2 + |\alpha_{\mathrm{Si}}| \delta\hat{\chi}_{\varphi_{\mathrm{Si}}} + \delta\hat{a}^\dagger \delta\hat{a}\,, \tag{2.102}$$

where $\varphi_{\mathrm{Si}} = \arg \alpha_{\mathrm{Si}}$, the left- and right-hand number operators from (2.98) become

$$\begin{aligned}\hat{n}_+ = {} & \tau_0^2 \eta_{\mathrm{Si}} \eta_{\mathrm{pre}} \left(|\alpha_{\mathrm{Si}}|^2 + |\alpha_{\mathrm{Si}}| \delta\hat{\chi}_{\varphi_{\mathrm{Si}}} + \delta\hat{a}^\dagger \delta\hat{a}\right) + \\ & + \rho_0 \tau_0 \sqrt{\eta_{\mathrm{Si}}} \eta_{\mathrm{pre}} \left(|\alpha_{\mathrm{LO}}| \delta\hat{\chi}_\varphi + |\alpha_{\mathrm{LO}}| X_\varphi\right) + \rho_0^2 \eta_{\mathrm{pre}} |\alpha_{\mathrm{LO}}|^2\end{aligned} \tag{2.103}$$

$$\begin{aligned}\hat{n}_- = {} & \rho_0^2 \eta_{\mathrm{Si}} \eta_{\mathrm{pre}} \left(|\alpha_{\mathrm{Si}}|^2 + |\alpha_{\mathrm{Si}}| \delta\hat{\chi}_{\varphi_{\mathrm{Si}}} + \delta\hat{a}^\dagger \delta\hat{a}\right) - \\ & - \rho_0 \tau_0 \sqrt{\eta_{\mathrm{Si}}} \eta_{\mathrm{pre}} \left(|\alpha_{\mathrm{LO}}| \delta\hat{\chi}_\varphi + |\alpha_{\mathrm{LO}}| X_\varphi\right) + \tau_0^2 \eta_{\mathrm{pre}} |\alpha_{\mathrm{LO}}|^2,\end{aligned} \tag{2.104}$$

with the classical and static quadrature of the signal field's coherent displacement $X_\varphi = e^{i\varphi} \alpha_{\mathrm{Si}}^* + e^{-i\varphi} \alpha_{\mathrm{Si}}$. AC filtering eliminates all offset terms not containing dynamic fluctuations, i.e. all terms without $\delta\hat{a}$, $\delta\hat{a}^\dagger$ or $\delta\hat{\chi}$. Further, we neglect all terms not scaling with the LO amplitude. Thereby only the $\pm\rho_0 \tau_0 \sqrt{\eta_{\mathrm{Si}}} \eta_{\mathrm{pre}}\, |\alpha_{\mathrm{LO}}| \delta\hat{\chi}_\varphi$ terms remain, and the high-pass filtered number operator difference becomes

$$\hat{n}_+ - \hat{n}_- = 2\rho_0\tau_0\sqrt{\eta_{\mathrm{Si}}}\eta_{\mathrm{pre}}\,|\alpha_{\mathrm{LO}}|\delta\hat{\chi}_\varphi, \tag{2.105}$$

with strong resemblance of the previous, ideal-case result. Similar then, we find

$$\left\langle :\delta\hat{\chi}_\varphi^k:\right\rangle = \sum_{l=0}^{k}\binom{k}{l}\mathcal{G}_{\mathrm{AC}}^{(l,k-l)}e^{-i(k-2l)\varphi}, \tag{2.106}$$

with the correlation function of the field's fluctuations $\mathcal{G}_{\mathrm{AC}}^{(n,m)} = \left\langle \delta\hat{a}^{\dagger n}\delta\hat{a}^m\right\rangle$. The BHC signal becomes

$$F'^{(k)}(\varphi) = \left(2\rho_0\tau_0\sqrt{\eta_{\mathrm{Si}}}\eta_{\mathrm{pre}}\,|\alpha_{\mathrm{LO}}|C_{\mathrm{Diode}}\bar{\tau^2}\right)^k\sum_{l=0}^{k}\binom{k}{l}\mathcal{G}_{\mathrm{AC}}^{(l,k-l)}e^{-i(k-2l)\varphi} \tag{2.107}$$

and we retrieve the wanted correlation functions via Fourier transform as

$$\mathcal{G}_{\mathrm{AC}}^{(n,m)} = \frac{1}{\left(2\rho_0\tau_0\sqrt{\eta_{\mathrm{Si}}}\eta_{\mathrm{pre}}\,|\alpha_{\mathrm{LO}}|C_{\mathrm{Diode}}\bar{\tau^2}\right)^k}\binom{k}{n}^{-1}\frac{1}{2\pi}\int_0^{2\pi}F'^{(n+m)}(\varphi)e^{-i(n-m)\varphi}\,\mathrm{d}\varphi\,. \tag{2.108}$$

In summary our treatment of the realistic case of unbalanced beam splitters and asymmetric losses has shown that, first, uneven transmissions τ_j after the first beam splitter, which would prevent a clean binomial construction of the BHC signal and thereby introduce unwanted extra correlation terms, can be adjusted for by determining all individual transmissions τ_j experimentally and scaling the measured voltages accordingly. Second, we saw that without AC filtering also unwanted extra moments would be introduced due to the unbalanced first beam splitter. With the AC filtering, however, the unwanted moments vanish and the beam splitter imbalance only introduces scaling factors. Third, we found that all introduced losses act only as scaling factors, as is typical for a correlative measurement.

2.7. Calculation of Correlation Moments of Squeezed Vacuum States

In this section we will calculate the correlation functions $\mathcal{G}^{(n,m)}$ for squeezed states, which will act as test states later for the BHC measurements. We reduce our calculations to $n+m=4$, which is the maximum order of correlation function our set-up with eight detectors allows to measure.

As pointed out above, due to the AC-filtering the measurement is only sensitive to correlations in the fluctuations. We will therefore calculate the correlation functions for the states with their coherent amplitude removed, i.e. the squeezed vacuum state with the same squeezing parameter ξ. The calculation is performed exemplarily for $\mathcal{G}^{(2,2)}$, the other correlation functions can be derived analogously.

We start our calculation with the definition of the $\mathcal{G}^{(2,2)}$ correlation function, expand the state according to the Heisenberg picture as $|\xi,0\rangle = \hat{S}(\xi)\,|0\rangle$ and introduce unities $1=\hat{S}(\xi)\hat{S}^{\dagger}(\xi)$ between the annihilation and creation operators,

$$
\begin{aligned}
\mathcal{G}^{(2,2)}_{|\xi,0\rangle} &= \langle \xi,0|\hat{a}^{\dagger}\hat{a}^{\dagger}\hat{a}\hat{a}|\xi,0\rangle && (2.109)\\
&= \langle 0|\,\hat{S}^{\dagger}(\xi)\,\hat{a}^{\dagger}\,\hat{S}(\xi)\quad \hat{S}^{\dagger}(\xi)\,\hat{a}^{\dagger}\,\hat{S}(\xi)\quad \hat{S}^{\dagger}(\xi)\,\hat{a}\,\hat{S}(\xi)\quad \hat{S}^{\dagger}(\xi)\,\hat{a}\,\hat{S}(\xi)\,|0\rangle\,. && (2.110)
\end{aligned}
$$

Now, we use the transformations of the creation and annihilation operator under the squeeze operator from Eqs. (2.36) and (2.37) and perform all multiplications

$$
\begin{aligned}
\mathcal{G}^{(2,2)}_{|\xi,0\rangle} &= \langle 0|\left(\cancel{\hat{a}^{\dagger}\cosh r} - \hat{a}e^{-i\vartheta}\sinh r\right)\left(\hat{a}^{\dagger}\cosh r - \hat{a}e^{-i\vartheta}\sinh r\right)\cdots\\
&\qquad\cdots\left(\hat{a}\cosh r - \hat{a}^{\dagger}e^{i\vartheta}\sinh r\right)\left(\cancel{\hat{a}\cosh r} - \hat{a}^{\dagger}e^{i\vartheta}\sinh r\right)|0\rangle\\
&= \langle 0|\Big[\hat{a}e^{-i\vartheta}\sinh r\;\hat{a}^{\dagger}\cosh r\;\hat{a}\cosh r\;\hat{a}^{\dagger}e^{i\vartheta}\sinh r\\
&\quad - \hat{a}e^{-i\vartheta}\sinh r\;\hat{a}^{\dagger}\cosh r\;\hat{a}^{\dagger}e^{i\vartheta}\sinh r\;\hat{a}^{\dagger}e^{i\vartheta}\sinh r\\
&\quad - \hat{a}e^{-i\vartheta}\sinh r\;\hat{a}e^{-i\vartheta}\sinh r\;\hat{a}\cosh r\;\hat{a}^{\dagger}e^{i\vartheta}\sinh r\\
&\quad + \hat{a}e^{-i\vartheta}\sinh r\;\hat{a}e^{-i\vartheta}\sinh r\;\hat{a}^{\dagger}e^{i\vartheta}\sinh r\;\hat{a}^{\dagger}e^{i\vartheta}\sinh r\Big]\,|0\rangle\,,
\end{aligned}
\tag{2.111}
$$

where we have immediately cancelled out the terms with an annihilation operator acting to the right on the vacuum, $\hat{a}\,|0\rangle = 0$, or with an creation operator acting to the left on the vacuum, $\langle 0|\,\hat{a}^{\dagger} = 0$. Using the commutator relations we can evaluate all expectation values of the products of annihilation and creation operators

$$\langle 0|\hat{a}\hat{a}^\dagger\hat{a}\hat{a}^\dagger|0\rangle = \langle 0|\hat{a}\hat{a}^\dagger|0\rangle = 1 \tag{2.112}$$

$$\langle 0|\hat{a}\hat{a}^\dagger\hat{a}^\dagger\hat{a}^\dagger|0\rangle = \langle 0|\hat{a}^\dagger\hat{a}^\dagger|0\rangle = 0 \tag{2.113}$$

$$\langle 0|\hat{a}\hat{a}\hat{a}\hat{a}^\dagger|0\rangle = \langle 0|\hat{a}\hat{a}|0\rangle = 0 \tag{2.114}$$

$$\langle 0|\hat{a}\hat{a}\hat{a}^\dagger\hat{a}^\dagger|0\rangle = \langle 0|(\hat{a}\hat{a}^\dagger + \hat{a}\hat{a}^\dagger\hat{a}\hat{a}^\dagger)|0\rangle = 2. \tag{2.115}$$

With only the first and last term in (2.111) remaining, the correlation function becomes

$$\mathcal{G}^{(2,2)}_{|\xi,0\rangle} = \cosh^2 r\ \sinh^2 r + 2\sinh^4 r. \tag{2.116}$$

The other correlation functions $\mathcal{G}^{(n,m)}$ are calculated analogously and are found in table 2.1.

(n,m)	$\mathcal{G}^{(n,m)}_{\vert\xi,0\rangle}$
$4,0$	$3e^{-2i\vartheta}\cosh^2 r\ \sinh^2 r$
$3,1$	$-3e^{-i\vartheta}\cosh r\ \sinh^3 r$
$2,2$	$2\sinh^4 r + \cosh^2 r\ \sinh^2 r$
$1,3$	$-3e^{i\vartheta}\cosh r \sinh^3 r$
$0,4$	$3e^{2i\vartheta}\cosh^2 r\ \sinh^2 r$

Table 2.1.: Correlation functions of the squeezed vacuum for $n + m = 4$.

We note that $\mathcal{G}^{(2,2)}$ is the only correlation function independent of squeezing angle. It is entirely real valued, as is expected due to its Hermiticity. The other, non-Hermitian correlation functions with $n \neq m$ show complex values with a constant phase determined by the squeezing angle. As expected, correlation functions with flipped indices are complex conjugates.

All functions are shown in Fig. 2.12 for varied squeezing strengths for an arbitrarily chosen squeezing angle of $\vartheta = 15°$, with the absolute value (on linear and logarithmic axes) plotted separately from the complex argument. In linear units the correlations grow exponentially with squeezing strength, as expected from the sinh and cosh functions. For vanishing squeezing strength the state approaches the vacuum state and correlations disappear. On the logarithmic scale the functions converge with growing squeezing strength. The complex arguments are constant and, for flipped indices, opposite to each other.

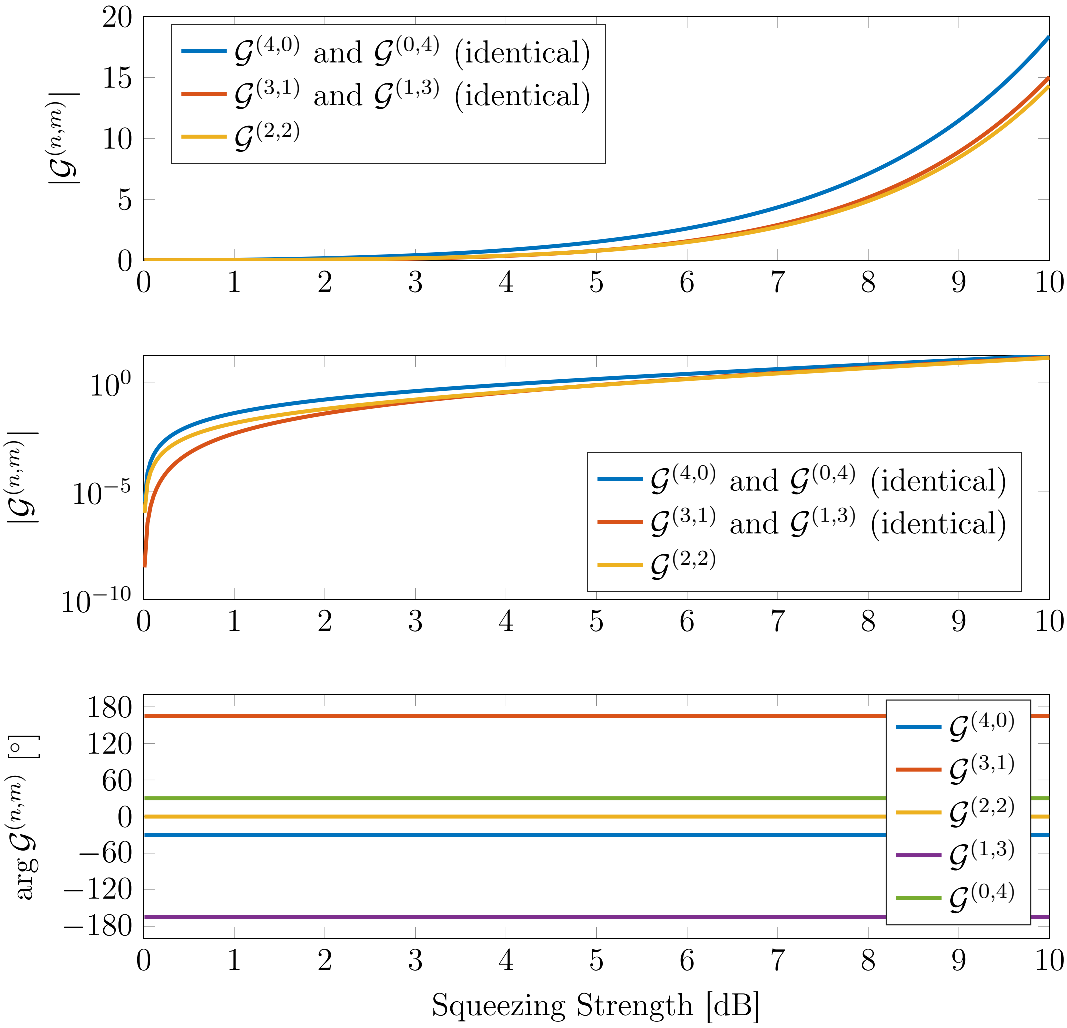

Figure 2.12.: Bode plots of the expected correlation functions for squeezed vacuum for varying squeezing strength. An arbitrary squeezing angle of $\vartheta = 15°$ was chosen. Top: Plot of absolute values on linear axis, showing exponential growth as expected from the sinh and cosh functions. Middle: Plot of absolute values on logarithmic axis. For strong squeezing the correlation functions converge. Bottom: Phase plot of the correlation functions. Phases are constant, and, for flipped indices, opposite to each other.

3. Experimental Set-Up

In chapter 2 we have taken a detailed look at the balanced homodyne correlation (BHC) method from the theoretical side and added considerations of the experimental limitations. Now we will move on to the experimental implementation and give insight into the development process. In this introduction we will first give an overview of the different components necessary, before we delve into more detailed descriptions in the following subsections.

Following Fig. 3.1, the first component in our set-up is the laser. We use the Innolight Diabolo, a Nd:YAG solid state laser, with a non-planar ring oscillator providing high frequency stability ($\approx 2\,\mathrm{MHz/min}$) and narrow linewidth ($\approx 1\,\mathrm{kHz}$). Infrared light at 1064 nm is directly produced while frequency doubled green light at 532 nm is provided by an integrated second harmonic generation unit. Both outputs are additionally spatially and spectrally filtered by following mode-cleaner ring resonators (not shown), providing a clean TEM_{00} mode. The lengths of the mode-cleaner cavities are stabilised using the Pound-Drever-Hall (PDH) scheme [Dre$^+$83; Bla01].

The next step is the state preparation. With squeezed light sources already available in the workgroup's laboratory, it was decided early on that squeezed light was to be used as a nonclassical test state for our BHC set-up. We use an optical parametric amplifier (OPA) to generate squeezed light at 1064 nm, with a PPKTP (*periodically poled potassium titanyl phosphate*) second order nonlinear crystal inside a standing-wave cavity resonant for the infrared light. The length of the cavity is locked onto resonance using a weak 1064 nm control beam of typically 500 µW with the PDH scheme. The control beam also adds a small coherent displacement of typically $< 10\,\mu\mathrm{W}$ to the output. The required nonlinear polarisation in the medium is generated by the strong 532 nm pump field of typically 50 mW to 200 mW. By use of a flip mirror the created signal beam can be sent either to the balanced homodyne detection (BHD) set-up for characterisation or to the BHC scheme for correlation measurements.

To characterise the signal field, i.e. measure the strength of the created squeezing, the flip mirror is removed and the signal field is sent to the balanced homodyne detector. As described in the theory section 2.5, the signal field is combined with the much stronger LO at a 50:50 beam splitter. Control of the LO phase is achieved by a piezo-mounted mirror which can be moved back and forth to create differences in path length. A ramp signal controls the piezo and is recorded to ease phase retrieval later. The photodiodes

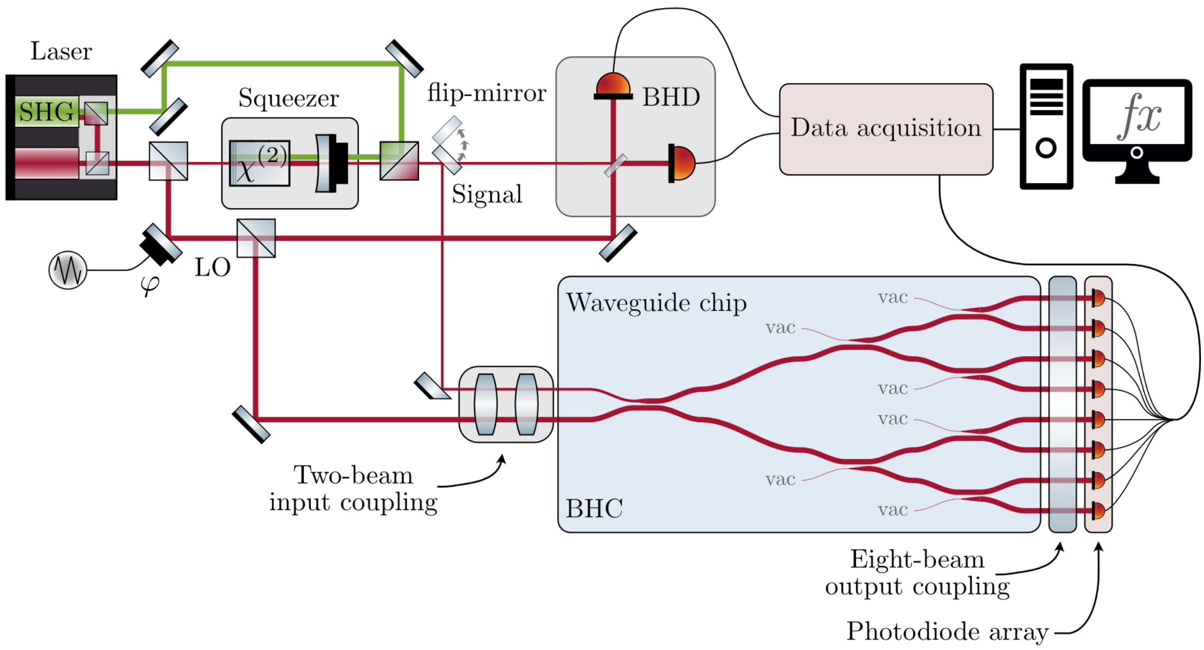

Figure 3.1.: Overview of the set-up used to perform BHC measurements. First, a test state (displaced squeezed-, coherent-, or vacuum state) is generated as signal beam using an OPA (squeezer). If the flip mirror is opened, the signal beam is sent to the BHD scheme for characterisation (measurement of squeezing strength). When the flip mirror is closed, the signal beam is sent to the BHC scheme, implemented in a laser direct written waveguide chip. Finally, the eight outputs are detected by a photodiode array. For the data acquisition fast digitizer cards are used. Special care is taken of the input coupling of signal beam and local oscillator (LO) into the waveguide chip, where both mode field diameter and waveguide pitch have to be matched, and the output coupling from the waveguide chip to the photodiode array, where the waveguide pitch has to be matched to the diode array pitch. The eight-fold output of the waveguide chip can alternatively, via a flip mirror, be sent to a camera (not shown) for analysis of the waveguide's output modes.

need to be approximately identical in frequency-dependent transfer functions, and in quantum efficiency. The measurement data is recorded via a fast two channel oscilloscope card for the high-pass filtered outputs (AC) of the diodes, while an additional slower digitizer card provides channels for the low-pass filtered outputs of the diodes (DC) and the phase ramp control signal.

After the characterisation the flip mirror is placed again and the signal beam is passed to the BHC scheme. As described in the theory section, a 50:50 beam splitter combines the signal beam with the LO, and subsequent 50:50 beam splitters further split the beams into eight outputs with approximately equal power. Here the scheme has been realized in an integrated waveguide structure, produced by direct laser writing. While the waveguide chip is approximately $150\,\mathrm{mm} \times 20\,\mathrm{mm} \times 1\,\mathrm{mm}$ in size, the particular realisations of the BHC scheme inside only need ca. 1 mm of the available width, so structures written with different parameters can be housed simultaneously. The LO phase is controlled again by the same piezo-mounted mirror used for the BHD scheme.

The output beams are detected by a 1x8 array of fast photodiodes, with individual photodiodes spaced 250 µm apart. The electric signals are amplified by a low noise and high speed eight channel transimpedance amplifier, with near identical transfer functions for all channels. To allow precise positioning of the diode array a mount allowing 3D translation and 1D rotation is used. A camera set-up in parallel to the photodiode detector (not shown) proved highly useful, especially for adjustments of the chip position.

The AC filtered outputs of the photodiode array are sampled at 50 MHz by a National Instruments 5751B digitizer, used with a reconfigurable PXIe-7962R FPGA (*field programmable gate array*) module. Additionally the phase ramp signal and DC signal of one photodiode are sampled at 10 kHz.

The coupling into the waveguide chip and from the chip to the detector posed a technical challenge. In the input coupling the two free space beams (LO and signal) have to be matched to the required mode field diameter of the waveguides while meeting the spacing (pitch) between the waveguides of 125 µm. Further in the output coupling the eight beams from the chip at a spacing of 125 µm have to be matched to the 250 µm pitch of the photodiode array. Confocal lens set-ups were found to be a satisfying solution, as in this case beams running in parallel will remain parallel in the output. Thereby the overall adjustment was substantially alleviated.

3.1. Optical Parametric Amplifier

In the theory section we have introduced squeezed states via the squeezing operator in Eq. (2.32). We will now discuss one way of realising this transformation via nonlinear optics. We will first give a brief theoretical description of optical parametric amplification and then give a short technical account of the experimental implementation, showing which parameters will be important in our measurements.

When an electro-magnetic field passes an optical medium, the charges of the medium are polarised in response to the field. Conventionally the polarisation will be linear in the incident field strength and show the same frequency components. However, if the incident field is highly intense[1], nonlinear (inharmonic) contributions to the polarisation become relevant, which depend on higher orders of the electric field strength. Additional frequency components are thereby added to the polarisation as combinations of the incident frequencies. The nonlinear polarisation couples back to the electric field and drives an electric field at the new frequency components. Focusing on second order nonlinear effects now, a typical application is e.g. second harmonic generation, in which a field at the doubled frequency is generated from the strong fundamental frequency field, as e.g. used in the frequency doubling unit of our laser. We refer to [Boy08] for detailed classical and quantum optical descriptions of the nonlinear processes.

Here we will use the second order effect of difference frequency generation in an optical parametric amplifier (OPA). Archetypically three fields are involved at frequencies ω_1, ω_2 and ω_3, with $\omega_1 = \omega_2 + \omega_3$ for energy conservation. The fields are usually referred to as pump, signal and idler, where the pump field has a high intensity and drives the nonlinear interaction, the signal field is the field to be amplified or attenuated, and the idler field with $\omega_3 = \omega_1 - \omega_2$ carries away surplus energy.

To generate a squeezed state we will use a *degenerate* parametric amplifier, where signal and idler are identical, i.e. are only a single field (we will still call it the signal field) at the fundamental frequency ω, while the pump field has the frequency $\omega_\mathrm{P} = 2\omega$. In the nonlinear interaction of the fields a photon from the pump field can be converted to two photons in the signal field, and equivalently two photons from the signal field can be converted to one photon in the pump field.

[1]...at the latest when the force on the charges induced by the incident field strength becomes comparable to the atomic forces within the medium [Boy08]...

Following [GK05], the Hamiltonian of the degenerate OPA is

$$\hat{H} = \hbar\omega\hat{a}^\dagger\hat{a} + \hbar\omega_{\mathrm{P}}\hat{b}^\dagger\hat{b} + i\hbar\chi^{(2)}(\hat{a}^2\hat{b}^\dagger - \hat{a}^{\dagger 2}\hat{b}), \tag{3.1}$$

where the first two terms are the energies contained in the two fields (barring static vacuum energy), and the third term describes the interaction between the fields, with the second order nonlinear susceptibility of the crystal $\chi^{(2)}$. Assuming the pump field to be in a coherent state, and to remain undepleted, i.e. to not be affected by the interaction, we can replace the operator valued pump amplitude with its c-number valued coherent amplitude, $\hat{b} \to \beta$. By further switching to the interaction picture the third term is isolated in the interaction Hamiltonian

$$\hat{H}_{\mathrm{I}} = i\hbar\chi^{(2)}(\beta^*\hat{a}^2 - \beta\hat{a}^{\dagger 2}). \tag{3.2}$$

The unitary time evolution operator becomes

$$\hat{U}_{\mathrm{I}}(t,0) = \exp\left(-i\hat{H}_{\mathrm{I}}t/\hbar\right) = \exp\left[\chi^{(2)}t\left(\beta^*\hat{a}^2 - \beta\hat{a}^{\dagger 2}\right)\right] \tag{3.3}$$

and is equivalent to the squeezing operator from Eq. (2.32), with the squeezing parameter now given as $\xi/2 = \chi^{(2)}t\beta$. We find the squeezing angle $\vartheta = \arg\xi$ to depend on the phase of the pump field $\varphi_{\mathrm{P}} = \arg\beta$. In the experiment we will carefully control the pump field phase with respect to the signal field via a feedback loop to set the squeezing angle.

In Eq. (3.3) the magnitude of the squeezing is influenced by three factors. The first factor is the nonlinear susceptibility of the crystal. Here $\chi^{(2)}$ is a shorthand notation for the susceptibility for a particular choice of field polarisations and crystal axis used. These parameters are optimised in the design of the BHD.

The second ingredient is the coherent amplitude β of the pump field. This parameter is easily accessible in experiment as a dial to set the squeezing strength. An upper limit is given by the threshold going from optical parametric amplification, for weaker pump strengths, to optical parametric oscillation, for high intensities. At this point the signal field experiences higher than unity net gain per round trip, $g \geq 1$, and becomes self-seeding, causing e.g. the noise in the amplified quadrature to diverge [BR19]. In our case a limit was reached much earlier due to uncompensated instabilities of the electric feedback loops for high optical gains in the nonlinear medium.

The third parameter is the duration of the interaction t. In our experiment the interaction time is increased as the signal field passes the nonlinear crystal twice per round trip.

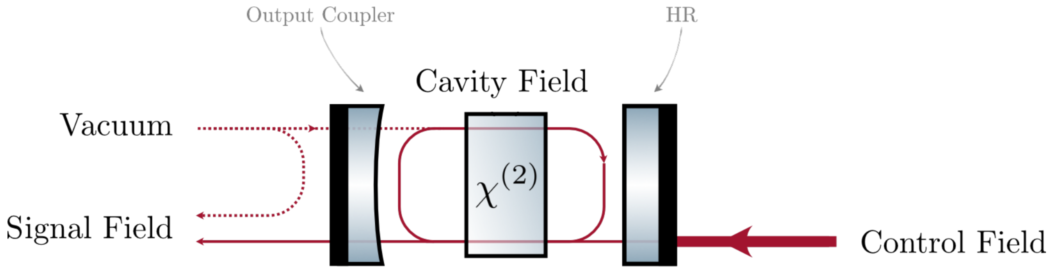

Figure 3.2.: Interference of the cavity field leaving the resonator through the output coupling mirror with the directly reflected vacuum field incident on the cavity from the left. The cavity field's fluctuations are predominantly determined by the vacuum field entering from the left side and not by the control field, due to the asymmetric reflection coefficients of the mirrors.

Another important benefit of the resonator, which is not shown in Eq. (3.3), is that the quadrature fluctuations of the cavity field leaving the resonator through the output coupling mirror can interfere destructively with the fluctuations of the vacuum field directly reflected off the same mirror (see Fig. 3.2 for illustration). For appropriately chosen cavity parameters the fluctuations in the squeezed quadrature can be significantly reduced further this way.

3.1.1. Set-Up of the Optical Parametric Amplifier

We will now describe the BHD used in this work as schematically shown in Fig. 3.3. It was built by Steve Jäger for his master's thesis in 2015 [Jäg15] with supervision from Melanie Schünemann. Squeezed light can be created at the infrared fundamental wavelength of 1064 nm, using a pump field of visible green light at 532 nm.

The centerpiece is a nonlinear PPKTP (*periodically poled potassium titanyl phosphate*) crystal with strong $\chi^{(2)}$ susceptibility, used with quasi-phase-matching (see e.g. [Boy08] for explanations on phase matching and corresponding techniques). It features an anti-reflective (AR) coating on one end facet (left side), and a highly reflective (HR) coating on the other end facet (right side), both effective at 1064 nm and 532 nm. A so-called *hemilithic* cavity is formed between the crystal's HR coating and a curved outcoupling mirror on the left side with ca. 90 % reflectivity for the fundamental field and ca. 20 % reflectivity for the harmonic field.

The cavity is locked onto resonance for the fundamental field with the PDH method, while the harmonic field experiences weak resonance. Further a Peltier element connected

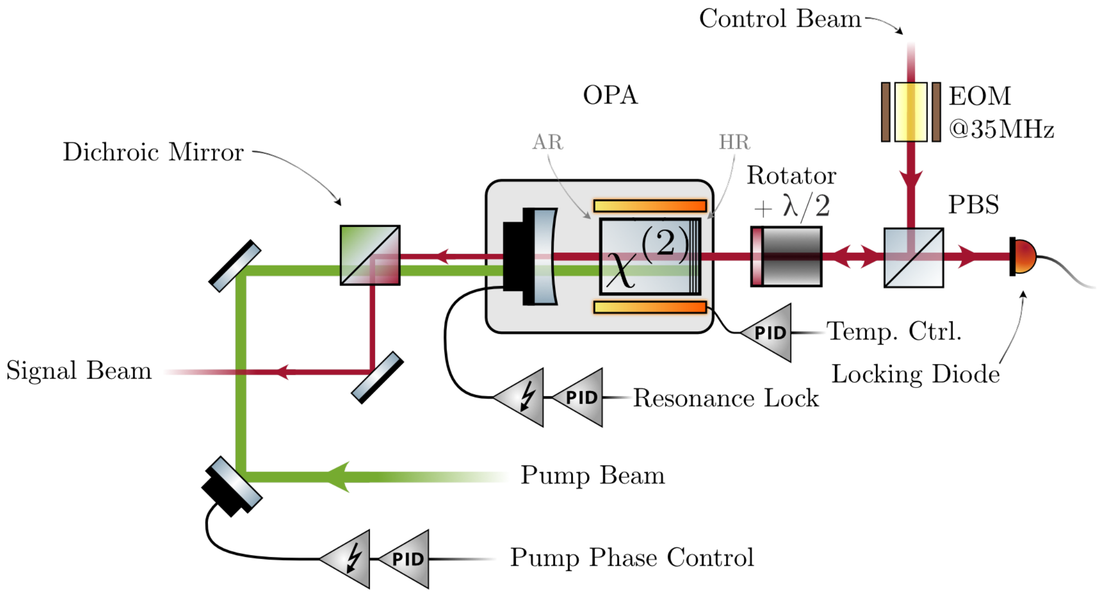

Figure 3.3.: Optical layout of the OPA used to generate the squeezed light. A PPKTP $\chi^{(2)}$ nonlinear crystal forms a hemilithic resonator between the curved outcoupling mirror and the crystal's highly reflective coated end facet on the right-hand side. The PDH method is employed to lock the cavity onto resonance for the fundamental field. With a Peltier element the quasi-phase-matching temperature is set. The weak control beam at the fundamental 1064 nm wavelength allows resonance control and adds a coherent displacement to the signal output of the OPA. The nonlinear process is driven by the harmonic pump field at 532 nm. The pump phase, and thereby the quadrature angle of parametric amplification or de-amplification, is set and stabilised by a closed loop controller.

to a closed loop temperature controller is employed to set the crystal temperature for phase-matching.

We will now describe the fields involved in the nonlinear interaction. First, a weak control beam in a coherent state at the 1064 nm fundamental wavelength allows resonance control of the cavity. An electro-optic modulator (EOM) applies a phase modulation at 35 MHz to the beam and thereby introduces the side bands required for the PDH scheme. The control beam's power can be set by a $\lambda/2$ plate + polarising beam splitter (PBS) combination. The beam is initially s-polarised and reflected by a PBS towards the cavity. The beam passes a combination of a Faraday rotator and a $\lambda/2$ plate, leaving the polarisation unchanged as it reaches the HR end facet of the nonlinear crystal. While a small portion passes into the resonator, most of its intensity is reflected. The beam passes the rotator combination again and leaves in p-polarisation, *passes* the PBS and is detected by a photodiode for the locking scheme. The control beam introduces a small coherent displacement (few µW) to the output signal field.

The second field of consideration is the strong coherent pump field at the 532 nm harmonic wavelength. The pump field power can be set by a $\lambda/2$ + PBS combination. The relative phase is controlled by a piezo-mounted mirror with a feedback loop via the same locking diode as used for the resonance lock. We can thereby dial in the quadrature angles of parametric amplification and de-amplification and hence the angle of the squeezing ellipse. Both parametric amplification of the control field, causing phase squeezing and amplitude anti-squeezing is available, as well as parametric deamplification, causing amplitude squeezing and phase anti-squeezing, and also settings in between.

In this work we will only use parametric deamplification, i.e. amplitude squeezing, as it is the most compatible with measurements in homodyne approximations as made in BHD and BHC, where the LO is assumed to be much stronger than the signal field. With our photodiodes typically operated in the 1 mW regime of incident optical power, signal beam powers are preferred in the low µW range, lending themselves to parametric attenuation.

Both fields are coupled out of the cavity by the coupling mirror and are separated spatially by a dichroic mirror. If the OPA is operated without the pump field, the signal beam is in a coherent state.

3.2. Waveguide Chip

We will now describe our implementation of the beam splitter cascade of the BHC scheme. A waveguide chip is used, as it naturally offers compactness, stability, and scalability. The optical adjustments are limited to modematching the signal and LO beam to the correct waveguide mode, and matching the pitch (spacing) of the output modes to the pitch of the photodiode array. The individual beam splitters are set via the writing process, with no individual adjustments necessary. Further all output modes will have the same mode shape. Last but not least an integrated waveguide solution promises high scalability, especially compared to a bulk optics solution, so that the scheme can be expanded later to 16 outputs or more.

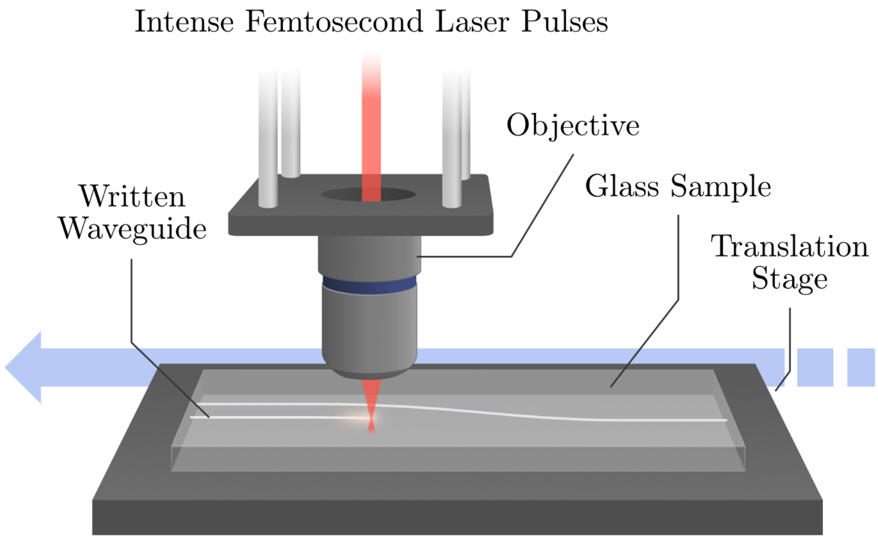

Figure 3.4.: Schematic of the femtosecond writing process. Intense femtosecond laser pulses are focused into the bulk material (fused silica) and induce a local increase in refractive index. Transversal movement of the sample allows the writing of waveguide structures. Illustration reprinted with kind permission of Karo Becker from the workgroup Experimental Solid-State Optics.

3.2.1. Femtosecond Laser Writing of Waveguide Structures

We will first briefly introduce the basics of the direct writing process following [SN10]. In femtosecond laser writing, ultrashort laser pulses are focused into a bulk optical substrate – in this case fused silica. An illustration is shown in Fig. 3.4. The high peak intensities made available by femtosecond lasers lead to a nonlinear (multiphoton) absorption, causing optical breakdown and the formation of a micro plasma. Fused silica consists of ring shaped molecules, made up of multiple SiO_2 molecules. In the nonlinear process, the ring structures are broken up, and the SiO_2 molecules recombine in smaller rings, made up of less constituents. The density of the material is thereby increased, leading to a locally increased refractive index. Moving the sample with respect to the laser beam, in our case transverse to it, creates a waveguide along the chosen path.

For the nonlinear process a threshold in intensity has to be reached, which is only available in the focus region. The area of increased refractive index is therefore described by the waist radius of the focused beam and its Rayleigh range. With Rayleigh range exceeding the waist radius, the waveguide area is oval-shaped, and so is the guided mode of light.

While the light is trapped by the area of increased refractive index, not all of it is confined within the waveguide. A part of the mode is guided outside of the waveguide as an evanescent tail, with its intensity exponentially decaying with increased distance from the waveguide, and can be used to interact with other waveguides.

If two waveguides are brought closely enough together, so that there is significant overlap of their modes, energy can flow between them, weakening one field and strengthening the other. This interaction is called evanescent coupling. We will use this feature to construct directional couplers, acting as beamsplitters [SB01]. In coupled mode theory it is assumed, that the mode in one waveguide is found independently from the presence of other waveguides [ST19]. During the interaction of nearby waveguides then, only the amplitudes of the modes in the waveguides evolve with interaction distance z. Assuming all power to be initially in the first waveguide, the powers in the waveguides 1 and 2 will vary as

$$P_1 = P_0 \cos^2(\zeta z) \tag{3.4}$$

$$P_2 = P_0 \sin^2(\zeta z), \tag{3.5}$$

where ζ is a coupling coefficient depending on the overlap of the evanescent modes and P_0 is the initial power. It is possible therefore to tune the power transfer by setting the coupler length z [ST19].

3.2.2. A Waveguide Chip for Balanced Homodyne Correlation

We will now describe the iterative design process to manufacture a waveguide chip implementing the beam splitter cascade for BHC measurements via femtosecond laser writing. The chip was developed in cooperation with Tom A. W. Wolterink and Max Ehrhardt from the workgroup Experimental Solid-State Optics of Prof. Dr. Alexander Szameit at the Institute of Physics in Rostock. The waveguides were written using a Coherent Monaco 517 – a femtosecond laser for industrial applications e.g. in micro-machining. The material to be manipulated was Corning C7980 fused silica glass. The chips were developed in a feedback process between writing in the fs-laser lab and testing in the squeezer lab, so that the created structures work optimally for the actual set-up in question. The iterative process from finding writing parameters to producing the resulting beam splitter cascade was performed in a single glass chip to ensure that the material conditions do not change between structures.

Powerscan

The first step is to find the correct writing parameters to produce well guiding structures for 1064 nm. For that purpose straight waveguides completely spanning the glass chip are written for varying writing parameters, as shown in Fig. 3.5. In this case only the power of the fs-laser was varied. For testing the 1064 nm laser to be used for BHC measurements is coupled into each waveguide individually and the output is focused onto a camera. We select the writing power which produced optimal guiding, i.e. a clean mode shape and low losses (see Fig. A.1 in appendix).

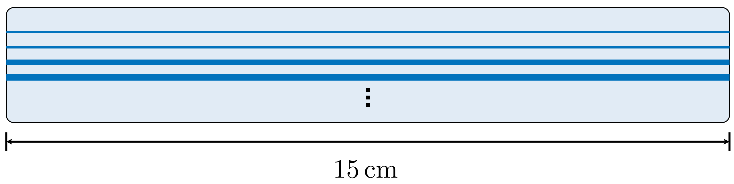

Figure 3.5.: Power scan. Straight waveguides are written with different laser powers. The candidates are then tested with light at 1064 nm for optimal guiding.

Straight Coupler Distance Scan

We now probe the coupling between neighbouring waveguides to find the coupler parameters. We start with one straight waveguide completely spanning the chip as before, but a short second straight waveguide is added over the last 10 mm, as shown in Fig. 3.6. The transverse distance between the two waveguides is iteratively increased from 20 µm to 50 µm. This results in a variation from overcoupling, i.e. more than 50 % of the power is transferred to the second waveguide, to undercoupling, where less than 50 % is transferred.

The structures are then tested in the squeezer lab with the 1064 nm laser by individually probing the couplers and focusing their output onto a camera. The relative powers of the two outputs are determined and the coupler distance yielding closest to 50:50 coupling is selected as a starting point. The polarisation of the guided light influences the coupling ratios – here the couplers were designed for p-polarised light.

Figure 3.6.: Straight coupler distance scan. A short section of parallel straight waveguides is written. The distance of the waveguides is varied in a sequence. Analysis of the power distribution between the two waveguides for 1064 nm light gives a first estimate of the coupler dimensions.

Curvy Coupler Length Scan

As shown in Fig. 3.7, in the final scheme the couplers will only have a straight parallel section in the middle, while the individual waveguides have to curve in, at the approach, and out, at the departure. The coupling, however, is not limited to the parallel section, with a significant portion of the total coupling achieved in the curved sections where they are still close enough together for sufficient evanescent overlap. This becomes especially apparent when considering that the widening from the coupling distance of 28 µm to the standard pitch of 125 µm is stretched out over ca. 14 mm on both approach and departure to minimise the increased losses occurring in bending parts of the waveguides. The effective interaction length is thereby significantly increased, and the coupler length used before (10 mm) would yield strong overcoupling.

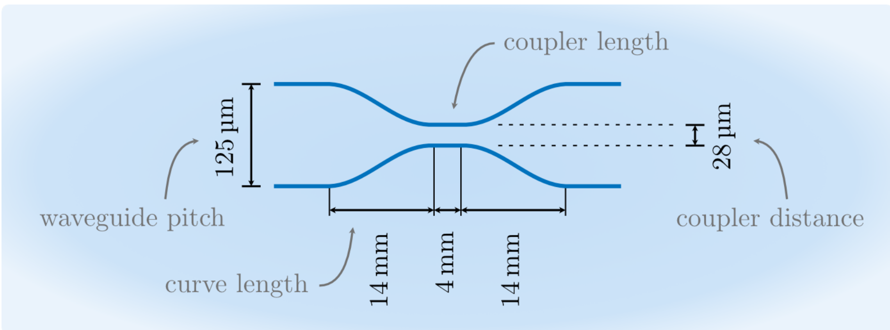

Figure 3.7.: Curved coupler scheme. Only a short segment of the waveguides in the middle is parallel. Significant coupling occurs already in the curved sections, yielding a longer effective coupling length. To avoid overcoupling the coupler length needs to be shortened. Dimensions are given for the final version of the chip.

To investigate the influence of the curves we will now write a sequence of curved couplers with varying parallel coupler length as shown in Fig. 3.8. The input waveguide is straight for the most part of the chip length and only at the end is brought together with a shorter second waveguide in the curved coupler scheme. The coupling at 1064 nm is analysed as before and an ideal coupling length is selected. As shown in Fig. 3.7 the ideal parallel coupler length was ca. 4 mm with a waveguide separation of 28 µm.

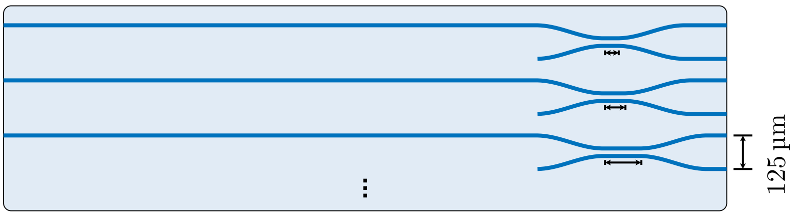

Figure 3.8.: Curvy coupler length scan. With effective interaction length increased due to the curved approach and departure of the waveguides, the parallel segment of the couplers needs to be shortened. A sequence of curved couplers is written with varying parallel coupler length. Analysis of the power distribution of the outputs allows selection of ideal coupler parameters.

Repetitions of 2x8 Structures

With writing and coupling parameters known, the beam splitter cascade with two accessible inputs and eight outputs can be written.We will first give a description of the scheme as seen in Fig. 3.9. The LO and the signal beam will be coupled in via the front facet, here on the left, and are combined in the first directional coupler. The now mixed outputs are separated in space with back to back curves as used in the couplers. The beams are then further divided by subsequent couplers. All directional couplers are identical and the structure is completely symmetrical with respect to an imagined middle line dividing the inputs. The inputs and outputs are spaced at the waveguide pitch of 125 µm. The output array spans $7 \cdot 125\,\mu\text{m} = 875\,\mu\text{m}$ in total. Over the transverse chip width of 20 mm multiple versions of the 2x8 structure can be written.

To ensure a version with ideal coupling and without defects is created, the 2x8 structure is repeated multiple times, as indicated in Fig. 3.9. This is a precaution to accommodate for possible changes of parameters during the writing process. The coupling length of the curved couplers is varied in small steps of 0.05 mm around the considered ideal length of 4 mm. The resulting structures are again analysed with light at 1064 nm to select a version with ideal splitting.

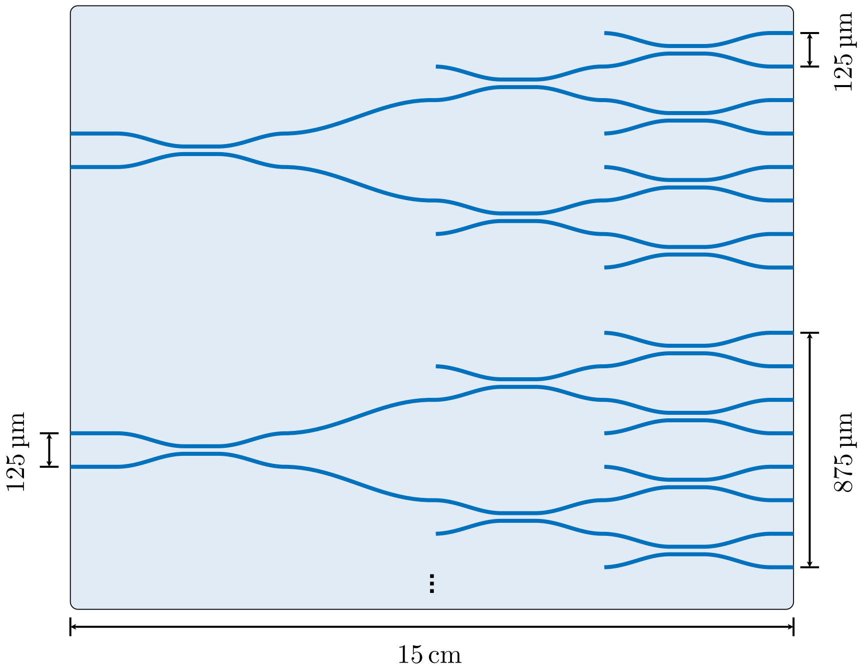

Figure 3.9.: Repetitions of 2x8 structure. The beam splitter cascade structure is repeated with slightly varying parallel coupler lengths to ensure a structure with ideal coupling and without defect is produced.

3.2.3. Results – Power Distribution and Coupling Ratios

We will now discuss the performance for the fourth chip iteration (mk.4). In this version 12 structures of the 2x8 beam splitter cascade were created overall, with only minute differences in coupler lengths. The details of individual coupler ratios and output distributions for all 12 structures are shown in the appendix section A. For the BHC measurements we chose to use structure 5-1, with the 5 indicating the fifth coupling length written (3.95 mm), and the 1 signifying the first of two duplicates. In this section we will show the output mode picture, the power distribution the structure produced, as well as an estimation of the individual coupling ratios in the chip.

Fig. 3.10 shows the output modes of structure 5-1, magnified and focused onto a camera with an objective lens. Eight equidistant modes are apparent with similar mode shapes and of similar output powers.

The original mode size in the chip can be estimated the following way. The total magnification can be found from the ratio of the mode pitch in the image to the waveguide pitch in the waveguide. From the mode size in the image we can then calculate the original mode size in the waveguide. The beam waist radii leaving the waveguide were

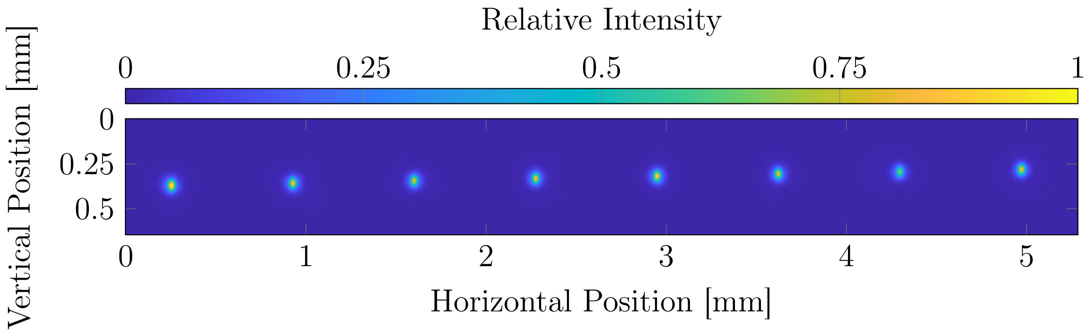

Figure 3.10.: Output modes of waveguide structure 5-1, focused and magnified onto the camera. Positions refer to position on camera sensor.

determined to be ca. $w_{0,x} = 9.6\,\mu\text{m}$ and $w_{0,y} = 10.7\,\mu\text{m}$ (half width at $1/e^2$ intensity). A close-up of the guided modes is shown in Fig. A.1 in the appendix.

In Fig. 3.11 we see the output power distribution of structure 5-1, as determined from integration over the individual modes in the camera picture Fig. 3.10. The red line indicates the optimal $1/8 = 12.5\,\%$ splitting. The maximum relative power is 14.94 % and the minimum is 10.25 %, giving a maximum absolute deviation from the 12.5 % optimum of 2.44 %. As we have discussed in section 2.6.2 we will be able to account for the deviations in the post processing.

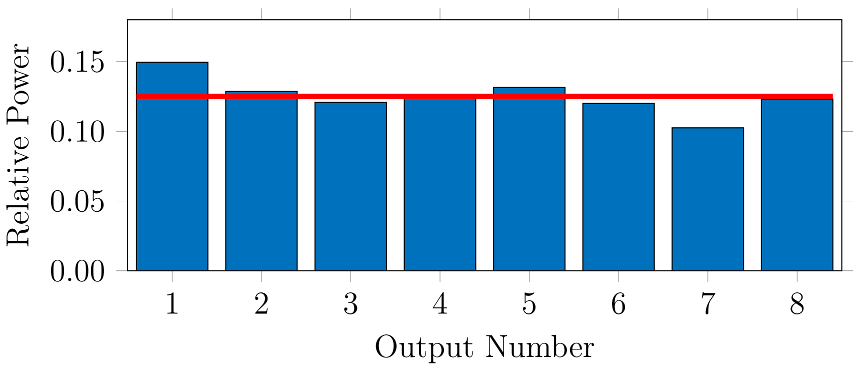

Figure 3.11.: Output distribution of structure 5-1. The red line shows 12.5 % reference of optimal splitting.

Fig. 3.12 shows the individual coupling ratios implemented in structure 5-1. The reflection coefficients are shown, which we define as the relative power remaining in the original waveguide. The coupler naming convention is shown in Fig. 3.13. Overall a flat distribution is found with all couplers close to the 50 % target as indicated by the red line. The maximum value is 52.7 % and the minimum value is 45.4 %, the maximal

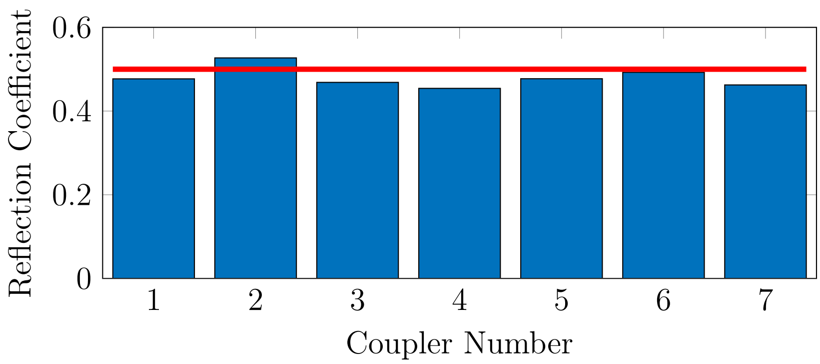

Figure 3.12.: Estimate of individual coupling ratios for structure 5-1. The red line shows the 50 % reference. Reflection is defined as remaining in the same waveguide.

deviation is hence 4.6 %. The couplers have a tendency to overcouple, so that less than 50 % of power remains in the original waveguide.

The coupling coefficients are calculated from the power output distribution in Fig. 3.11 as

$$R_1 = \frac{\sum_{i=5}^{8} P_i}{\sum_{i=1}^{8} P_i} \quad (3.6)$$

$$R_2 = \frac{\sum_{i=5}^{6} P_i}{\sum_{i=5}^{8} P_i} \quad (3.7)$$

$$R_3 = \frac{\sum_{i=3}^{4} P_i}{\sum_{i=1}^{4} P_i} \quad (3.8)$$

$$R_4 = \frac{P_7}{P_7 + P_8} \quad (3.9)$$

$$R_5 = \frac{P_6}{P_5 + P_6} \quad (3.10)$$

$$R_6 = \frac{P_3}{P_3 + P_4} \quad (3.11)$$

$$R_7 = \frac{P_2}{P_1 + P_2}. \quad (3.12)$$

This approach assumes, that no asymmetrical losses exist in the paths from the coupler to the output and therefore can only offer an estimate of the real coupling coefficients.

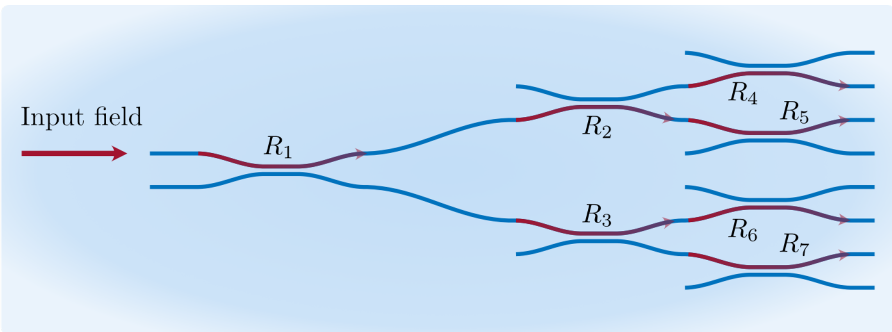

Figure 3.13.: Naming convention of couplers. Reflection is defined as power remaining in the original waveguide.

The total transmission T_{total} through structure 5-1, i.e. the ratio of summed output power over all outputs, to the input power, was measured to be $T_{\text{total}} \approx 31\,\%$.

3.3. Photodiode-Array Detector

We will now discuss the detection of the eight output modes of the waveguides using an integrated photodiode array. To that end a mount allowing precise positioning of the diode array had to be constructed and transimpedance amplifiers for all eight photodiodes had to be produced and tested. We will first give an overview of the electrical design, then show the mechanical design, and finally discuss the performance of the detector.

3.3.1. Electrical Design

The centerpiece of the detector is the photodiode array. We use the Fermionics FD80A-10 array with 10 diodes in a row, of which we only use the inner 8. The FD80 photodiodes in the array offer high speed performance with low capacitance and a low dark current, with a photosensitive area of 80 µm in diameter per diode. The device, shown in Fig. 3.14a, is designed around a ceramic base $11\,\mathrm{mm} \times 2.5\,\mathrm{mm} \times 1\,\mathrm{mm}$ in size. A gold wrapper implements the contact for the common cathode. The row of diodes with a pitch of 250 µm is found in the central black region and features an anti-reflective coating. The individual anodes of the photodiodes are connected by gold wire bonds to a vapour deposited gold fanout structure, allowing individual contacting.

In our case, the photodiode ceramic will be held by a carrier PCB (printed circuit board), see the schematic in Fig. 3.14b. The carrier board is designed as a circular shape with a diameter of 25 mm, so it can conveniently be placed in an optics mount. The electrical connection of the diode array to the carrier board, however, posed a technical challenge. Here the fine contacts on the ceramic at a pitch of 500 µm, and even less width, have to be connected to the fine solder pads on the carrier PCB, without electrical contact between neighbouring anodes.

Since the workgroup has experience in SMD soldering, the first idea was to directly solder the contacts by hand. In a first attempt we used 60Sn/40Pb solder, which dissolved the deposited gold contacts on the ceramic. Using indium solder this problem was overcome, but no sufficient control over the solder was reached to create the fine connections.

The second idea was to use an electrically conductive adhesive. This approach was tested in cooperation with Dr. Andrej Novikov from the university's Institute of Electronic Appliances and Circuits in Rostock. A template with cutouts for the finer and larger solder pads surrounding the diode array on the carrier PCB was produced by laser cutting.

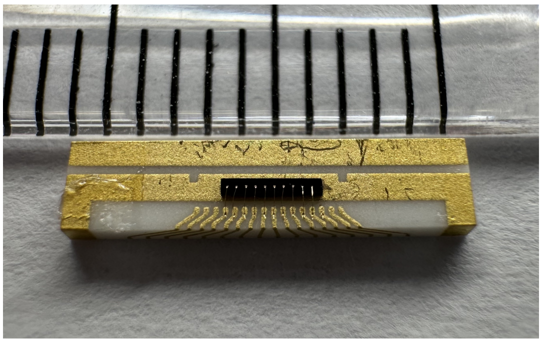

(a) Integrated Photodiode Array

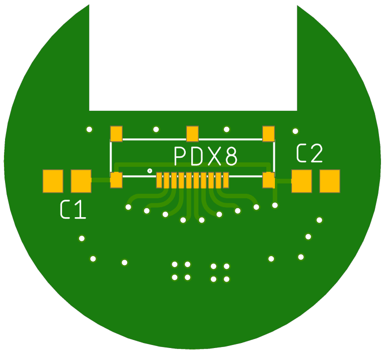

(b) Carrier PCB

Figure 3.14.: **(a)** FD80A-10 photodiode array by Fermionics, millimetre rule for scale. 10 photodiodes in a line are situated in the central black bar with 250 µm pitch (the outer two photodiodes are not used here). The individual diode anodes are connected by gold wires to the fanned out structure in the front for contacting. The ceramic is wrapped with the common cathode.
(b) Schematic of the carrier PCB. The diameter is ca. 25 mm, designed for placement in an optics mount. The diode array ceramic is placed in the center. 5 square gold pads surround the ceramic for mechanical connection and common cathode contacting. The photodiode anodes are to be connected to the row of smaller solder pads beneath the central box. On the backside a socket for a ribbon cable plug is placed.

The electrically conductive adhesive, here the MG Chemicals 9400 1-part epoxy, was then to be printed manually with a doctor blade through the cutouts onto the carrier PCB. The diode ceramic could then be placed into its designated place, with the adhesive both providing electrical contact to the individual pads and also mechanical fixation.

Over many attempts, however, either no sufficient contact between the adhesive and the array's gold contacts was reached, or short circuits between neighbouring contacts arose. While the larger gold pads on the carrier PCB could be connected to the common cathode, and sufficient mechanical stability was reached, no satisfying result was reached for the finer contacts.

The third idea was then to use gold wire bonding. While the adhesive was to be used for the mechanical connection and the common cathode electrical connection, gold wire bonding was to be used for the finer connections of the individual photodiode anodes. We used the semi-automatic wire bonder TPT HB16 kindly provided by the Institute of Electronic Appliances and Circuits. Ball-wedge bonding was used with gold wire of 25 µm in diameter. The ball-connection was placed on the top part of the fanout structure on the ceramic, and the wedge-connection was placed on the gold pads of the carrier PCB.

After considerable tests on the TPT H68 bond sample and with defect photodiode arrays over various days, at last the gold wire connections could be placed successfully on a functional sample of the array and the carrier PCB. While two of the in total ten created bonds on this sample broke, it was coincidentally the outer two that broke, so the center eight diodes could be used as planned. Fig. 3.15 shows the final result of the bonding process.

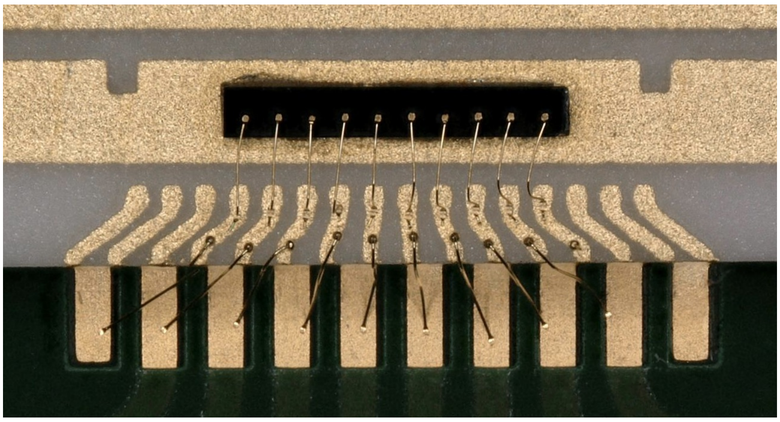

Figure 3.15.: Successful final result of the bonding process, recorded at 50x magnification. Ball-wedge bonds were created from the top of the fanout structure on the array ceramic to the solder pads on the carrier PCB. While the outer two bonds broke, the inner eight diodes could be used as planned.

We will now turn to the further elements of the electrical design. Fig. 3.16 shows an overview of the electronic set-up. The electric signals from the diode array are sent via the carrier PCB and a short ribbon cable to the motherboard. Here all signals are routed and voltage regulators provide power to the amplifier cards where every diode signal is amplified individually.

The amplifier cards implement an ultra low noise, high speed and high dynamic range transimpedance amplifier circuit, carefully designed within the workgroup and similarly used in the BHD stage. Here we use the low noise and high speed operational amplifier AD829 (for specification see [Ana11]). The output of the operational amplifier is sent to a low- and a high-pass stage to create a DC and an AC output, respectively.

The DC output is useful for reading out the mean power incident upon the photodiode and will later be used to infer the phase between the LO and the signal beam from their interference. The AC output allows measurement of the incident field's intensity fluctuations, without the constant offset generated by the mean power, allowing greater dynamic range.

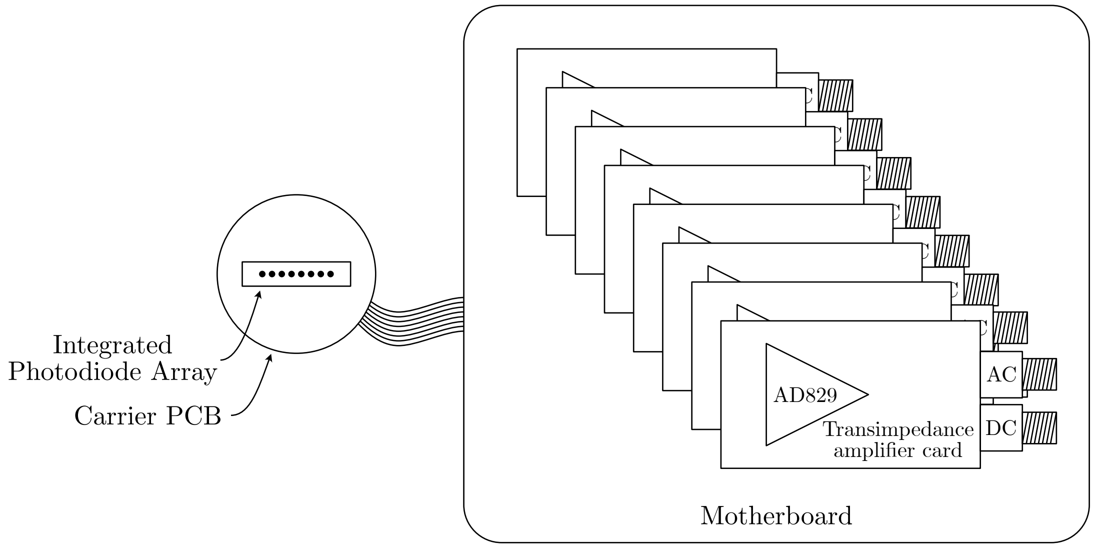

Figure 3.16.: Schematic overview of the electronic set-up. The photodiode array is placed on a small carrier PCB. The individual diode signals are sent to individual transimpedance amplifier cards. A motherboard provides signal routing and power supplies to the amplifier cards. Output signals are split into a low-pass filtered output (DC) and a high-pass filtered output (AC).

3.3.2. Mechanical Design

For the mechanical design the goal was to allow precise 3D positioning of the diode array and 1D rotation to allow matching of the roll of the line of output modes to the line of photodiodes. Fig. 3.17 shows a render of the mechanical layout. The carrier PCB with the diode array is placed in the Thorlabs CRM1P/M precision rotating optics mount that allows rotation via a micrometer drive. The optics mount is mechanically connected to a Thorlabs MAX350D/M fibre launch stage, enabling 3D positioning via further micrometer drives with 4 mm of range available in each dimension. The motherboard with the amplifier cards are housed separately in an upright case closely behind the rotating mount. The AC and DC outputs from the amplifier cards are accessible via SMA connectors at the backside of the case.

3.3.3. Performance

We will now test the photodiode circuits for various required properties, including comparable transfer functions, linear DC and AC behaviour, similar quantum efficiencies, and dark noise clearance.

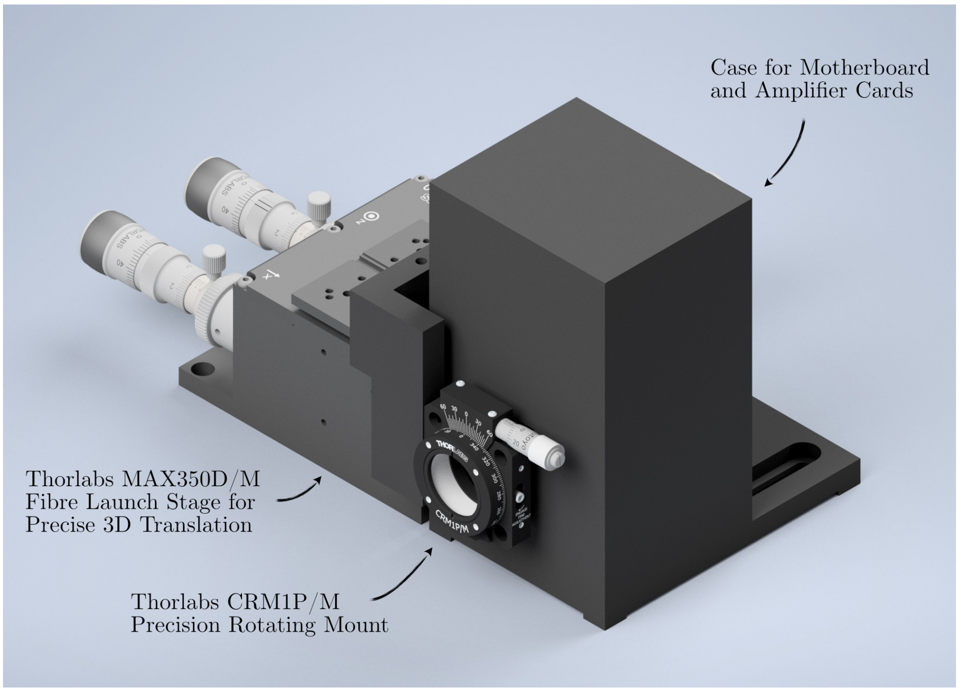

Figure 3.17.: Render of the mechanical detector design. The carrier PCB containing the photodiode array is placed in a Thorlabs CRM1P/M precision rotating optics mount, allowing rotational alignment of the photodiode line to the line of output modes from the waveguide chip. The rotating mount is connected to a Thorlabs MAX350D/M fibre launch stage, thereby enabling 3D translational adjustment of the photodiode array. Behind the rotating mount the motherboard and the amplifier cards are housed in a separate case. The electrical signals from the diode array are sent from the carrier PCB to the motherboard via a short ribbon cable.

Transfer Functions

The first test we discuss is the measurement of transfer functions. The photodiode circuits should have near-identical transferfunctions in the frequency window of interest. To measure the transferfunctions we focus amplitude modulated light onto a reference photodiode (the same is used for all amplifiers), which is connected to one amplifier card at a time. Using a network analyser we vary the modulation frequency from 10 kHz to 200 MHz and measure the amplifier's AC output in magnitude and phase. The results are shown in Fig. 3.18.

The recorded transfer functions show the high pass behaviour of the AC stage with a cutoff frequency of $f_{\mathrm{HP}} \approx 160\,\mathrm{kHz}$. Overall a flat magnitude response is found from ca. 400 kHz to 10 MHz for all amplifier cards. After 50 MHz the bandwidth limitations of the operational amplifiers become visible.

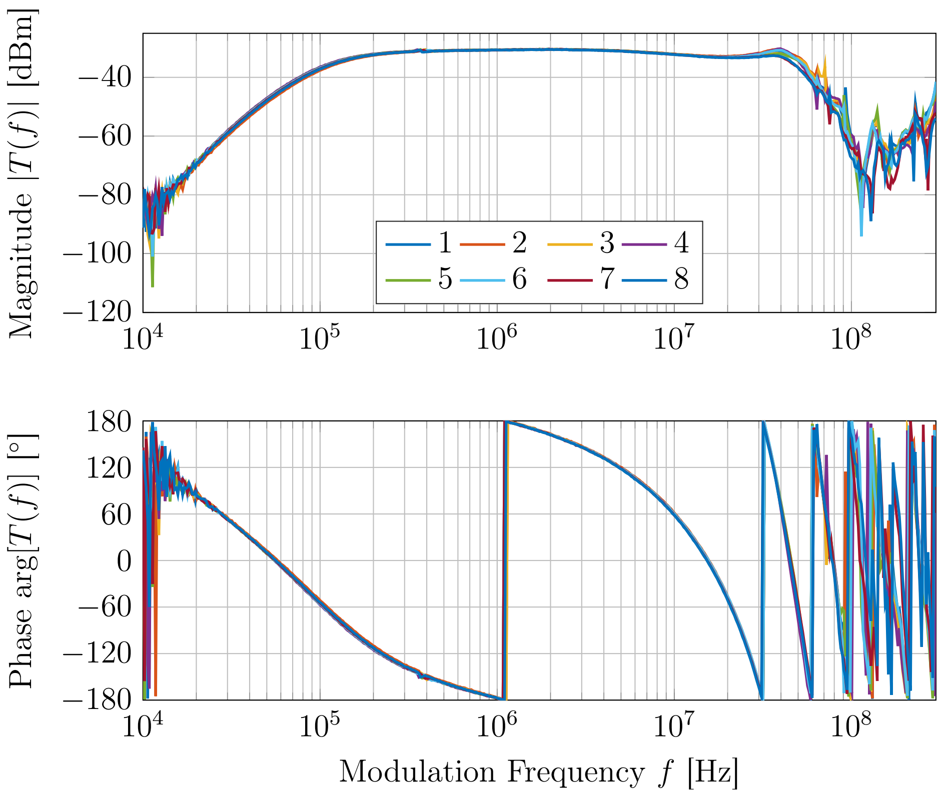

Figure 3.18.: Transfer functions of all eight amplifier cards for amplitude modulated input light, recorded with the same reference photodiode for each card individually. From ca. 30 kHz to 20 MHz all transfer functions are similar in magnitude and phase. A flat magnitude response is found from ca. 200 kHz to 10 MHz for all amplifier cards.

Most important to the experiments in this thesis is the response in the target frequency window. For the quantum noise limited measurements other forms of noise, e.g. relaxation oscillations of the laser at ca. 1 MHz or the phase modulations generated at 12 MHz and 35 MHz, need to be avoided. In the data analysis later, we will focus on the frequency window from 6 MHz to 8 MHz. Within this interval the transfer functions of all circuits are nearly identical, with a maximum magnitude difference of ca. 0.3 dBm and a maximum phase difference of ca. 3.2° between any two curves.

DC Linearity and Quantum Efficiency

We will now test the diode-circuits for linearity between the input optical power and the voltage output of the low-pass filtered DC stage. Working with the detector is generally simplified by a linear voltage response, e.g. in the retrieval of the phase between LO and signal beam a linear map between detector voltage and field power requires less post processing and is overall more intuitive. The quantum efficiency can be estimated from the slope given by output voltage and incident power. Near-identical quantum efficiencies are desired to decrease corrections in the post-processing, although they are not strictly necessary.

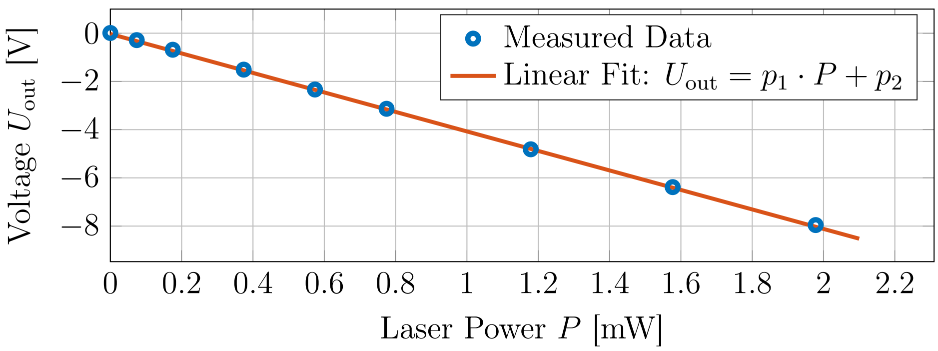

Figure 3.19.: Test of linearity of optical input power to output voltage, shown exemplarily for diode and amplifier 1. The linear fit agrees well with the measured data, with a negative slope of $p_1 = -4.04\,\mathrm{V/mW}$. The quantum efficiency is estimated to be $\eta = 92.4\,\%$.

Fig. 3.19 shows an example for the DC linearity test, here for the photodiode and amplifier card number 1. The laser power P (measured with an optical power meter) and corresponding voltage response U_{out} are shown, and a linear fit $U_{\mathrm{out}} = p_1 \cdot P + p_2$ between them is performed with the linear coefficients p_1 and p_2. We find a slope of $p_1 = -4.04\,\mathrm{V/mW}$, where the negative sign is due to the inversion in the transimpedance amplification. Highly similar behaviours are found in the other diodes and amplifiers; the average slope over all eight is found to be $\bar{p_1} = -4.03\,\mathrm{V/mW}$. The circuits show low variation, with the steepest slope at $p_{1,\max} = -4.06\,\mathrm{V/mW}$ and the shallowest slope at $p_{1,\min} = -3.95\,\mathrm{V/mW}$.

From the voltage to power response measurements we can now infer the quantum efficiencies of the diodes. Electrically, the photo current I is given by the output voltage U_{out} over the transimpedance resistance R_{TI}. Optically, the photo current is produced by the photon flux $\phi = n/\Delta t = P/(hf)$ where n is the number of photons arriving in the time span Δt, P is the optical power and hf is the photon energy. The chance to produce a photo electron in the semiconductor diode is given by the quantum efficiency η. The photo current is now found as $I = \eta e P/(hf)$ with the electron charge e. From the equality the quantum efficiency is found as

$$\frac{U}{R_{\text{TI}}} = I = \eta e \frac{P}{hf} \tag{3.13}$$

$$\Leftrightarrow \eta = \frac{Uhc}{PR_{\text{TI}}e\lambda} = \frac{p_1 hc}{R_{\text{TI}}}, \tag{3.14}$$

where in the second line we have used the slope $p_1 = U/P$.

For the example of diode and amplifier number 1 the quantum efficiency is found to be $\eta = 92.4\,\%$. For the other diodes very similar values are found, with a mean of $\bar{\eta} = 92\,\%$, a minimum value of $\eta_{\min} = 90.3\,\%$ and a maximum of $\eta_{\max} = 92.8\,\%$.

AC Linearity and Dark Noise Clearance

The theory we presented in chapter 2 is based on measurements of the photon flux at different detectors $\hat{n}_j = \hat{a}_j^\dagger \hat{a}_j$ and their correlations. For a correspondence to exist between theory and experiment then, the measured photo currents, or voltages, need to be a linear representation of the photon flux. While we have shown this to be the case for the low-pass filtered output, we will now test the linearity in the AC stage by measurements of the noise power for varied laser power.

For a single field incident on the detector, the photon flux becomes

$$\hat{n} = \hat{a}^\dagger \hat{a} = (\alpha^* + \delta\hat{a}^\dagger)(\alpha + \delta\hat{a}) \tag{3.15}$$

$$= |\alpha|^2 + |\alpha|\delta\hat{\chi} + \delta\hat{a}^\dagger\delta\hat{a}, \tag{3.16}$$

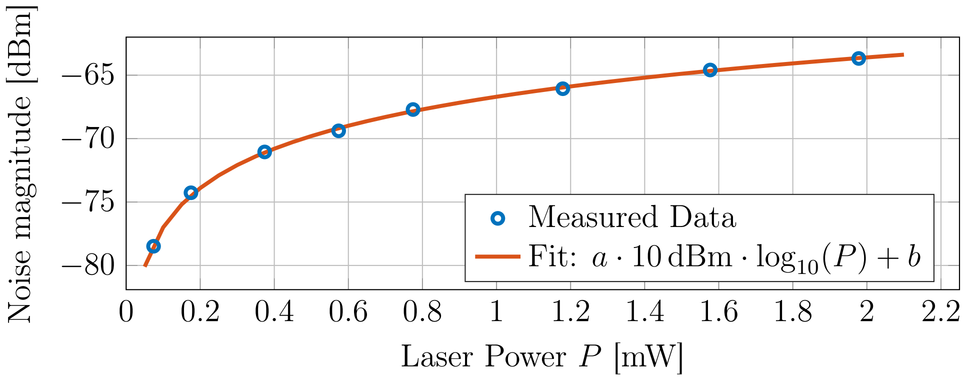

Figure 3.20.: Investigation of scaling of noise power with laser power, shown for diode and amplifier 1. The detector dark noise was subtracted and the noise magnitude was averaged over the frequency window from 6 MHz to 10 MHz. For a coherent state, as approximately realised by the laser, we expect the noise power to scale linearly with laser power. The scaling exponent in P^a was found by performing a logarithmic fit. For this circuit $a = 1.03$ was found, signifying nearly optimal linear behaviour.

where $\delta\hat{\chi}$ describes the fluctuations of the quadrature in phase with the coherent amplitude. As we are concerned only with the fluctuations we can neglect the static offset term, and further assuming a strong enough coherent amplitude, we can also disregard the second order fluctuation term, leaving only

$$\hat{n}_{\mathrm{AC}} = |\alpha|\delta\hat{\chi}. \tag{3.17}$$

If the voltage output from the detector is linear in the photon number, $\hat{U}_{\mathrm{AC}} = \zeta\,\hat{n}_{\mathrm{AC}}$, with a proportionality constant ζ containing e.g. quantum efficiency and all other detector constants, the variance becomes

$$\begin{aligned} \operatorname{Var}\hat{U}_{\mathrm{AC}} &= \zeta^2\,|\alpha|^2 \operatorname{Var}\delta\hat{\chi} && (3.18)\\ &= P\cdot\zeta^2 \operatorname{Var}\delta\hat{\chi} && (3.19)\end{aligned}$$

and depends linearly on the mean optical power $P = |\alpha|^2$. In contrast, for classical intensity fluctuations, or for an amplitude modulated laser, the variance will scale with the square of the laser power [BR19]. On a logarithmic scale, as is typically used, a doubling in optical power is then expected to yield a 3 dB increase in noise power when only quantum fluctuations are present, while for dominant classical noise or modulations a 6 dB increase will be seen.

Fig. 3.20 exemplarily shows the result of measurements performed on diode and amplifier card 1, with highly similar results found for all other diodes and amplifiers. Here the laser power was varied from 0 mW to ca. 2 mW and a power spectrum of the AC output was recorded for every power setting. The dark noise from the detector was subtracted from every spectrum and the average noise magnitude in the frequency window from 6 MHz to 10 MHz was calculated.

To investigate the scaling of the noise magnitude with laser power, we consider Eq. (3.19) on a logarithmic scale under assumption of a general power scaling as P^a,

$$\log_{10} \mathrm{Var}\, \hat{U}_{\mathrm{AC}} = \log_{10}(P^a \cdot \zeta^2 \, \mathrm{Var}\, \delta\hat{\chi}) \tag{3.20}$$

$$= a \cdot \log_{10}(P) + b, \tag{3.21}$$

where logarithm rules yield the scaling exponent a as a prefactor and all other constants contained in b. Fitting the measured data accordingly for the coefficients a and b immediately reveals the scaling.

For diode and amplifier card 1 a scaling factor of $a = 1.03$ was found. Over all circuits the average value is $\bar{a} = 1.01$ with a minimum value of $a_{\mathrm{min}} = 0.98$ and a maximum value of $a_{\mathrm{max}} = 1.04$. We can therefore assume the AC outputs to show sufficiently linear scaling of input fluctuations so they can be used for the correlation measurements without post-processing.

Dark Noise Clearance

Dark noise clearance refers to the distance in spectral power between the signals to be measured and the detector's intrinsic (dark) noise. A clearance of typically 10 dB or more is desirable. To assess dark noise clearance we use measurements performed with the LO at typical power as only light source impinging on the detector, and with both LO and signal beam blocked (dark). From the power spectra of the AC signals the dark noise clearance can be read out. Fig. 3.21 exemplarily shows the power spectral densities for the AC signals recorded by channel eight. Here a 6 MHz to 8 MHz band pass filter has already been applied in the post-processing. We see ca. 10.1 dB of dark noise clearance, with the other channel's clearances ranging from 8.2 dB to 9.8 dB.

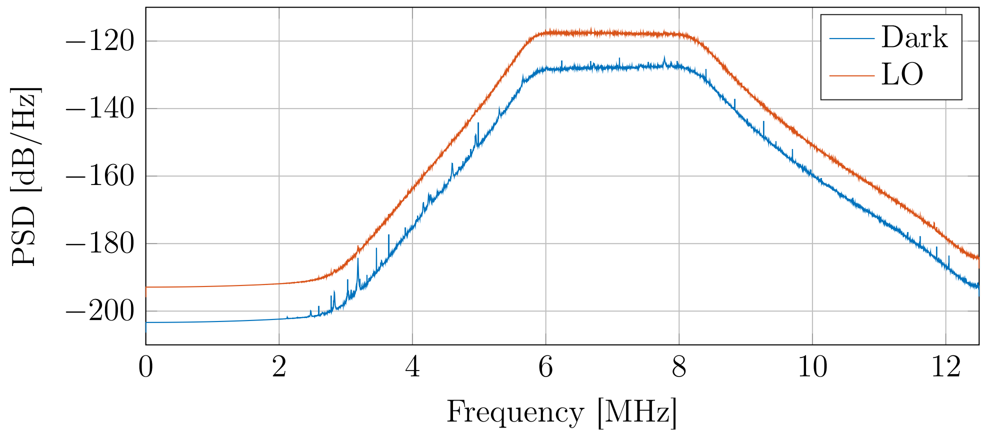

Figure 3.21.: Power spectral density (PSD) for detector dark noise and LO shot noise for channel 8 for bandpass filtered data.

3.4. Multibeam Coupling

A central technical problem that needed to be solved was the multibeam coupling of modes into the waveguide chip, and from the waveguide chip onto the detector.

On the input side the LO and the signal beam have to be coupled into the waveguide chip. Here the waveguide pitch of 125 µm has to be met and the eigenmode size of the waveguides should be matched to minimise losses. Further the same polarisation has to be maintained between both beams.

On the output side all eight output modes from the waveguide chip have to be imaged onto the 1x8 photodiode array. Here the pitch has to be transformed from 125 µm to 250 µm while maintaining the geometry of the mode distribution in 2D space. Further, the transformed mode sizes must fit onto the 80 µm diameter of the diodes. Again, only low losses should occur ideally.

Many different solutions are possible to reach these goals. One possibility we discussed is the use of fibre arrays, which are often used for multi-beam coupling into and out of waveguides as e.g. in the cooperation workgroup Experimental Solid-State Optics in Rostock. Fibre arrays typically have free fibres on one end, and an small connecting structure on the other end, in which the fibres are brought together by a comb-like structure, at a pitch of e.g. 127 µm, 250 µm or a configured-to-order distance.

Both input and output coupling could be realised this way. In the case of input coupling the LO and signal beam would need to be coupled into the fibres first and the array structure would need to be precisely positioned in front of the waveguide chip to match the waveguide positions. In the output coupling the waveguide modes would be directly coupled into the fibres via the array, and the fibres would need to be coupled to the diodes individually. In this case fibre coupled photodiodes could be used instead of the photodiode array.

A clear disadvantage of fibre arrays is the mode matching, or usually the lack thereof. Typically coupling is achieved by bringing the end of the fibre within the array close to the waveguide for direct coupling ("butt coupling"). In this case neither matching of the mode field sizes nor of the wave front curvatures is achieved, making this coupling technique inherently lossy.[2] Further there was no experience in our workgroup with fibre arrays, while we have extensive experience with free space- / bulk optics mode matching. Therefore the adjustment effort for using fibre arrays was assumed to be, at least initially, on par with free space solutions. We decided to first investigate a free space solution, before potentially exploring a fibre based solution.

3.4.1. Free Space Collimating Confocal Lens Set-Up

We will now discuss the multibeam coupling of LO and signal beam into the waveguide chip, and the imaging of the eight output modes from the chip onto the photodiode array. Two goals were sought – first, we want beams which run in parallel to each other to remain parallel after the imaging, and second, we want to use collimated beams in the imaging.

In the input coupling the resulting beams need to be parallel to each other to match the waveguide modes which run in parallel in the chip. While the signal and LO beams do not strictly need to be parallel before the imaging, the adjustment is simplified by it.

In the coupling from the waveguide chip onto the photodiode array the beams from the waveguide run in parallel. While the transformed beams after the imaging, again, don't strictly need to be parallel, we still see the following advantage in it. If the beams run in parallel, the longitudinal positioning of the detector can be used to find the focus of the beams while the spacing of the modes remains constant. If, however, both the mode size *and* the mode spacing changes at the same time due to non-parallel beams, the adjustment becomes significantly more complicated.

[2] Fibre arrays with micro lenses can mitigate the mismatch, but were not part of the discussion at the beginning of this work.

The second goal was to use a collimating set-up if possible. If only one lens or objective is used, the position of the lens will decide both the position of the focus as well as the magnification, which again is inconvenient for the adjustments. We consider a collimating set-up to be easier to adjust, as collimation from the first lens is typically easy to test, the magnification ratio is (nearly) fixed by the focal lengths of the lenses, and the position of the second lens (approximately) only decides the position of the created image.

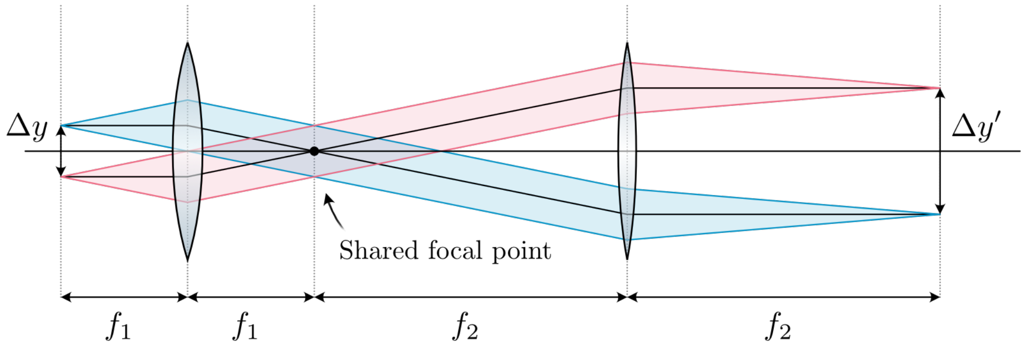

Figure 3.22.: Top view of the collimating, confocal lens set-up. Due to the shared focal point, the initially parallel center rays of both beams remain parallel in the output.

A solution fulfilling both goals was found in the collimating, confocal lens set-up as illustrated in Fig. 3.22. With the first beam positioned in focal distance f_1 from the initial beam waist, a collimated beam is created in the intermediate space. The second lens with focal length f_2 is positioned so that the inner focal points are identical and creates a magnified image after its focal length to the right. We follow two beams with initially parallel center rays (shown in black). Since the central focal point is shared, the intermediate center rays are focal rays to both lenses, and consequently are parallel again after the second lens, proving the conservation of parallelism. Further the magnification of both the beam distance and their waist radii is found via the tangents of the intermediate rays as $A = \Delta y'/\Delta y = f_2/f_1$.

3.4.2. Implementation of Input Coupling

For the input coupling the target mode size and pitch are given by the waveguide chip. The waist radius within the waveguide was determined to be approximately $w \approx 10\,\mu\text{m}$. Here the minor ellipticity of the waveguide modes is not accounted for. Further the mode pitch is $125\,\mu\text{m}$. The goal for the imaging is to start from bigger modes at a larger separation so the LO and the signal beam can be placed in parallel.

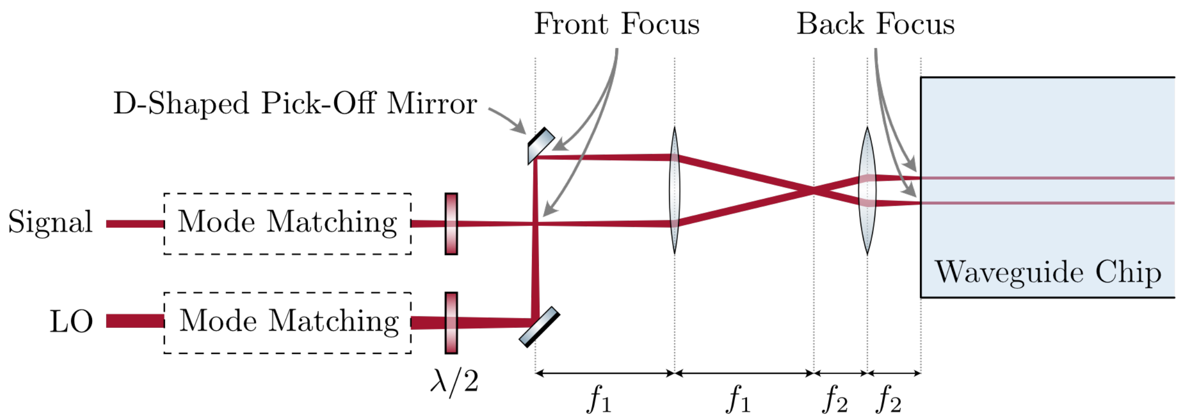

Figure 3.23.: Top view of the input coupling set-up with an indication of the mode size evolution. A 10:1 collimating, confocal telescope is used, scaling down the mode sizes and mode separation to the waveguide target parameters. The LO and signal beams are mode matched individually to the front focus mode and parallelised by a d-shaped pick-off mirror. The individual polarisations can be set via $\lambda/2$ plates.

Fig. 3.23 shows a scheme of the input coupling with an indication of the mode size evolution. Here a 10:1 collimating, confocal telescope is used as described above, using a $f_1 = 200\,\text{mm}$ spherical lens and a $f_2 = 20\,\text{mm}$ aspherical lens. To reach modes with $w \approx 10\,\mu\text{m}$ at $125\,\mu\text{m}$ separation in the back focus, the input modes at the front focus need to be $w = 100\,\mu\text{m}$ in radius at a separation of $1250\,\mu\text{m}$.

To achieve beams running in parallel at a close distance a d-shaped pick-off mirror is used in the front focus of the LO. The initially separated LO and signal beam are mode matched individually to the front focus mode via additional lenses. Further a $\lambda/2$ plate is used in both beams to set the polarisations.

3.4.3. Implementation of Output Coupling

In the output coupling the goal is to transform the mode separation from the waveguide pitch of $125\,\mu\text{m}$ to the photodiode array pitch of $250\,\mu\text{m}$. Fig. 3.24 shows a top view of the coupling scheme. A 1:2 collimating, confocal telescope is used, employing $f_1 = 50\,\text{mm}$ and $f_2 = 100\,\text{mm}$ spherical lenses. The front focus is located at the waveguide facet with mode radii of $w \approx 10\,\mu\text{m}$ and a mode separation of $125\,\mu\text{m}$. The back focus features modes with a radius of $w \approx 20\,\mu\text{m}$ at a separation of $250\,\mu\text{m}$. The modes should be well fitting for the diodes' active diameters of $80\,\mu\text{m}$. While in practice larger mode sizes were created, the modes still fit on the diodes.

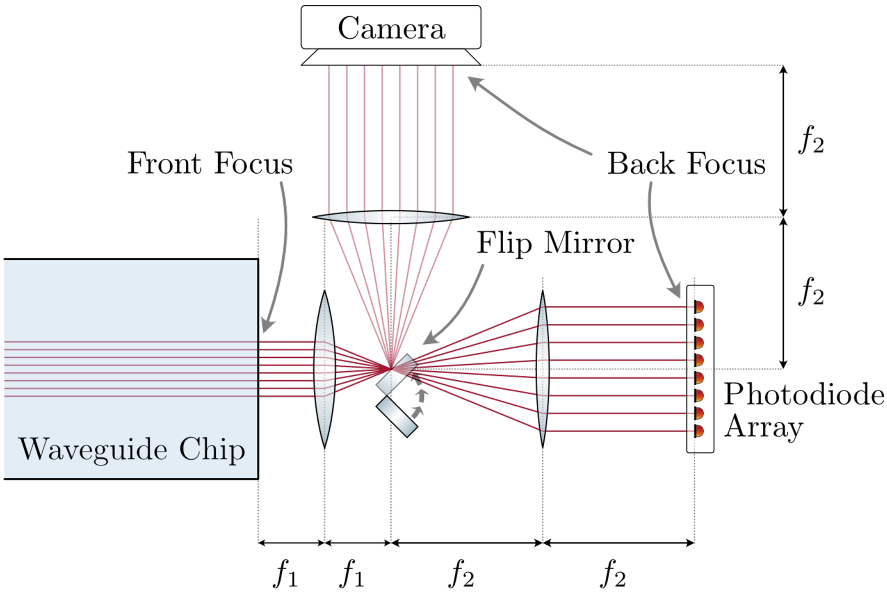

Figure 3.24.: Top view of the output coupling scheme. The eight output modes from the waveguide chip are enlarged in mode size and mode separation by a 1:2 collimating, confocal telescope and focused onto the photodiode array. Optionally a flip mirror can be placed in the intermediate space between the lenses to send the beams to a camera. In this path also the confocal set-up is used.

Further, a flip mirror can be placed in the intermediate space between the lenses, allowing the beams to be sent to a camera if needed. Here a WinCamD XHR beam profiler is used. The modes are focused onto the camera via a further 100 mm lens, following the confocal scheme, implementing approximately identical imaging as in the path to the photodiode detector. A LabVIEW program was developed for the camera analysis of the recorded mode picture in which, besides the camera image, further measurements are provided such as integrated intensity, pitch and mode size estimates, power distribution between the modes, etc.

The camera in the parallel path proved highly useful, e.g. in verifying the imaging in the output coupling or to check adjustments done in the input coupling. Further the camera was employed when a different waveguide structure was selected by transversally moving the chip. Due to the large sensor area in comparison to the photodiodes, the camera provided a quick and intuitive way to verify the adjustment in all cases, without needing further adjustment itself.

At last we want to point out another advantage that arose from the confocal lens scheme. In the earlier phases of this work stray light originating from the front facet of the chip (or the propagation within the chip) posed a problem. With earlier lens set-ups a focused spot with significant intensity was created in close longitudinal proximity to the imaged focus of the waveguide modes, impeding adjustments and measurements. With the confocal set-up, however, the intermediate real image of the stray light is found behind the shared central focal point. Therefore no real image is created after the second lens – instead the stray light is strongly defocused and no longer poses a problem.

3.5. Data Acquisition

We will now discuss the acquisition of measurement data for both the BHD and BHC measurements. In both cases fast fluctuations in the target frequency window of 6 MHz to 8 MHz need to be recorded, requiring according to the Nyquist criterion a sample rate of at least $f_{\text{Nyquist}} = 16\,\text{MHz}$ for alias free recording. The goal was to use National Instruments digitizer cards and LabVIEW, as the corresponding lab infrastructure already existed.

In the BHD measurements the signals from two photodiodes need to be recorded, necessitating two fast channels ($f_{\text{sample}} \geq f_{\text{Nyquist}}$) for the high-pass filtered (AC) signals, at least one slow channel recording the low-pass filtered (DC) output for retrieval of the phase between LO and signal beam from the interference signal, and one further slow channel for recording the voltage ramp applied to the phase-shifting piezo-mounted mirror.

For the BHC measurements eight photodiodes are used, and consequently eight fast channels are required. Further a slow channel is needed to record at least one diode's DC voltages for later phase retrieval as well as a slow channel to record the voltage ramp applied to the phase-shifting piezo-mounted mirror. The increased channel number for BHC complicated the data acquisition and necessitated the use of a FPGA (*field programmable gate array*) module rather than the simpler to use oscilloscope cards.

3.5.1. Implementation for Balanced Homodyne Detection

In the BHD measurements the two fast channels are realised using National Instruments' PXI-5152 oscilloscope card with two analog channels and a sample rate of 2 GS/s, 300 MHz bandwidth and 8 bit of resolution [Nat17]. For the slow channels the PXI-6132 multipurpose data acquisition module is used, featuring four analog channels with a sample rate of maximally 2.5 MS/s, 1.3 MHz bandwidth and 14 bit resolution [Nat04].

A LabVIEW VI (*virtual instrument*) created by a former group member, ensuring synchronous data acquisition from both cards, was used. The fast channels were sampled at 100 MS/s and the slow channels at 100 kS/s.

3.5.2. FPGA-Based Implementation for Balanced Homodyne Correlation

In the BHC measurements a NI-5751B digitizer adapter module is used for both the eight fast and the two slow channels. It features 16 analog channels with a 50 MS/s sample rate, 26 MHz bandwidth and 14 bit resolution [Nat15]. The digitizer is connected to a PXIe-7962R FPGA module with a Virtex-5 SX50T FPGA. Two banks of onboard DRAM (*dynamic random access memory*) are available with 256 MB per bank and a maximum data rate of 1.6 GB/s per bank. The connection to the host computer (lab PC) is realised by a PXI Express x4 connection with version 1.0 compliance, allowing a maximum theoretical transfer speed of 1 GB/s [Nat11]. The particular memory size and connection bandwidth will be important later in the analysis of data flow and its consequences for the read-out design.

While both fast and slow channels are sampled with the same digitizer, only the fast channels are sampled and stored at the full 50 MS/s rate, while for the slow channels only every 5000th value is stored, yielding an effective lower sample rate of 10 kS/s.

We will now turn to the software implementation in LabVIEW. The data recording VI(s) were developed using a *Getting Started* example from National Instruments as starting point.

Host-PC/FPGA-Target Division

For the measurements using the FPGA a two-sided hardware and software structure is needed. A host VI is run on the lab PC, while a FPGA VI is run on the *FPGA target*, i.e. the FPGA card to be used. An overview is shown in Fig. 3.25.

The host VI has the following tasks. First it launches the chosen FPGA VI on the FPGA target and sets the record parameters such as the host side buffer depth. Further it

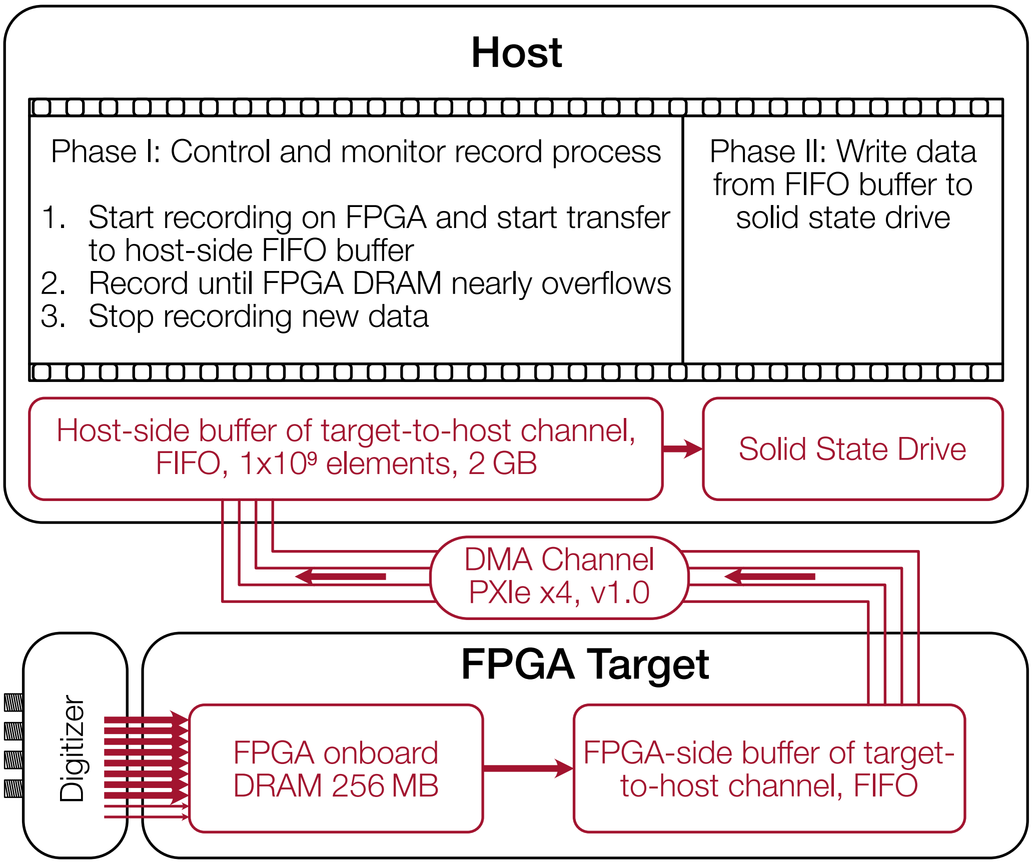

Figure 3.25.: Overview of the host/target separation in hardware and software, with an illustration of data flow (dark red). If recording is active, i.e. the "write to DRAM" flag has been set by the host, measurement data from the digitizer are passed on to the FPGA onboard DRAM for intermediate storage. When the FPGA-side FIFO buffer of the target-to-host channel is ready for new data (not full), data is shortly stored here, before being transferred via the DMA channel to the host-side FIFO buffer. New voltages are recorded until the measurement is stopped by the host. In the last step the recorded voltages are written from the host-side buffer to a file on the lab PC's solid state drive.

controls and monitors the data read and write process. A start and stop signal can be sent to the FPGA target to control whether data from the digitizer is recorded. The host VI receives the data from the FPGA target via a DMA (*direct memory access*) channel and stores it first in its host-side FIFO (*first in, first out*) buffer on the lab PC's RAM, before writing the data from the buffer to a hard drive.

FPGA VIs running on a FPGA target can be executed independently of a host PC once launched. The digitizer module continuously provides voltage samples, but only when the "write to DRAM" flag has been set by the host VI the measurement data are written to a FIFO memory on the onboard DRAM for intermediate storage. It is possible to execute immediate data manipulations on the FPGA if wanted. It was attempted to apply a frequency down-shift and a down-sampling on the data streams to reduce the needed bandwidth towards the lab PC and thereby enable continuous sampling. However not enough space was available on the FPGA to implement the operations for all eight fast channels.

Measurement data is written to the FPGA-side buffer of the target-to-host channel, whenever it is ready to accept new data. From the local buffer, data is sent to the host VI via the DMA channel [Nat24]. On the FPGA side the buffer is comparatively small, holding only 1023 16-bit integer values, implemented in block memory. Here the memory implemented on the DRAM acts as the main buffer. On the host side a relatively large buffer is set-up using the lab PCs RAM, holding up to 1 billion 16-bit integer values, effectively using 2 GB of storage.

Bandwidth Limitations

Due to bandwidth limitations no continuous sampling was possible. We will now describe the occurring data rates, identify the bottleneck in the transfer chain, and explain the solution which was used.

The digitizer samples the eight fast channels at the full 50 MS/s record rate. Since the voltage entries are stored as 16-bit integers a data rate of 800 MB/s is reached for bank 1 of the DRAM. Since the two slow channels are only sampled at 10 kS/s, a much lower data rate of 40 kB/s is reached for bank 2. We will neglect the data rate of the slow channels in our further analysis.

The maximum theoretical data rate of the onboard DRAM is 1600 MB/s per bank. If data is written into and out of the DRAM at full speed, this limit would be reached, in practice, however, the onboard transfer rate was not the limiting factor.

The target-to-host DMA channel uses the PXI Express x4 v1.0 connection, with a theoretical transfer rate of 1 GB/s. However, a much lower rate of ca. 678 MB/s was actually reached, possibly due to overhead in the communication. Since data cannot be moved fast enough from the FPGA DRAM through the DMA channel, data starts building up in the DRAM, slowly filling the 256 MB of storage.

The chosen solution here is recording in large chunks, rather than continuous. For BHC it is not necessary to record all data in one run, as long as the values for the AC channels are still synchronous to each other and the relative LO phase can be retrieved for each set of voltages.

The process used is the following:

1. Clear FPGA DRAM.
2. Start recording and start data stream from digitizer via FPGA DRAM and FPGA-side target-to-host buffer to the host-side buffer.
3. Write data until the FPGA DRAM nearly overflows (90 % full).
4. Stop recording, i.e. stop writing new data to the FPGA DRAM. DRAM empties into the host-side buffer.
5. Write data from host-side buffer to file on the lab PC's solid state drive.
6. Repeat from top if multiple acquisition runs are needed.

During the process the state of the FPGA DRAM is monitored to ensure no overflows have happened.

As a result typically 1891 blocks were recorded in one run, with each block containing 50000 rows of eight voltages for the fast channels. In the ca. 1.89 s of continuous recording ca. 1.475 GB of data were recorded. Typically only one run was performed per set of measurement parameters. If more statistic is wanted, however, multiple runs can be performed easily.

4. Measurements, Evaluation and Results

We have described in detail the set-up for our balanced homodyne correlation measurements (BHC). Now we will test the system with a well-known reference state to see if the expected behaviour is shown. We will use squeezed states which we have readily available in the lab.

The correlation functions of squeezed states depend on the squeezing strength, see Tab. 2.1, so in our first test we will produce squeezed states of different squeezing strengths by varying the pump power in the optical parametric amplifier (OPA), measure the correlation functions of the states with the BHC method, and compare the measured correlations with the theoretical expectation.

Correlation methods are expected to be more immune towards losses than other methods such as balanced homodyne detection (BHD). In the case of eight detectors we expect the measured field moments to scale with input losses as the square of the signal beam's intensity efficiency, η_{Si}^2. So in a second test we will introduce neutral density (ND) filters in the signal beam path and check if the measured correlations scale with the power transmission as T_{ND}^2.

At last, a key feature of correlation measurements is that all contributions from vacuum terms vanish. In a third test we will use coherent states of different displacements as signal states. In case of the AC filtering used, the measured correlation functions should be zero, independent of the coherent power.

For every measurement we will first give an explanation of the experimental method, and then discuss the results. Further we will use the first measurement, the measurement of correlations for different squeezing strengths, to explain the data evaluation process.

4.1. Correlation for Different Squeezing Strengths

In our first test we want to verify that the correlation moments measured for squeezed states scale correctly with the squeezing strength. We will therefore now produce squeezed states of different squeezing strengths by varying the pump power in the squeezer, measure the squeezing strength via BHD, measure the correlation moments via BHC and compare them with the theoretical expectation.

4.1.1. Method

We will first guide through the measurement process. For BHD a local oscillator (LO) of approx. 1 mW was used, while for BHC the LO power was ca. 6 mW before the front facet of the waveguide chip. The power of the OPA control beam was ca. 0.5 mW. The interferometric visibility in the BHD set-up was 90 %. Higher values were reached with the same set-up in the past, but due to time constraints no further investigation was possible. For the interference of LO and signal beam in the BHC waveguide a visibility of 97 % was found.

For every measurement step we set a pump power (here: 10 mW to 120 mW), measure the parametric amplification and deamplification, and then lock the pump phase to deamplification. The pump phase is thereby set anew for every measurement and slight variations of the squeezing angle occur between measurements.

With all parameters set BHD measurements are performed. The LO phase is continuously varied by driving a piezo-mounted mirror with a triangle oscillation at ca. 13 Hz with approx. 4π of phase range per incline and decline of the ramp. The steering signal is recorded as reference for the later phase retrieval.

We record the high-pass filtered (AC) outputs of both BHD photodiodes and the low-pass filtered (DC) signal of at least one of the diodes. The later one is used for the retrieval of the relative phase between signal beam and LO. Measurements are performed with LO and signal beam active, only LO active, and both inputs blocked (dark).

While typically the LO-only measurement, with blocked signal beam, is used as vacuum reference, here an issue was encountered. Measurements with coherent states as signal beam showed an unexpected dependence of quadrature variance on the LO phase. It is assumed that remaining phase modulations at 35 MHz in the signal beam caused nonlinear behaviour in the amplifier circuits. Due to time constraints no deeper investigation was possible, so as temporary solution we use coherent states as vacuum reference.

After the BHD measurements the flip mirror as shown in Fig. 3.1 is placed to send the signal beam to the BHC set-up for the correlation measurements. Here again the LO phase is continuously varied during the measurements and the steering voltage is recorded. Further, we record all eight AC outputs of the detector and one of the DC outputs for later phase retrieval. Measurements are performed with LO and signal beam active, only LO active, and both inputs blocked (dark). No nonlinear behaviour of the photodiodes was found for the BHC photodiodes.

The output intensity of the waveguide chip was observed to change as a triangle function in time with changing LO phase. This behaviour is plausibly explained by periodical changes to the pointing of the LO beam caused by the movement of the phase-shifter, resulting in periodical changes of the input-coupling efficiency. While the triangular behaviour was overcome by quick readjustments when needed, it is advisable to shorten the beam path from the phase-shifter to the waveguide for future measurements – perhaps by employing separate shifters for the BHD and BHC set-ups.

4.1.2. Data Processing (Filtering and Phase-Fitting)

The first step in the overall evaluation process is the basic processing of the raw AC and DC voltage arrays, for both BHD and BHC measurements. We will bandpass filter our data down to an appropriate frequency window and retrieve the LO phase for every entry.

As described in Sec. 3.3.3 we use the spectral window from 6 MHz to 8 MHz, which is free of disturbing technical signals. In a first step we apply corresponding high- and low-pass filters to the raw data. Next, the signals are resampled for more convenient file sizes, in the case of BHD from 100 MHz to 20 MHz and for BHC from 50 MHz to 25 MHz.

For the phase retrieval we will first identify time intervals with well-behaved, nearly linear LO phase evolution. Using the record of the piezo ramp steering signal, we can define windows between the inflection points of the triangular wave, leaving sufficient margins to both sides. We will only use these time intervals for further evaluation.

Within the chosen time windows, the DC output of the photodiode is expected to evolve as $U_{\mathrm{DC}} = a \sin\varphi_{\mathrm{LO}}(t) + U_0$. The time evolution of the LO phase can be well described by a fourth order Taylor series $\varphi_{\mathrm{LO}}(t) = \omega_4 t^4 + \omega_3 t^3 + \omega_2 t^2 + \omega_1 t + \phi_0$. Performing an according fit of the measured DC voltages gives the coefficients needed to interpolate the LO phase for every AC entry. This method of *continuous phase variation* was developed within the workgroup and published in Ref. [Agu+15].

4.1.3. Determination of Squeezing – BHD Evaluation

To characterise the squeezing strength, we will perform a standard BHD evaluation. We will then estimate the original squeezing strength present in the source, which is more relevant to us than the directly measured squeezing.

As the first step we calculate the difference signal of the two photodiode's AC signals to obtain a measure of the signal quadrature $\hat{\chi}$. We then sort all values into phase bins by their fitted LO phase, with a chosen bin width of 1°. We now have many realisations for the phase dependent quadrature $\hat{\chi}(\varphi_i)$ for each phase angle.

Then we calculate the variance over the entries in the respective phase bins, yielding a curve of quadrature variance over phase angle $\operatorname{Var}\hat{\chi}(\varphi_i)$.[1] The procedure is performed for both the squeezed state as signal beam, as well as the coherent state, which is used as vacuum reference (see above). An exemplary plot is shown in Fig. C.1 in the appendix.

Next, we identify phase spans of minimal signal quadrature variance (squeezing, V_{sq}) and maximal variance (anti-squeezing, V_{asq}) for the squeezed state, and the corresponding phase intervals in the coherent reference. We calculate both the mean value of variance for these regions as well as the random error of quadrature variance. We then calculate the squeezing and anti-squeezing (in linear units) from the quotients, as well as confidence intervals.

Recalling Eq. 2.63, the measured squeezing and anti-squeezing will relate to the original squeezing in the source as

$$V_{\mathrm{sq}} = \eta V_{\mathrm{src}} + 1 - \eta \tag{4.1}$$

$$V_{\mathrm{asq}} = \eta \frac{1}{V_{\mathrm{src}}} + 1 - \eta. \tag{4.2}$$

Hence the original squeezing in the source (and the detection efficiency η) can be found as

$$V_{\mathrm{src}} = -\frac{V_{\mathrm{sq}} - 1}{V_{\mathrm{asq}} - 1} \tag{4.3}$$

$$\eta = -\frac{(V_{\mathrm{sq}} - 1)(V_{\mathrm{asq}} - 1)}{V_{\mathrm{sq}} + V_{\mathrm{asq}} - 2}. \tag{4.4}$$

[1]While the bins have different numbers of entries, we calculate the variance over the same number of entries for each bin by capping at the minimum entry count found over all bins.

We calculate the estimate of the original squeezing as well as confidence intervals from error propagation, and finally transform from linear to logarithmic units (dB).

4.1.4. Transmission Balancing of Outputs for BHC

With the squeezing of the signal beam known, we now continue with the BHC evaluation. In the theory section 2.6.2 we discussed the realistic case of BHC with unbalanced transmissions after the initial beam splitter. We showed that if the individual transmissions are known, they can be cancelled out in the post-processing, see Eq. 2.94. We will now discuss a method to estimate the required internal transmissions in a waveguide structure, where a direct measurement is not possible.

The first attempt to determine the transmission ratio was to use the distribution of power in the output modes, similar to the estimate of splitting ratios in the manufacturing of the waveguide chip, see section 3.2.3. Ideally the DC output voltages of the diodes would be used for this, but due to the limited channels on the digitizer card this was not possible. Separate measurements of all DC voltages using an oscilloscope are possible but would introduce more complexity to the involved measurement process. It was attempted to use the camera picture for this, but the results were not reliable enough.

A viable alternative is to use the distribution of shot noise over the output modes, which can be measured with the AC channels. Since measurements with only the LO, i.e. without the signal beam, were performed anyway, this method creates no additional overhead during the measurements. According to Eq. 2.67, the variance in photo current of the j-th output will be

$$\mathrm{Var}\,\hat{n}_{j,+} \propto \tau_j^2 \rho_0^2 P_{\mathrm{LO}} \tag{4.5}$$

$$\mathrm{Var}\,\hat{n}_{j,-} \propto \tau_j^2 \tau_0^2 P_{\mathrm{LO}}, \tag{4.6}$$

where τ_j is the amplitude transmission coefficient from the first beam splitter to the j-th output as defined in section 2.6.2, ρ_0 and τ_0 is the amplitude reflectivity and transmission of the initial beamsplitter in the waveguide chip, and P_{LO} is the LO power. Part a) of Fig. 4.1 shows the variances of the AC voltages of the different channels before any balancing.

To determine the balancing factors τ_j independent of the splitting ratio of initial beam splitter, we will first cancel out the dependence on τ_0 and ρ_0 using estimates generated from Eq. 3.6. The initial beam splitter called R_1 in Fig. 3.13, will now be referred to as R_0

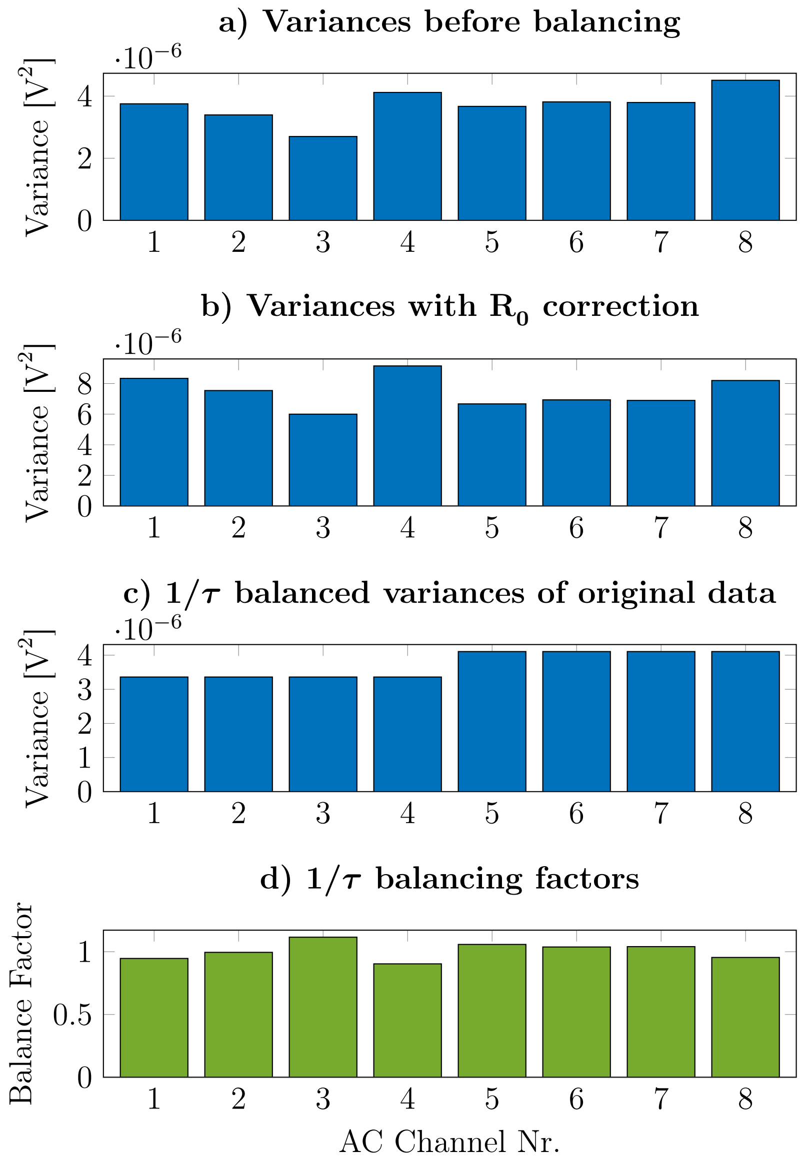

Figure 4.1.: Derivation of balancing factors for the uneven transmissions within the waveguide chip from measured shot noise when using the LO as only input. **a)** voltage variances of original data. **b)** Correction of voltages for asymmetric first beam splitter, using estimates for R_0 and T_0. Variances are proportional to the transmissions τ_j and can be used for the balancing factors. **c)** Variances of scaled (τ-balanced) voltages. **d)** Normalised balancing factors independent of LO power and detector constants.

to avoid conflicts between output indices and beam splitter indices. Scaling the voltages $U_1(t)$ to $U_4(t)$ by $1/\sqrt{R_0} = 1/\rho_0$, and $U_5(t)$ to $U_8(t)$ by $1/\sqrt{T_0} = 1/\sqrt{1-R_0} = 1/\tau_0$, yields the R_0 corrected variances

$$\mathrm{Var}\left(\frac{U_{j,+}}{\rho_0}\right) \propto \tau_j^2 P \tag{4.7}$$

$$\mathrm{Var}\left(\frac{U_{j,-}}{\tau_0}\right) \propto \tau_j^2 P \tag{4.8}$$

as seen in part b) of Fig. 4.1.

In case of the balancing test mode, where every channel needs to be balanced with $1/\tau_j$ to achieve even variances, we choose the balancing factors for the *upper modes* ($j = 1, ..., 4$) as

$$B_{j,+} = \frac{1}{\sqrt{\mathrm{Var}\left(\frac{U_{j,+}}{\rho_0}\right)}} \sqrt{\overline{\mathrm{Var}\left(\frac{U_{j,+}}{\rho_0}\right)}} \equiv \frac{\sqrt{\overline{\tau_j^2}}}{\tau_j} \tag{4.9}$$

and analogously $B_{j,-}$ for the lower modes ($j = 5, ..., 8$). Here the overline symbol $\overline{(...)}$ denotes the mean value over all $j = 1, ..., 8$. This normalised balancing factor is independent of the LO power P_{LO} and all coefficients in the mapping from photon flux to voltage. Part c) of Fig. 4.1 shows the variances of the correspondingly balanced voltages. While the differentiation into left-hand and right-hand outputs is still visible, the influence of the individual transmissions after the first beam splitter has been cancelled out. Part d) in Fig. 4.1 shows the $1/\tau_j$ balancing factors used here.

For the BHC evaluation, where every channel has to be balanced with $1/\tau_j^2$, the balancing factors of the upper modes ($j = 1, ..., 4$) are chosen as

$$B_{j,+} = \frac{1}{\mathrm{Var}\left(\frac{U_{j,+}}{\rho_0}\right)} \overline{\mathrm{Var}\left(\frac{U_{j,+}}{\rho_0}\right)} \equiv \frac{\left(\overline{\tau_j^2}\right)}{\tau_j^2}. \tag{4.10}$$

and analogously $B_{j,-}$ for the lower modes ($j = 5, ..., 8$), again independent of LO power and detector constants.

4.1.5. Determination of Field Moments – BHC Evaluation

We will now give a brief explanation of the BHC evaluation process in accordance with the theoretical prescription. Similar to the BHD evaluation, we will first sort the octuples of time coded AC data $U_{\mathrm{AC},j}(t)$ with detector number $j = 1, ..., 8$ into phase bins by their fitted LO phase. Then we calculate the immediate (same-time) correlations for pairs of four detectors as laid out in the BHC scheme. Arbitrarily we decide to always choose 4 detectors in a row, so e.g. detectors $3, 4, 5, 6$.

At this point it would be possible to immediately calculate the mean correlation functions $\Gamma_l^{(4)}(\varphi_i)$ as in Eq. 2.70 for every phase angle respectively as average value over all immediate correlations in the same phase angle bin. This would lead to a single resulting data point of $\mathcal{G}^{(n,m)}$ for the measurement. To get insight into the random error of the measurement, however, we choose to evaluate the average correlations *by blocks*. Thereby we imitate having taken multiple measurements over shorter recording times.

Similar to the BHD evaluation, the number of entries varies between the phase bins. To achieve the same length for all bins we cap all phase bins at the minimum of the entry numbers. Now we divide the length of the phase bins into ten blocks of equal length and perform individual BHC evaluations over them.

The next step is to calculate the quintet of average correlations $\Gamma_l^{(4)}(\varphi_i)$ for each phase angle, where $l = 0, 1, 2, 3, 4$ is the number of detectors from the left-hand side (see Sec. 2.6.1). Then we calculate the binomially constructed function $F^{(4)}(\varphi_i)$ for each phase angle as described in the theory,

$$F_{\mathrm{uncal}}^{(4)}(\varphi_i) = \sum_{l=0}^{4} (-1)^{(4-l)} \binom{4}{l} \Gamma_l^{(4)}(\varphi_i). \tag{4.11}$$

We note explicitly with the subscript $_{\mathrm{uncal}}$ that the results have not been calibrated yet with respect to the experimental constants. We calculate the uncalibrated field moments by performing a Fourier transform via numerical integration

$$\mathcal{G}_{\mathrm{uncal}}^{(4-m,m)} = \binom{4}{m}^{-1} \frac{1}{2\pi} \sum_i F^{(4)}(\varphi_i) e^{-i(4-2m)\varphi_i} \Delta\varphi, \tag{4.12}$$

where $\Delta\varphi = 2^\circ$ is the bin width, and where we have cancelled out the binomial coefficients again.

Performing this procedure over all blocks gives us ten values for every of the five correlation moments $\mathcal{G}^{(n,m)}$ with $n + m = 4$. The evaluation is performed for each one of the measurements with different squeezing strengths.

Calibration

The uncalibrated moments we have determined are as yet given in their measured unit V^4 and are scaled by experimental constants. In the theory section 2.6.2 we have identified the calibration factor

$$C_{\mathrm{cal}} = \left(2\rho_0\tau_0\sqrt{\eta_{\mathrm{Si}}}\eta_{\mathrm{pre}}\,|\alpha_{\mathrm{LO}}|C_{\mathrm{Diode}}\bar{\tau}^2\right)^k \tag{4.13}$$

with which we can calculate the calibrated moments as $\mathcal{G}^{(n,m)}_{\mathrm{cal}} = \mathcal{G}^{(n,m)}_{\mathrm{uncal}}/C_{\mathrm{cal}}$. The calibration factor can be determined in two ways. If the correlation moments to be measured are known from the theory, we can determine the calibration factor by fitting the measured moments to the theoretical prediction (*fit calibration*).

Alternatively, the calibration factor can be determined from ab initio considerations. Using DC and AC measurements with the LO only, we can determine the product $|\alpha_{\mathrm{LO}}|C_{\mathrm{Diode}}$, while the other constants are known from waveguide chip characterisations. For the DC measurement the measured voltage is given by $U_{\mathrm{DC}} = p_1 P_{\mathrm{out}} + p_2$ where P_{out} is the optical power leaving the waveguide chip and p_1 and p_2 are known detector parameters (see Appendix section B). The outgoing power from one of the outputs, under the assumption that the light was reflected off the first beam splitter, is related to the input power via $P_{\mathrm{out}} = P_{\mathrm{in}}\eta_{\mathrm{in}}\eta_{\mathrm{pre}}\rho_0^2\tau_i^2$, where η_{in} is the input coupling efficiency. We find

$$\eta_{\mathrm{in}}\eta_{\mathrm{pre}}\rho_0^2\tau_i^2 = \frac{U_{\mathrm{DC}} - p_2}{p_1 P_{\mathrm{in}}}, \tag{4.14}$$

where all quantities on the right-hand side are known.

Performing a variance measurement on the AC output for the LO as only non-vacuum field gives

$$\mathrm{Var}U_{\mathrm{AC}} = |\alpha_{\mathrm{LO}}|^2\eta_{\mathrm{in}}\eta_{\mathrm{pre}}\rho_0^2\tau_i^2 C^2_{\mathrm{Diode}}. \tag{4.15}$$

Therefore we find

$$|\alpha_{\mathrm{LO}}|C_{\mathrm{Diode}} = \sqrt{\frac{\mathrm{Var}U_{\mathrm{AC}}\,p_1 P_{\mathrm{in}}}{U_{\mathrm{DC}} - p_2}}\,. \tag{4.16}$$

The factors ρ_0 and τ_0 in the calibration factor in Eq. (4.13) are approximately known from the measurements in section 3.2.3. The product of the factors η_{pre} and $\bar{\tau}^2$ can be inferred from measurements of the total transmission T_{total} from the input to all outputs of the chips as $\eta_{\mathrm{pre}}\bar{\tau}^2 = \frac{1}{4}T_{\mathrm{total}}$. The signal beam efficiency η_{Si} can be estimated from knowledge about the components along the signal path.

The measured moments shown in the results section will be fit-calibrated. The agreement of the calibration factors obtained via fit or ab initio is shown in section 4.1.5.

Scatter Plot and Projected Error Bars

Next in our evaluation is the determination of error bars from the sample of blockwise-calculated correlation moments. We will accompany the discussion with the first visualisation of the measured moments in a scatter plot, as shown in Fig. 4.2.

For every squeezing strength (distinguished by the color of the marks), we see the 10 sample entries, here exemplarily for $\mathcal{G}^{(4,0)}$, plotted in the 2D complex plane as circles. Scatter plots for $\mathcal{G}^{(3,1)}$ and $\mathcal{G}^{(2,2)}$ are found in the appendix section C.2. Since $\mathcal{G}^{(1,3)}$ and $\mathcal{G}^{(0,4)}$ are complex conjugates of $\mathcal{G}^{(3,1)}$ and $\mathcal{G}^{(4,0)}$, respectively, they offer no additional insight and we will not discuss them in this work.

As the first step we calculate the mean value of the correlation moments $\bar{G}^{(m,n)}$ for every squeezing strength, as indicated by the x marks in the centres of the distributions. As the first representation of measurement accuracy we calculate the 95 % confidence ellipse of the mean values from the covariance matrix of the 2D scatter fields. These are marked by the ellipses around the mean values.

We aim, however, to display the correlation moments as functions of squeezing strength. For this we will separate the complex correlation moments into magnitude and phase, similar to a Bode plot, and plot them individually against the squeezing strength. The covariance ellipses are not suited for this visualisation, so instead we will now calculate confidence intervals from projections onto magnitude and angle. First we project all sample values from one scatter field onto the polar-radial vector pointing towards the mean value ($\mathbf{e}_r$), and calculate a confidence interval for the magnitude $\left|\mathcal{G}^{(n,m)}\right|$. Then we project all sample values onto the orthogonal polar-angle vector ($\mathbf{e}_\varphi$), calculate the confidence interval and convert the upper and lower limit of the projection into polar angles to obtain a confidence interval of the complex argument $\arg\mathcal{G}^{(n,m)}$. The projected confidence areas of magnitude and complex argument are shown by the wedges around

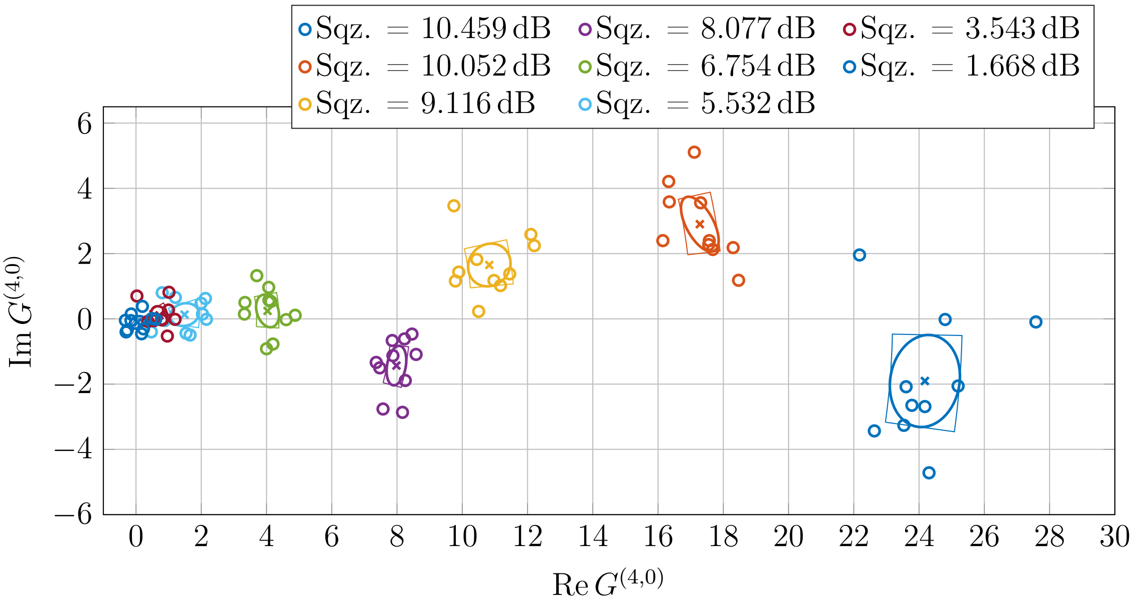

Figure 4.2.: Colour coded scatter fields of blockwise-calculated $\mathcal{G}^{(4,0)}$ moments for different squeezing strengths (legend entries show estimate of squeezing in source). The small circles show the individual realisations of the field moments. The 'x' marks in the centres show the mean value of every scatter field. The ellipses around the centres show 95 % confidence areas of the mean values, calculated from the covariance matrices of each scatter field. The wedges (boxes) around the mean values show confidence areas for magnitude and complex argument of the moments, calculated from the projection of the scatter fields onto radial and angular unit vectors. For better overview some scatter fields near the origin have been omitted. The measured moments are calibrated with the fit calibration (see next section).

the mean values. Typically the wedges slightly overestimate the error area compared to the ellipses.

In the plot we find the measured moments for estimated source squeezing strengths from 1.668 dB (left side, at origin), to 10.459 dB (right side)[2]. With increasing squeezing strength, the magnitude of the field moments increases rapidly. For the lowest squeezing strength the values are grouped around the origin of the plot. Here only statistical noise is seen and the actual correlation moment is overshadowed. No useful phase information is obtained and the phase has to be considered completely undetermined. Fig. 4.3 shows a close-up view of two scatter fields at the origin. The expectation value of the noise floor

[2]Here positive squeezing values mean a reduction of quadrature variance below the vacuum level.

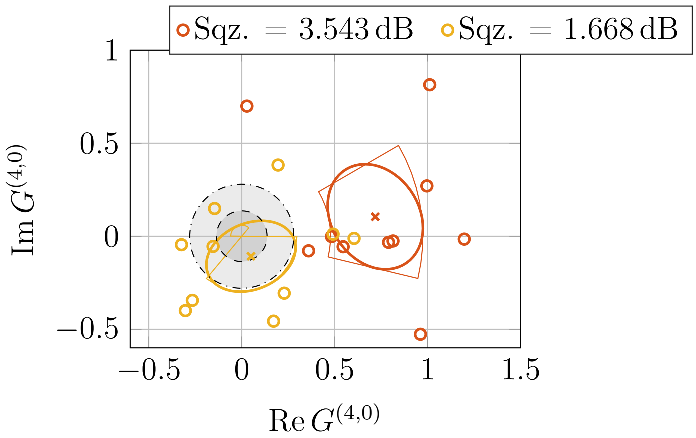

Figure 4.3.: Close-up of correlation moment scatter fields for two selected low squeezing strengths. The grey circles around the origin show the noise floor estimate (dark grey: expectation value, light grey: upper limit of 95 % confidence interval).

as determined from vacuum measurements and the upper limit of the 95 % confidence interval are shown as concentric circles around the origin.

For higher squeezing strengths the complex arguments become meaningful. The scatter fields and their mean values are distributed evenly above and below the real axis in close proximity to it. The measured complex arguments are expected to be proportional to the squeezing angle, as shown in Sec. 2.7. As the pump phase and thereby the squeezing angle is set anew for each squeezing strength (see Sec. 4.1.1), we see a slight variation around the target squeezing angle of $\vartheta = 0$. Overall the confidence ellipses and wedges seem to increase in size with increasing squeezing strength.

Bode Plot with Projected Error Bars

Our key visualisation of the measured correlation moments is the Bode plot. Exemplarily we discuss the results for $\mathcal{G}^{(4,0)}$, with plots for $\mathcal{G}^{(3,1)}$ and $\mathcal{G}^{(2,2)}$ shown in the appendix section C.2. In Fig. 4.4 we see the correlation moments plotted over the estimates of the in-source squeezing strength. The complex valued correlation moments are separated into their magnitude and complex argument. The first plot shows the magnitude of the correlation moments on a linear axis, the second shows the magnitude on a logarithmic axis, and the third plot shows the complex argument.

Error bars are drawn for both the measured correlation moments and the corresponding squeezing strengths. Regular measurement points have blue indicators. For weak squeezing strengths some of the magnitude error bars reach to negative values and can therefore not be represented in a logarithmic plot. Therefore they have been capped in the logarithmic plot by replacing their lower end with a fixed value (here $5 \cdot 10^{-3}$, black or purple indicators). The noise floor as determined from vacuum measurements is indicated by the grey area in the logarithmic plot. Its expectation value is shown by the dashed black line, and the upper limit of the 95 % confidence interval is shown by the black dash-dotted line. Measurement points below the noise floor are shown by yellow indicators.

The theoretically expected correlation moments with respect to the squeezing strength (see Sec. 2.7) are shown by the solid red line. The measured correlation moments have been scaled with a calibration factor determined from a single parameter fit for C_{cal}. In the case of $(n, m) = (4, 0)$, the fit equation $|G^{(4,0)}|_{\mathrm{uncal}} = C_{\mathrm{cal}} \cdot 3 \cosh^2 r \sinh^2 r$ was used, where r is the squeezing parameter (see Sec. 2.3.3). Only measurement points above the noise floor were used for the fit.

We begin our discussion of the measurement results with the magnitude behaviour. For measurements above the noise floor, i.e. for in-source squeezing strengths $\geq 2.5\,\mathrm{dB}$, we find agreement of the measured correlation moments with the theoretical expectation. With increasing squeezing strength the vertical error bar size increases in absolute value, but decreases in relative size. For example, the measured correlation moment for 3.5 dB of squeezing (first above noise floor) is $\left|\mathcal{G}^{(4,0)}\right| = 0.73 \pm 0.25 = 0.73\,(1 \pm 35\,\%)$, while for the highest squeezing strength of 10.46 dB we find $\left|\mathcal{G}^{(4,0)}\right| = 24.3 \pm 1.1 = 24.3\,(1 \pm 4.5\,\%)$.

Concerning the phase, we only find erratic behaviour below the noise floor, while a stabilisation of the phase towards $0°$ is seen for measurements above the noise floor. The error bar size decreases with increasing squeezing strength. For example at 3.5 dB of squeezing the measured phase is $\arg \mathcal{G}^{(4,0)} = 8° \pm 22°$, whereas at 10.46 dB we find $\arg \mathcal{G}^{(4,0)} = -5° \pm 4°$. The scattering above and below $0°$ is plausibly explained by the setting anew of the pump phase (and thereby the squeezing angle) for every squeezing strength.

The plots for $\mathcal{G}^{(3,1)}$ and $\mathcal{G}^{(2,2)}$ in the appendix section C.2 show a similar behaviour. Concerning the magnitude, we find agreement between the measured correlation moments and the theoretical expectation for measurements above the noise floor.

In the case of $\mathcal{G}^{(2,2)}$, all complex arguments are zero, as is expected for the real valued quantity. For $\mathcal{G}^{(3,1)}$ we expect to see a stabilisation of the phase towards $\arg \mathcal{G}^{(3,1)} = -\vartheta - \pi$ for measurements above the noise floor, but the measured phases scatter around $0°$, similar to $\mathcal{G}^{(4,0)}$, for which we expected $\arg \mathcal{G}^{(4,0)} = -2\vartheta$. Both measured phases being

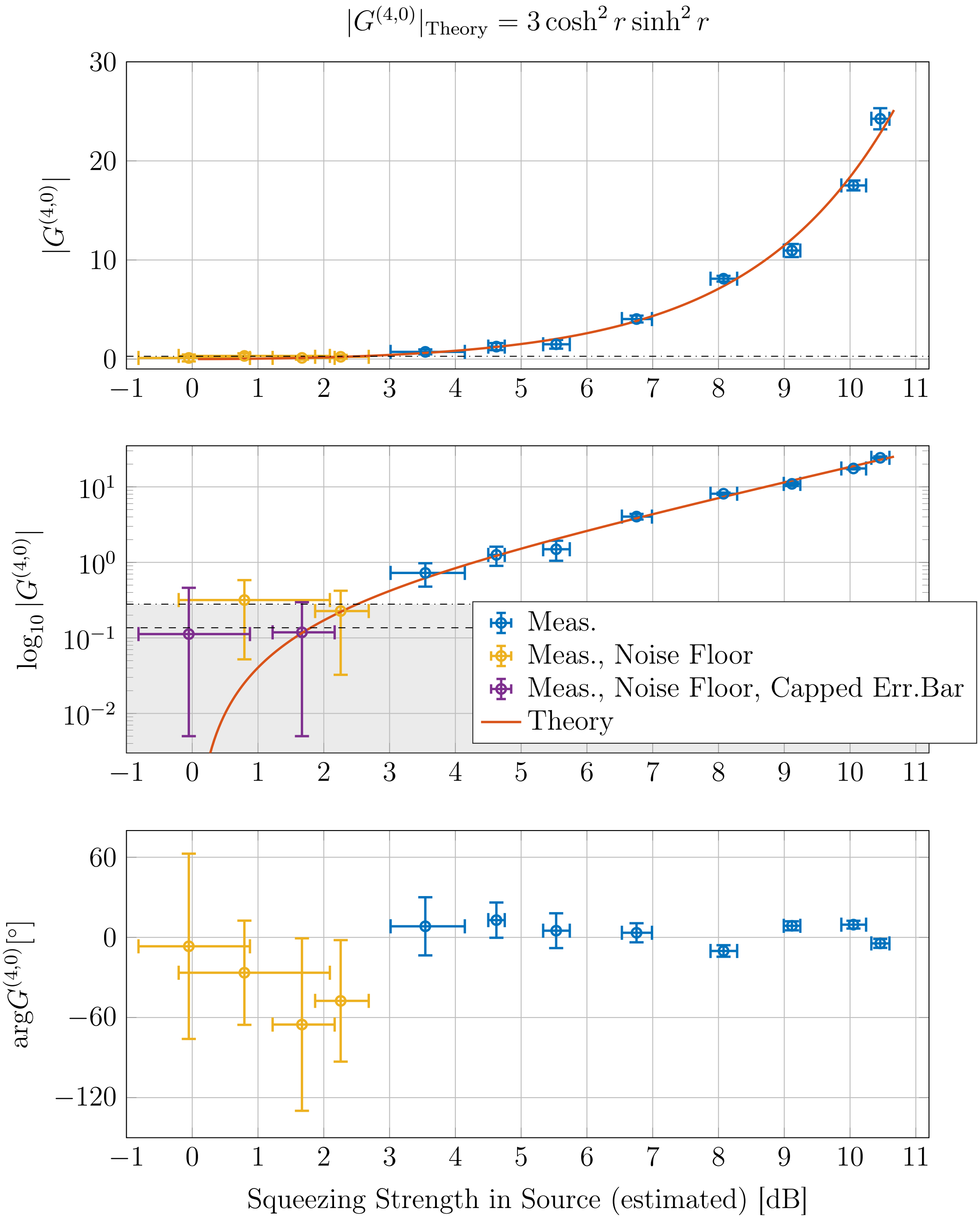

Figure 4.4.: Bode plot of the correlation moments $\mathcal{G}^{(4,0)}$ for squeezed states with varying squeezing strengths. Regular data points are shown in blue. The grey area indicates the noise floor, with the dashed and dash-dotted lines indicating the noise floor's expectation value and the upper confidence limit. Measurements below the noise floor are shown with yellow markers, or purple markers for entries with error bars extending to negative values (capped at $5 \cdot 10^{-3}$ in the logarithmic plot). The red line shows the theoretical expectation of correlation magnitude. The measured correlations have been calibrated using the fit calibration.

centred around 0° is explained by a constant phase offset of 180°.[3] The measured complex arguments rely on the phase scale provided by the interference of the LO with the signal beam. For free space beams we would expect a LO phase of 0° to mean constructive interference between signal beam and LO. In a directional coupler as used in the waveguide chip, however, a symmetric phase shift of 90° is found in the transition from one waveguide path to the other (see symmetric beam splitter matrix, e.g. in [ST19]). The output intensities will therefore evolve as $\cos(\varphi_{\mathrm{LO}} \pm 90°) = \mp \sin(\varphi_{\mathrm{LO}})$, with the sign ($\pm$) depending on the output observed. We can therefore plausibly assume that the choice of recorded DC output did not agree with the chosen (+) sign in the phase fit, and the missing phase offset would be re-introduced by either fitting a $(-\sin)$ in the phase retrieval or adding a 180° offset afterwards. Overall the scattering around 0° is scaled back by a factor of approximately 2 in comparison with $\mathcal{G}^{(4,0)}$, in agreement with the expectation.

In summary we find the magnitudes of the correlation moments to scale with the squeezing strength as expected for measurements above the noise floor. The complex argument is increasingly well determined for increasing squeezing strength and behaves as expected. Lowering the noise floor by increasing the measurement time would be useful to allow the measurement of weaker moments.

Comparison of Calibrations

Figure 4.5 shows the overlap of the calibration factors as determined from the fits of the measured correlations to the theoretical expectations for $\mathcal{G}^{(4,0)}$, $\mathcal{G}^{(3,1)}$ and $\mathcal{G}^{(2,2)}$, as well as the ab initio calibration factor. All calibration factors overlap. The ab initio factor has, however, larger error bars due to the uncertain knowledge of the required experimental parameters, amplified by the exponentiation to the power of $k = 4$ (see Eq. 4.13).

4.2. Verification of Loss-Behaviour

A strong advantage of correlation methods is that losses only have influence as a scaling factor, but do not explicitly mix in vacuum characteristics. For our device of depth $d = 3$, with correlations calculated over pairs of four detectors, we expect a scaling with signal beam efficiency as η_{Si}^2, if the losses are not accounted for. To verify that this behaviour

[3] $e^{-i2\vartheta} = -e^{-i\vartheta} \Leftrightarrow \vartheta = \pm\pi \ (+n \cdot 2\pi), \quad n \in \mathbb{Z}$

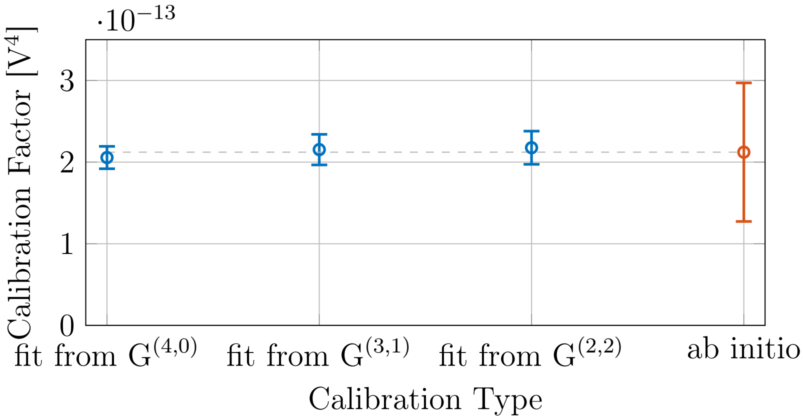

Figure 4.5.: Overlap of calibration factors from fit and from ab initio considerations.

is shown we will now introduce ND filters of varying intensity transmission T in the signal beam path, measure the correlation moments for a squeezed state, and check if the measured moments scale as T^2.

4.2.1. Method

The measurement procedure for the loss investigation is similar to the measurements with different pump powers, only that instead of changing the pump power the ND filter is changed between measurements. We prepare a squeezed state using a moderate pump power of 50 mW. The OPA's control beam power was again 500 µW. The squeezing in the source, estimated from the BHD measurements, was 7.2 dB with a 95 % confidence interval of [6.9 dB, 7.6 dB].

We place a ND filter after the OPA, before the flip-mirror, so that the attenuated beam can be sent to both the BHD and the BHC set-up. A BHD measurement is performed first, then the flip mirror is placed again and a BHC measurement is performed. Then the ND filter is changed and the procedure is repeated. Additionally a measurement is performed without a ND filter, i.e. with $T = 1$. All ND filter transmissions were determined beforehand by power measurements before and after the respective filter.

4.2.2. Results

We will now discuss the measurement results based on the Bode plot. Figure 4.6 shows the correlation moments $\mathcal{G}^{(4,0)}$ plotted against the ND filter transmission T, with error bars in both dimensions. Additional plots for $\mathcal{G}^{(3,1)}$ and $\mathcal{G}^{(2,2)}$ are shown in the appendix section C.3. Again the magnitude is shown on both a linear and a logarithmic axis, and the complex argument is shown on a linear axis.

Regular measurement points are shown by blue indicators. As before, the grey area shows the noise floor, with the expectation value and the upper limit of the confidence interval displayed as dashed and dash-dotted lines. Measurement points below the noise floor are shown by yellow markers. In the logarithmic plot the purple indicators denote points below the noise floor, for which the lower end of the error bar extends to negative values and has been capped at $1 \cdot 10^{-2}$. For the transmission $T = 0.73$ two data points are shown. Here the measurement was repeated as a precaution because of hints of instability in a cavity lock. The original point is shown in dark red and the repetition is shown in blue.

The red line shows the theoretically expected scaling of the correlation moments with transmission as $|G^{(4,0)}|_{\text{theory}} = |G^{(4,0)}|_{T=1} \cdot T^2$. The measured correlation moments are again calibrated using the fit from before.

Considering the magnitudes first, we see agreement of the measured correlation moments with the theoretical expectation.

Concerning the complex argument we find the measured phases for $T = 0.35$, $T = 0.73$ (both original and repeated), and $T = 1$ to show the expected overlap, while the phase for $T = 0.55$ deviates. The behaviour for $T = 0.55$ is consistent with a deviation in squeezing angle found in the BHD evaluation (not shown).

For the correlation moment $\mathcal{G}^{(3,1)}$, shown in Fig. C.7, we similarly find agreement of the magnitudes with the theoretical expectation. The phases overlap for the same transmission values as above, again with a deviation for $T = 0.55$. For $\mathcal{G}^{(2,2)}$, as seen in Fig. C.8, we also see agreement between the measured magnitudes and the theory curve. Since $\mathcal{G}^{(2,2)}$ is real valued all complex arguments are $0°$, allowing no influence of losses on the complex argument.

Overall the scaling of the magnitude with transmission as T^2 was verified. To investigate the phase behaviour further we recommend a repetition of the measurement with additional scrutiny towards experimental parameters in the state preparation.

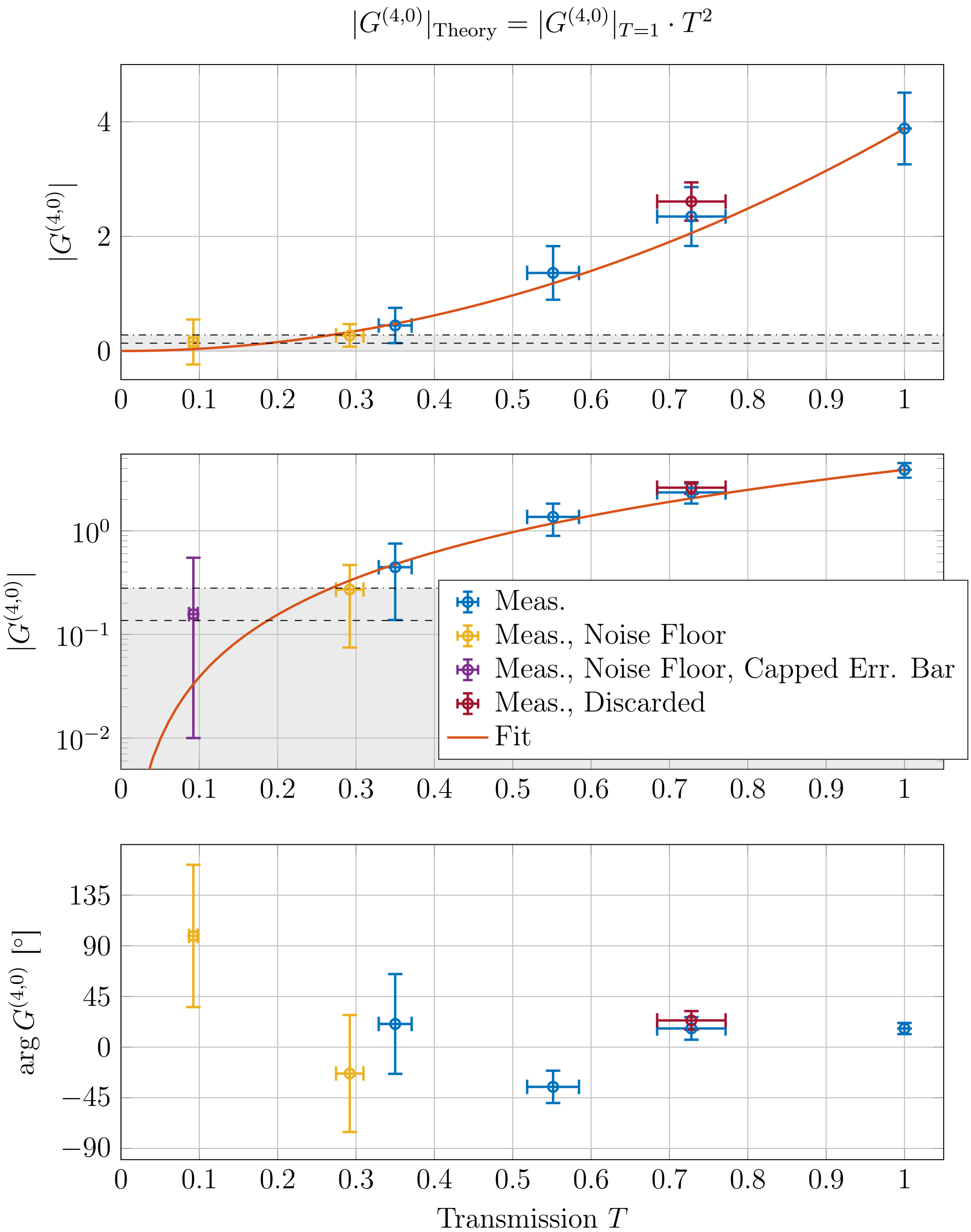

Figure 4.6.: Bode plot of $\mathcal{G}^{(4,0)}$ correlation moments for different ND transmissions T. Blue markers indicate regular measurement point. The grey area shows the noise floor, with the dashed and dash-dotted lines indicating its expectation value and upper confidence limit. Yellow markers indicate measurements below the noise floor, the purple marker in the logarithmic plot additionally indicates that for this measurement point the lower end extends to negative values and was capped at $1 \cdot 10^{-2}$. For $T = 0.73$ the measurement was repeated, with the original data point shown by a dark red marker. The red line shows the theoretical expectation of correlation magnitude. The measured moments were calibrated with the fit from above.

4.3. Correlation Measurements for Coherent States of Varied Powers

So far we have used squeezed states as signal states. Since we were using the AC output of the photodiodes and applied a bandpass filter from 6 MHz to 8 MHz, we effectively saw squeezed vacuum states. The coherent displacement at the laser frequency therefore had no influence on the measured correlation functions.We will now explicitly test the influence of coherent displacement by measuring correlation functions for coherent states of different powers. The goal is to show that varying the coherent power has no influence on the measured correlation functions.

4.3.1. Method

In this experiment we operate the OPA without the pump beam and use the weak transmission of the coherent control beam through the OPA cavity as our signal beam. We vary the input power of the control beam from 302.5 µW to 1050 µW to create a signal beam with powers ranging from 1.44 µW to 5.16 µW. The signal powers are therefore on the same order as in the measurement with varied squeezing strength, where the signal field power varied from 1 µW to 2.2 µW. The LO power in the BHC measurement was $P_{\mathrm{LO}} = 6.26\,\mathrm{mW}$, so that the homodyne condition $P_{\mathrm{LO}} \gg P_{\mathrm{Signal}}$ is fulfilled for all signal powers. In each measurement step a new control beam power is set and measured, the signal beam power is measured, and then a BHC measurement is performed.

4.3.2. Results

The Bode plot in Fig. 4.7 shows the measured correlation moments $\mathcal{G}^{(4,0)}$, separated into magnitude and complex argument, plotted against the coherent signal beam power P_{Signal}. Bode plots for $\mathcal{G}^{(3,1)}$ and $\mathcal{G}^{(2,2)}$ are shown in appendix section C.4. As before, the grey area and the dashed and dash-dotted lines indicate the noise floor, its expectation value, and the upper limit of its confidence interval.

Considering the magnitude plot, we find all measurement points to be within the noise floor or slightly above, with large overlap between all vertical error bars. The measured phases show large error bars and behave erratically. The measured magnitudes and phases for $\mathcal{G}^{(3,1)}$ (Fig. C.12) and $\mathcal{G}^{(2,2)}$ (Fig. C.13) show a similar behaviour.

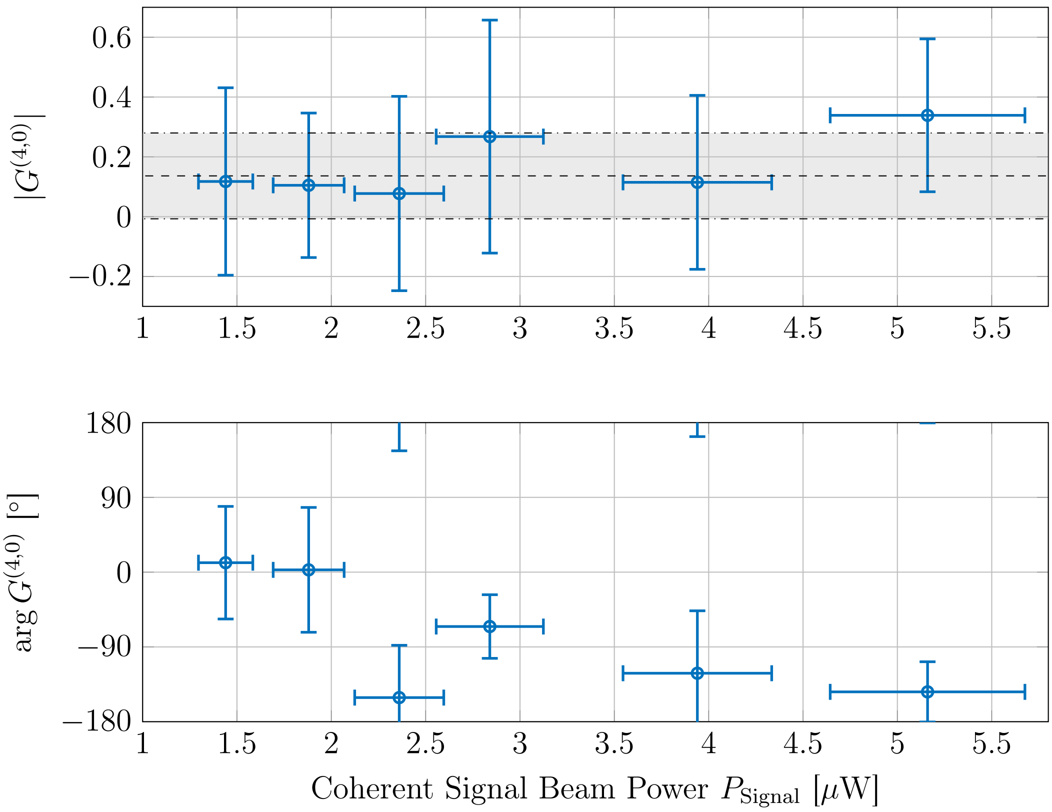

Figure 4.7.: Correlation moments $\mathcal{G}^{(4,0)}$ in magnitude and complex argument measured for a coherent beam as signal field for varied beam power. The error bars of the complex argument wrap around the ±180° margins. The grey area indicates the noise floor, with the dashed and dash-dotted lines showing its confidence bounds. The measured correlations are calibrated with the fit result from above.

Overall we can assume that only statistical noise from the noise floor was seen. We conclude that variations in the signal power had no measurable influence on the correlation moments, as was the expectation.

5. Summary and Outlook

In this work we have realised balanced homodyne correlation (BHC) measurements for the first time. From the theoretical description we saw that BHC enables the determination of both even and odd ordered correlation functions, i.e. field moments with equal or unequal powers of creation and annihilation operators, as is required for a complete description of the most general correlation and coherence properties. With strong local oscillators (LO) allowed, high moments become accessible with strong signal to noise ratio, where previous methods fell short. Due to the correlative nature of the measurement, losses act only as a scaling factor and do not mix in vacuum characteristics, in stark contrast to balanced homodyne detection.

In the experimental implementation we overcame several technical challenges. We created the required beam splitter cascade in a femtosecond laser written waveguide chip, offering stability and compactness, as well as future scalability. From the two inputs for LO and signal beam eight outputs are generated in three layers of beam splitters. With eight outputs correlation moments up to fourth operator power become measurable. The relative output powers varied around the ideal ideal 12.5 % mark from 10.25 % to 14.94 %, while the individual beam splitter reflections were estimated to vary from 45.4 % to 52.7 %. As this was the first time waveguide structures were used in our workgroup, additional infrastructure had to be created (e.g. self-written camera analysis software).

To account for the imperfect splitting ratios and uneven transmissions along the beam splitter cascade we have added to the BHC theory a discussion of the realistic case found in the experiment. We learned that, first, an imbalanced splitting at the first beam splitter only introduces a scaling factor, but does not introduce unwanted parasitic moments in the case of AC filtering, and second, that uneven transmissions τ_j after the first beam splitter can be adjusted for in the post processing if they are known. Experimentally the transmissions were determined from the distribution of shot noise over the output modes. Third, we have seen that losses of the signal beam only scale the measured moments as expected.

For the detection of the tightly spaced output fields we used a 1x8 photodiode array, where gold wire bonding was necessary to create the fine connections from the integrated array to the carrier PCB. Further an eight channel ultra low noise, high speed transimpedance amplifier was constructed and tested. An FPGA based solution was found to implement the required high bandwidth data acquisition with eight fast channels at 50 MS/s each.

For the multibeam coupling into the chip and the imaging of the eight output modes onto the detector we found collimating, confocal lens set-ups, that fulfil all modematching and pitch-conversion requirements. Additionally this allowed beams running in parallel to remain parallel in the output, and to suppress stray light disturbances.

To verify our set-up we performed BHC measurements for test states with known correlation moments. In a first test we employed squeezed states to see if the correlation moments scale with squeezing strength as expected. For measurements above the noise floor, i.e. for in-source squeezing strengths $\geq 2.5\,\mathrm{dB}$, we found agreement between the measured correlation magnitudes and the theoretical expectation. The complex arguments showed a small variation as was expected due to the setting anew of the squeezing angle for each measurement. With increasing squeezing strength and therefore increasing correlation magnitude, the correlation moments could be measured with increasing sharpness, so that for 10.46 dB of squeezing in the source the relative error of the magnitude had diminished to $\pm 4.5\,\%$, while the phase error was $\pm 4°$. From the fits of the measured moments to the theory curve we generated calibration factors, which agree with the factor found from ab initio considerations. The ab initio factor, however, shows larger error bars due to the imperfect knowledge of experimental constants, amplified by the exponentiation to the power of $k = 4$.

In our second test we verified the BHC loss behaviour by placing ND filters in the signal beam path and measuring the correlation moments of a squeezed state. The measured magnitudes agree with the theoretically expected T^2 scaling. The measured complex arguments overlap (as is expected) for four out of the five measurement points above the noise floor. The deviation of the fifth point is consistent with the deviation in squeezing angle found in the BHD evaluation. A repetition of the measurement with additional scrutiny towards experimental parameters concerning the state preparation can clear remaining uncertainties.

In our final test we verified that coherent displacement has no influence on the correlation moments by performing BHC measurements for coherent states of varied power. We found all correlation magnitudes to be within the noise floor or close to it, with a large overlap between the magnitude error bars. The measured phases behave erratically and show large error bars. Overall we can assume than only statistical noise from the noise floor was seen, so that no measurable dependency of the correlation moments on the coherent displacement was found.

In conclusion, we have successfully implemented the BHC scheme for the measurement of correlation moments $\mathcal{G}^{(n,m)}$ up to fourth operator power ($n + m \leq 4$), and have shown that the measured correlation moments for squeezed states and coherent states agree with the theoretical expectation. As a final step of this work we will now show future perspectives enabled by our BHC implementation, starting with immediately available further investigations, and then moving on to more involved future projects.

The access to weak moments was limited by the statistical noise floor. A simple way to lower the noise floor will be to increase the measurement time. The data we have used so far were produced by a single run in the acquisition program. It is easily possible to increase the measurement time by performing many acquisition loops in sequence as described in the set-up section 3.5.2. Limits will be posed by the long term stability of the locking circuits and thereby the stability of the generated state.

Normalised correlation functions, i.e. correlation moments normalised by the signal field's intensity, are a standard tool in state characterisation [Lai+22; GK05; WM08]. Especially the second order normalised correlation function $g^{(2)}$ is widely used. To connect our work to previous results in the field, it will be useful to determine normalised correlation functions from BHC measurements.

The deepening of our understanding of nonclassical correlations and their possible technological applications is a subject of continuous research. The measurement of correlation moments of even or uneven operator powers lends itself to the determination and characterisation of nonclassicality as described in [Vog08], where nonclassical correlation properties are completely described by minors from normally and time-ordered field correlation functions as are accessible from BHC measurements. With correlation moments up to fourth operator power measured for squeezed states and coherent states, a next step will be to identify a nonclassicality condition fitting our set-up and the application to our measured correlation moments.

Correlation functions cannot only be determined from correlation measurements. It was shown that even ordered correlation moments can be determined from homodyne measurements, by either performing phase averaged measurements with a single BHD pair of detectors [MR97], or by detecting conjugate quadratures simultaneously with two pairs of BHD diodes [Gro+07] (see also [Lai+22] for a review). It is however possible, to determine both even or odd ordered correlation functions from homodyne measurements, as Andrii A. Semenov from the Bogolyubov Institute for Theoretical Physics in Kyiv has shown to us in a discussion. In the BHC theory the combination of direct correlation measurements between sets of detectors yields a function $F^{(k)}(\varphi)$ which is proportional to the normally ordered k-th moment of the quadrature operator, $\langle : \hat{\chi}^k(\varphi) : \rangle$. From this the correlation moments were found via Fourier transform. The normally ordered moments of the quadrature can, however, also be rewritten in terms of generic quadrature operator moments, and hence become accessible by BHD. In the appendix section D we show the relationships up to the fourth moment. Since we can perform both BHD and BHC measurements on a given state with our set-up, we are in a great position to test the quadrature moment based technique, and to compare the two methods.

So far we have applied the BHC technique to squeezed and coherent states. A first additional state we can expand our investigation to is the phase-diffused squeezed states, which is relevant to the field of quantum communication due to its link to the transmission of a pure squeezed state through a channel exhibiting phase noise [Fra+06; Hag+07; Kie+09]. From our measured phase-sensitive BHD and BHC data it will be possible to emulate the measurement on a phase-diffused state by resampling randomly from a chosen interval of phase bins.

Another state of particular interest due to its strong nonclassicality is the Schrödinger cat state, which is a superposition of two coherent states of diametrically opposed coherent amplitudes [GK05]. Cat states of weak amplitude, so called *kitten states*, can be conditionally generated by photon subtraction from a weakly squeezed state. Here a small part of the state is separated off using an unbalanced beam splitter and sent to a click detector. Thereby a conditional measurement can be performed when a photon is detected [Nee+06; Our+06]. With access to both squeezed states and a superconducting nanowire single photon detector (SNSPD) in our lab[1], performing BHC measurements on kitten states is a compelling next step.

Last but not least it will be important to investigate the scaling of our device to more outputs to allow access to higher order correlation moments. A first step will be, following the current design, to add another layer of beam splitters, thereby yielding 16 outputs. For this approach a limit will be posed by the minimal length a beam splitter can have without introducing significant losses from the curvature of the waveguide. Another approach might be to use alternative beam splitter designs which generate more than two outputs (see [Wei+96; Kow+05], and [Spa+13] for an overview). Thereby a greater number of outputs could be achieved in the same chip length.

[1] In fact our SNSPD was lent out to the group of Roman Schnabel in Hamburg precisely for kitten state experiments, see the Ph.D. thesis of Julian Göttsch on kitten state growth [Göt22].

A. Mode Profile, Coupling Ratios and Output Distributions of Waveguide Chip mk.4

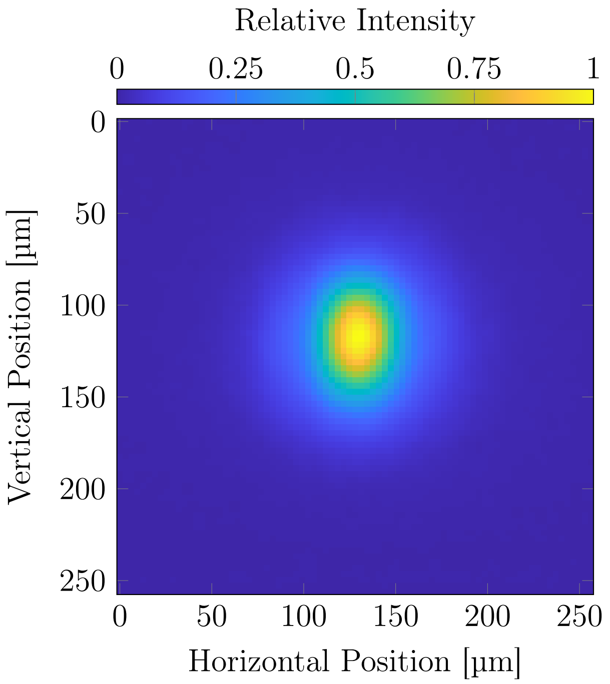

Figure A.1.: Mode profile. Horizontal and vertical positions refer to positions on the camera.

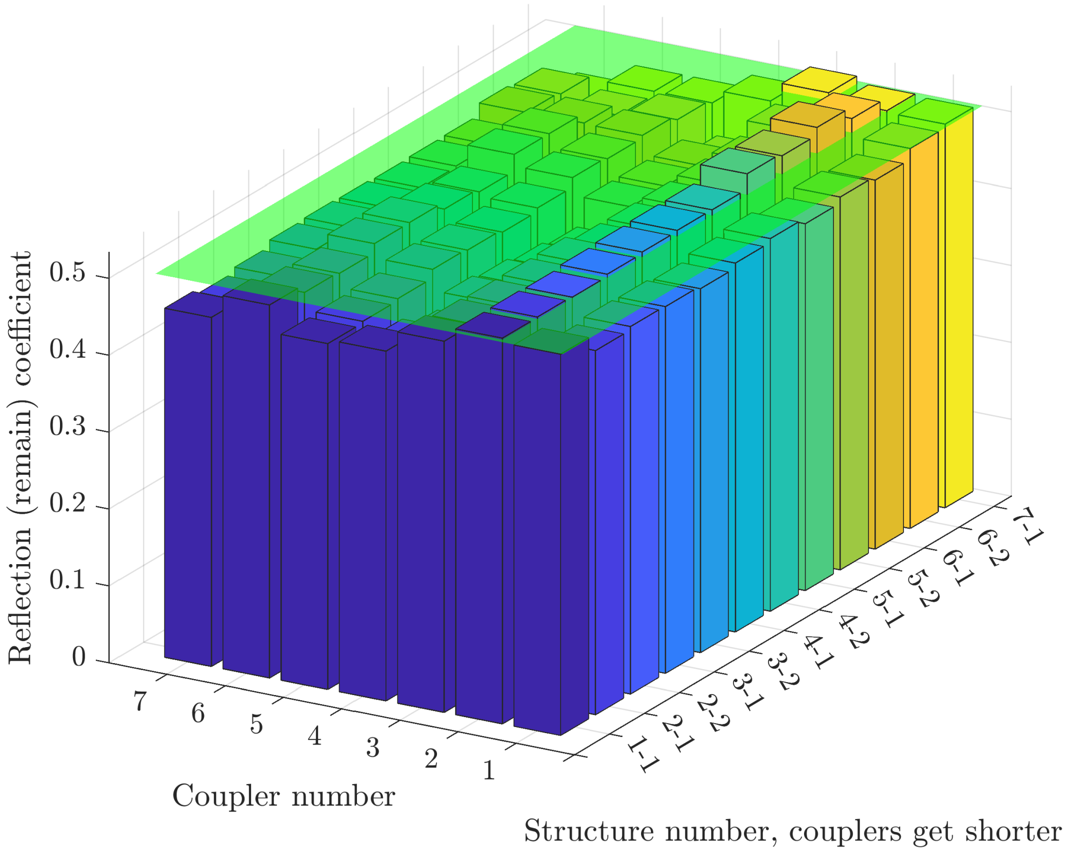

Figure A.2.: Reflection coefficients for all couplers and all structures in waveguide chip mk.4. The green plane indicates ideal 50:50 splitting.

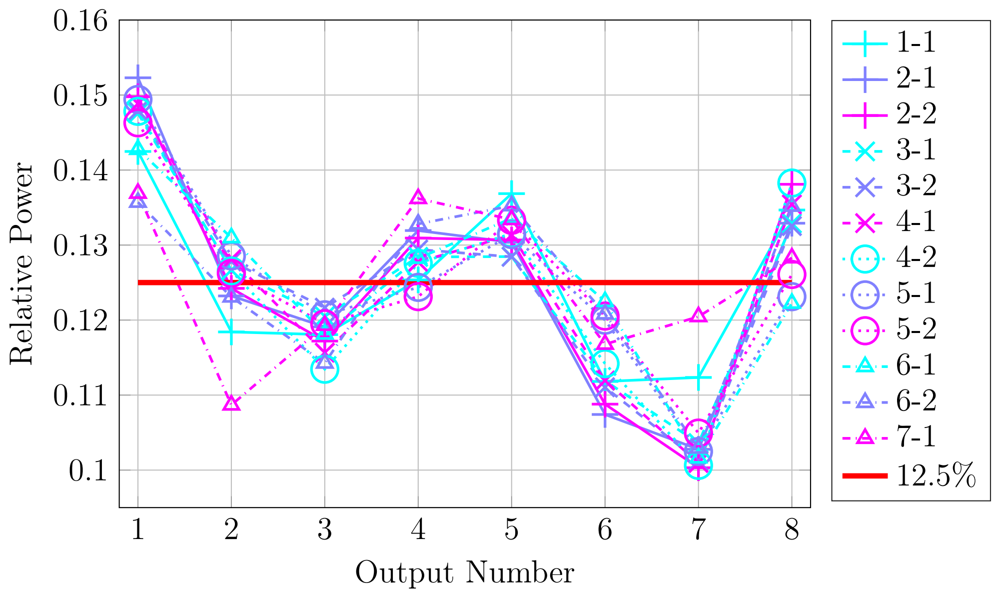

Figure A.3.: Comparison of relative output powers for all structures in waveguide chip mk.4. The red line indicates ideal $1/8 = 12.5\,\%$ splitting.

B. Detector Details

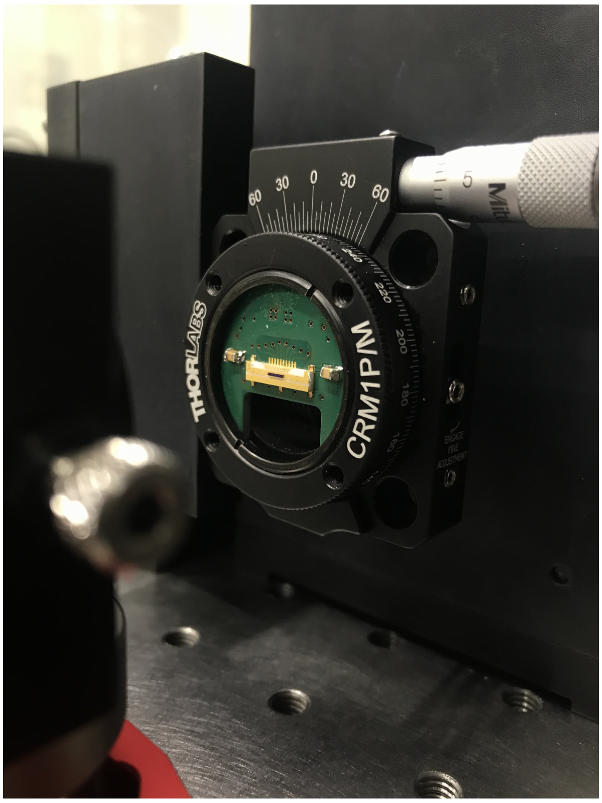

Figure B.1.: Carrier PCB with diode array in rotating mount. The actual photodiodes are found in the small black bar in the middle of the golden ceramic.

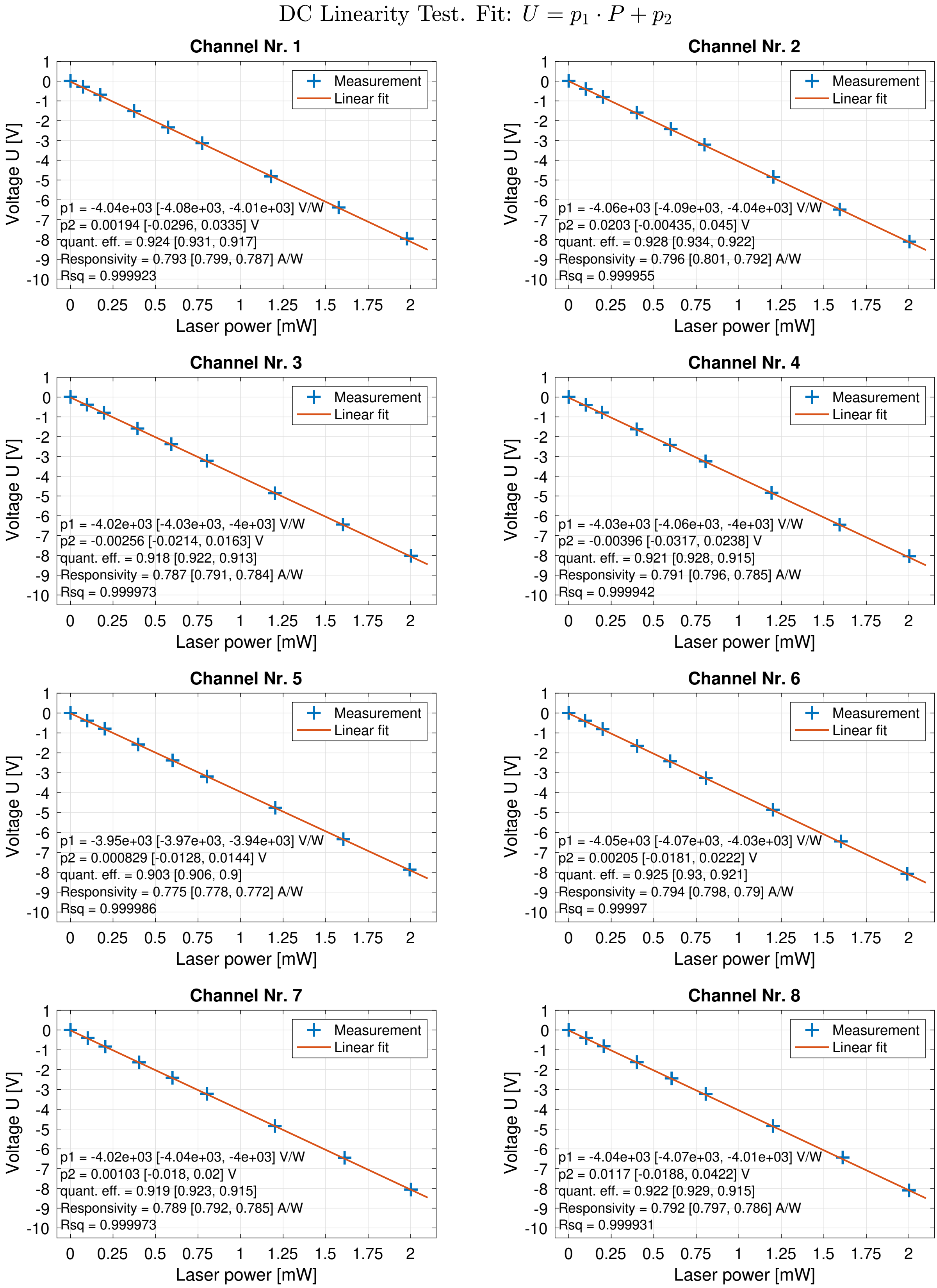

Figure B.2.: DC linearity test results for all eight photodiode circuits.

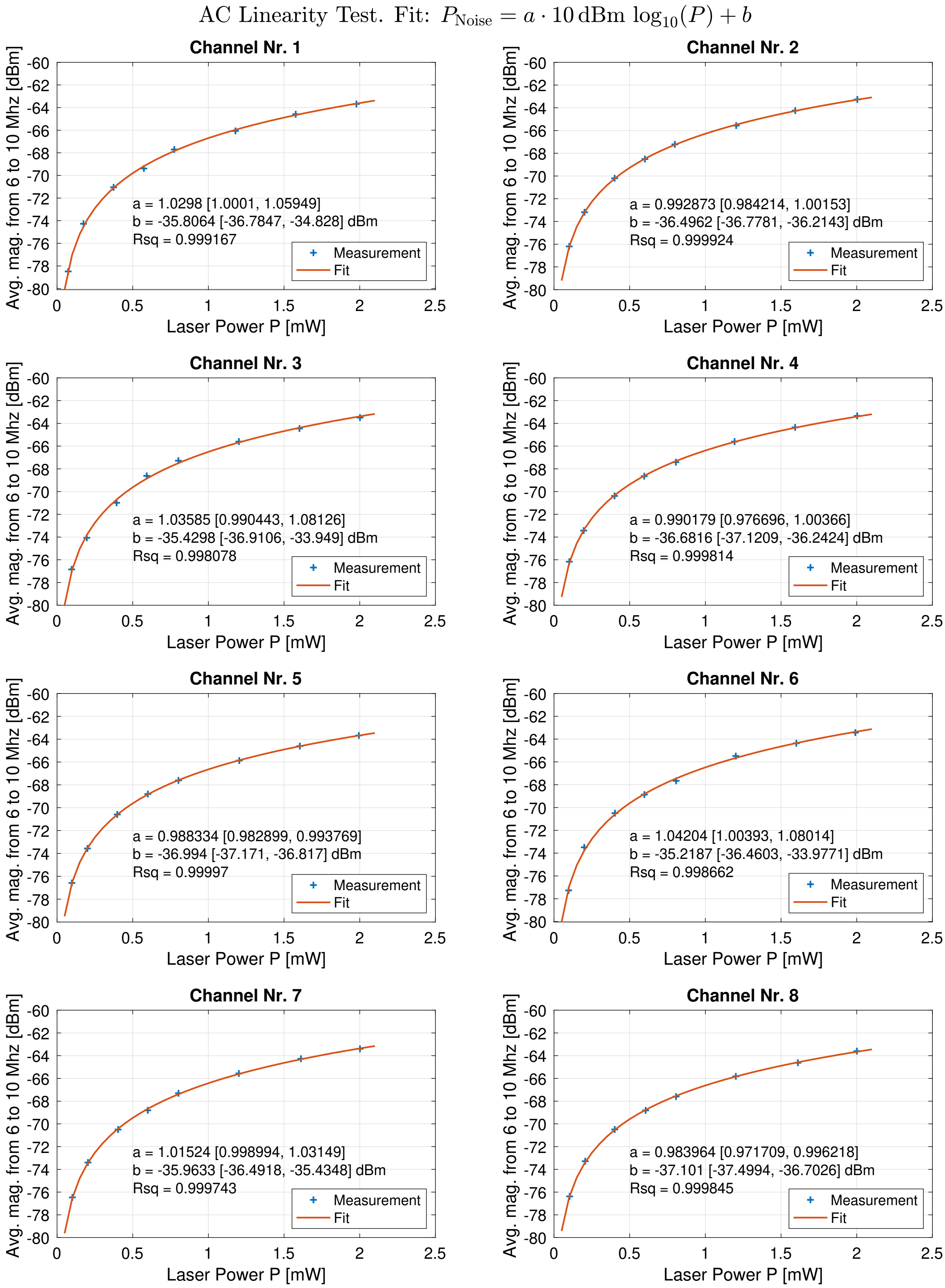

Figure B.3.: AC linearity test results for all eight photodiode circuits.

C. Additional Plots

C.1. Quadrature Variance Curve from Balanced Homodyne Detection

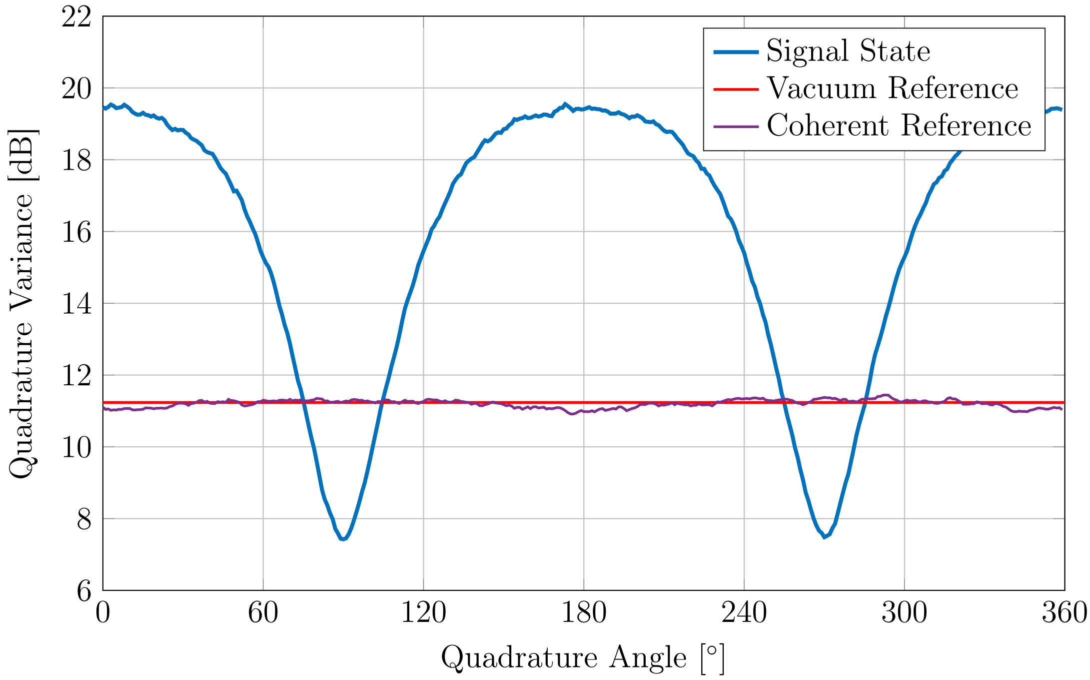

Figure C.1.: Exemplary curve of quadrature variance in dependence of phase angle, $\mathrm{Var}\,\hat{\chi}(\varphi)$, for a squeezed state produced with 100 mW of pump power. We find $-3.82\,\mathrm{dB}$ of squeezing with a 95 % confidence interval of $[-3.91\,\mathrm{dB}, -3.73\,\mathrm{dB}]$ and $8.40\,\mathrm{dB}$ $[8.30\,\mathrm{dB}, 8.50\,\mathrm{dB}]$ of anti-squeezing. It is estimated that in the source $-10.05\,\mathrm{dB}$ $[-10.24\,\mathrm{dB}, -9.87\,\mathrm{dB}]$ of squeezing were produced.

C.2. Correlation for Different Squeezing Strengths

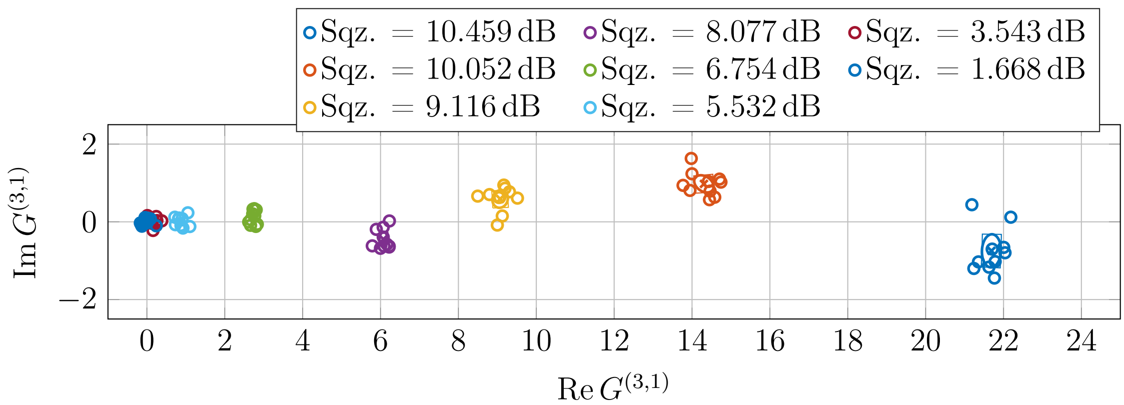

Figure C.2.: Scatter fields for correlation moment $\mathcal{G}^{(3,1)}$ for different squeezing strength.

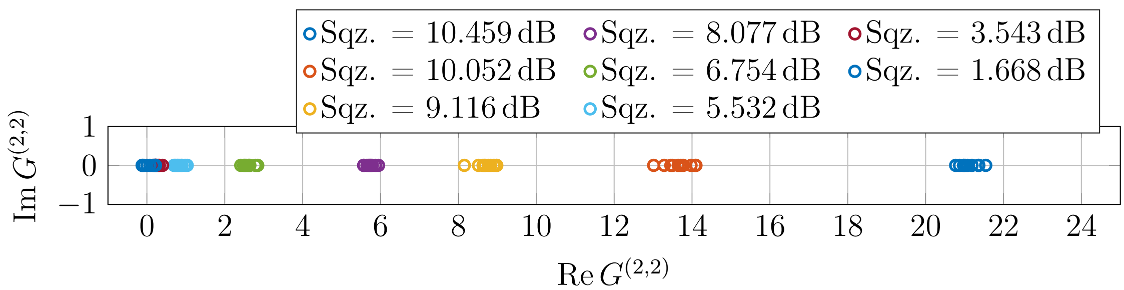

Figure C.3.: Scatter fields for correlation moment $\mathcal{G}^{(2,2)}$ for different squeezing strength.

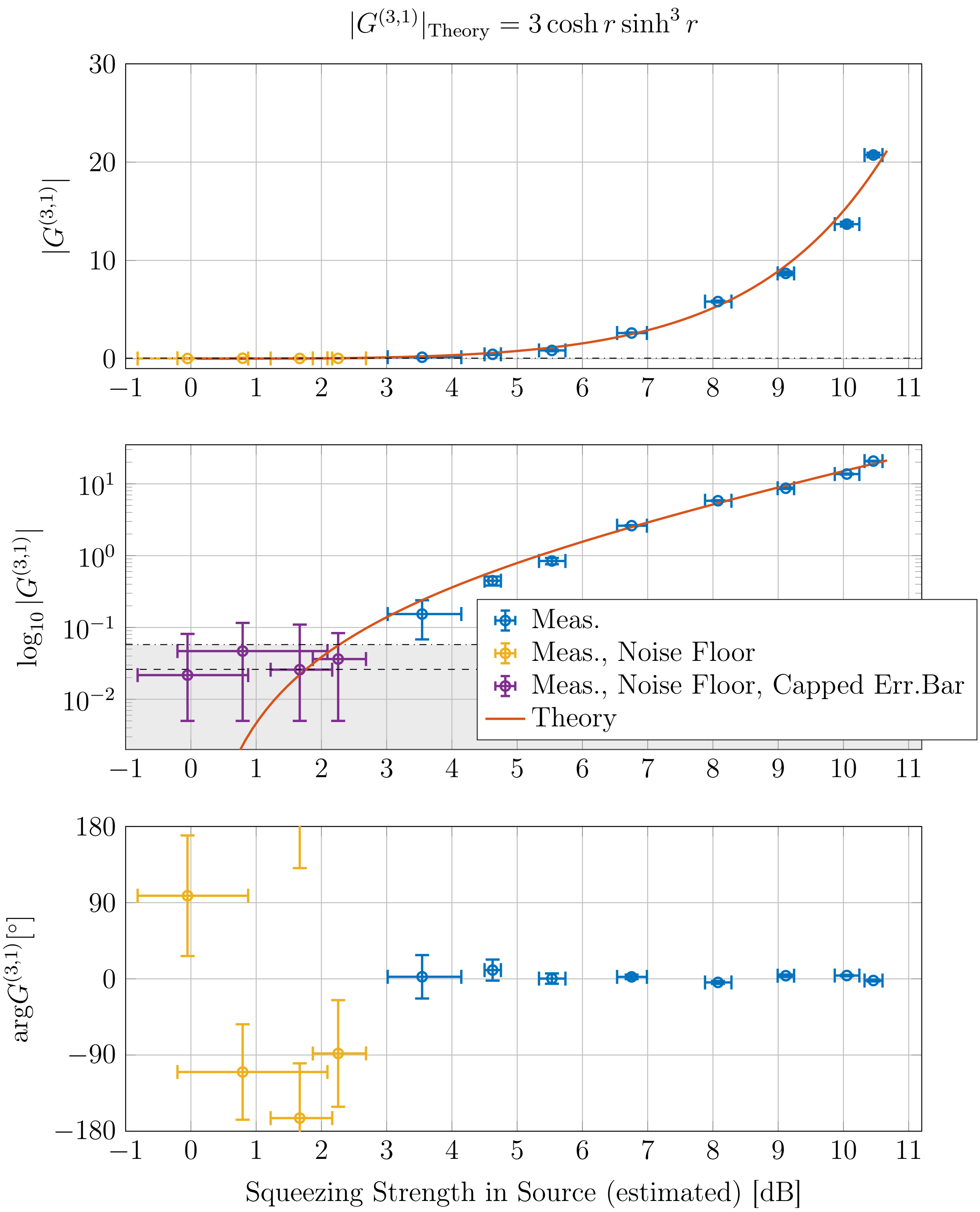

Figure C.4.: Bode plot of correlation moments $\mathcal{G}^{(3,1)}$ for varied squeezing strength. The grey area indicates the noise floor, with the dashed and dash-dotted line showing the expectation value and the upper confidence limit.

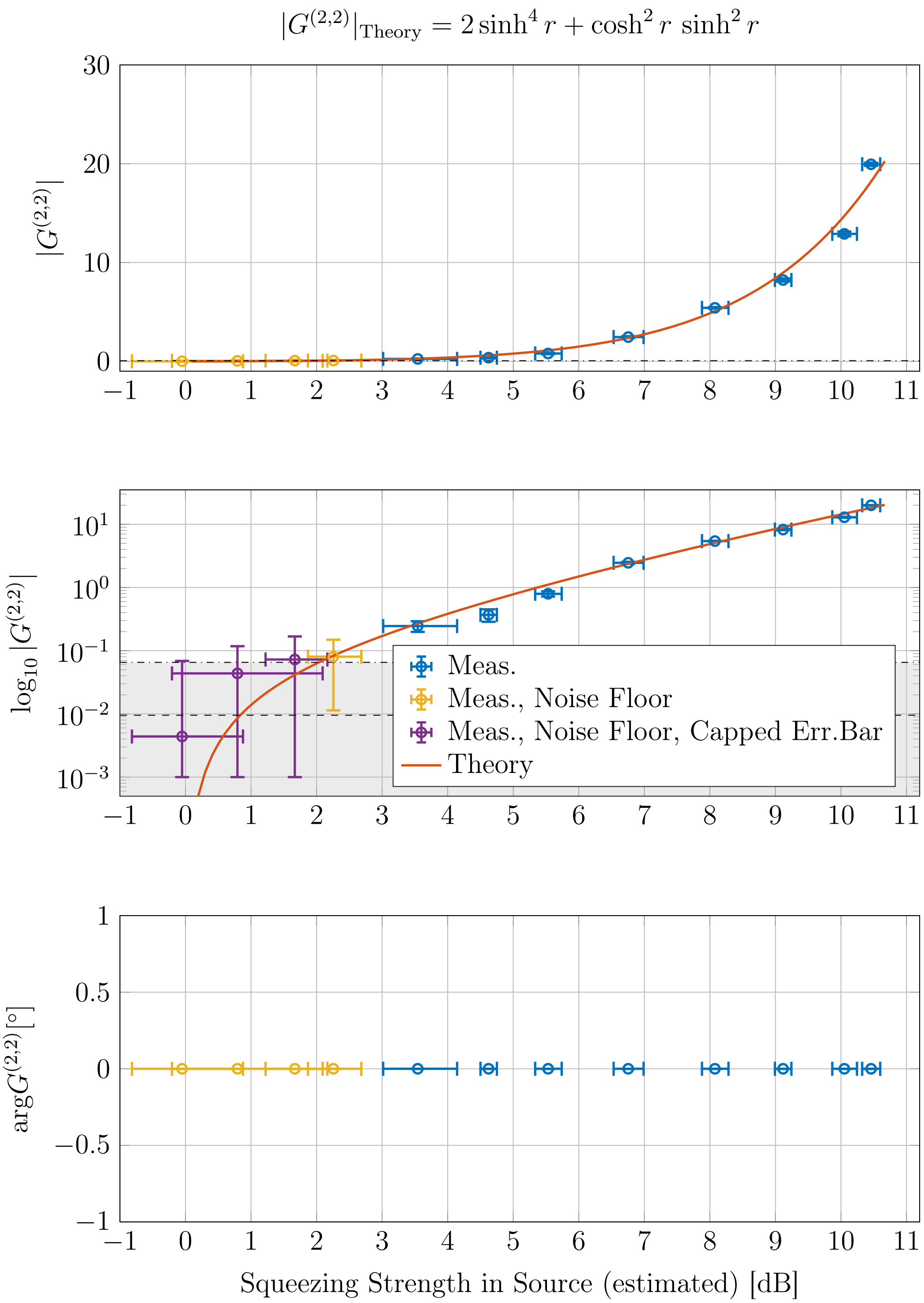

Figure C.5.: Bode plot of correlation moments $\mathcal{G}^{(2,2)}$ for varied squeezing strength. The grey area indicates the noise floor, with the dashed and dash-dotted line showing the expectation value and the upper confidence limit.

C.3. Correlation for Different Losses

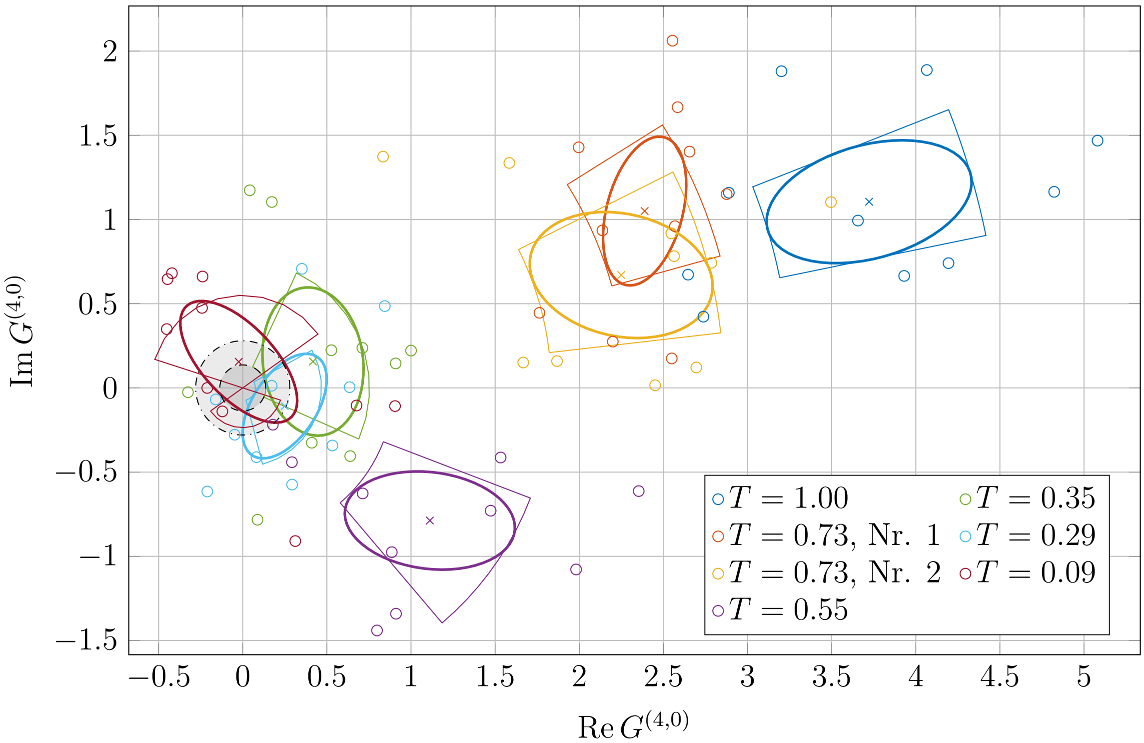

Figure C.6.: Scatter plot of measured correlation moments $\mathcal{G}^{(4,0)}$ for a squeezed state for varied ND filter transmission T in signal beam. Noise floor indicated by dark- and light grey circles at origin (expectation value and upper confidence limit).

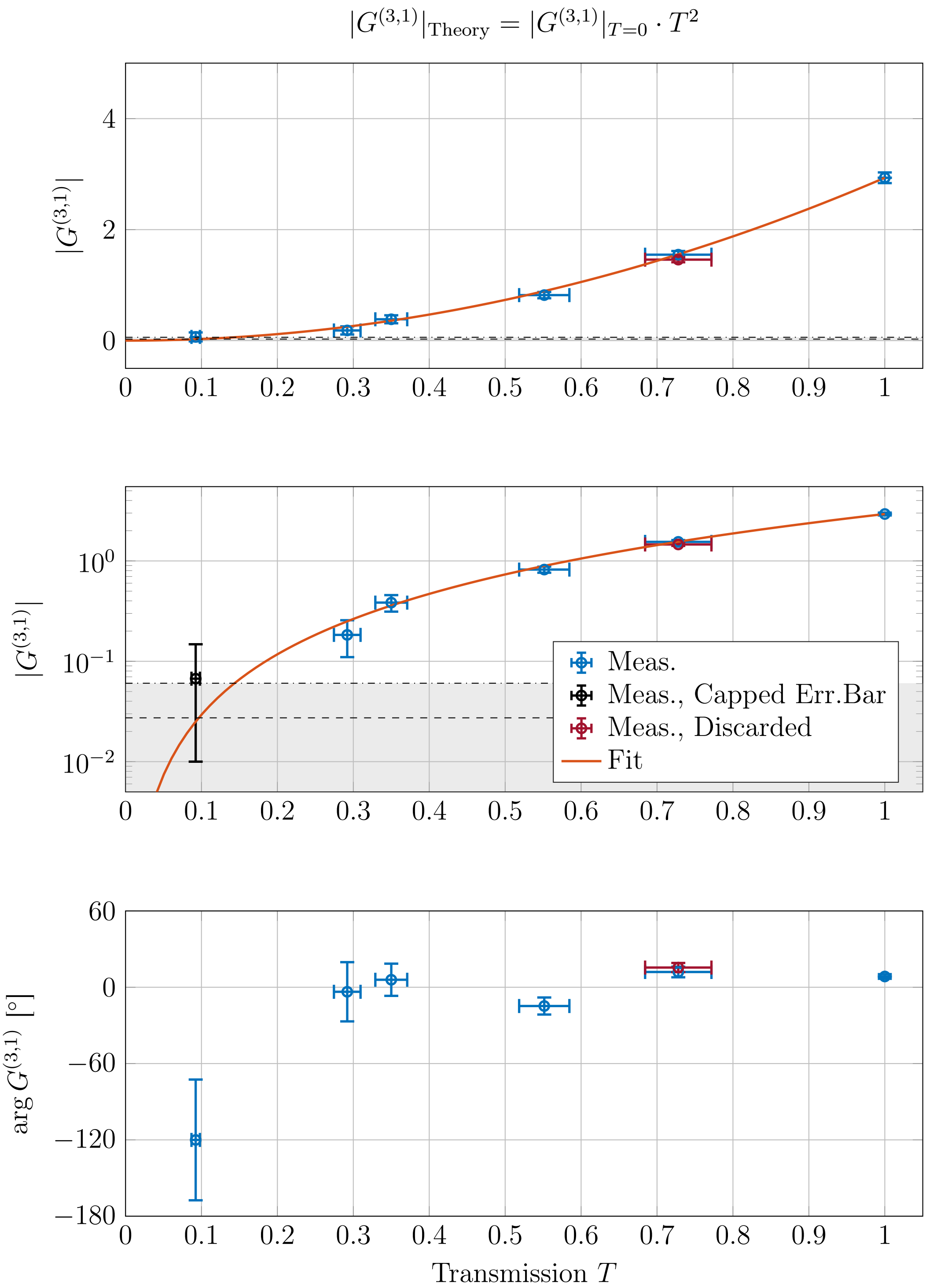

Figure C.7.: Bode plot of measured correlation moments $\mathcal{G}^{(3,1)}$ for a squeezed state and varied ND filter transmission T in signal beam. The grey area indicates the noise floor, with the dashed and dash-dotted line showing the expectation value and the upper confidence limit.

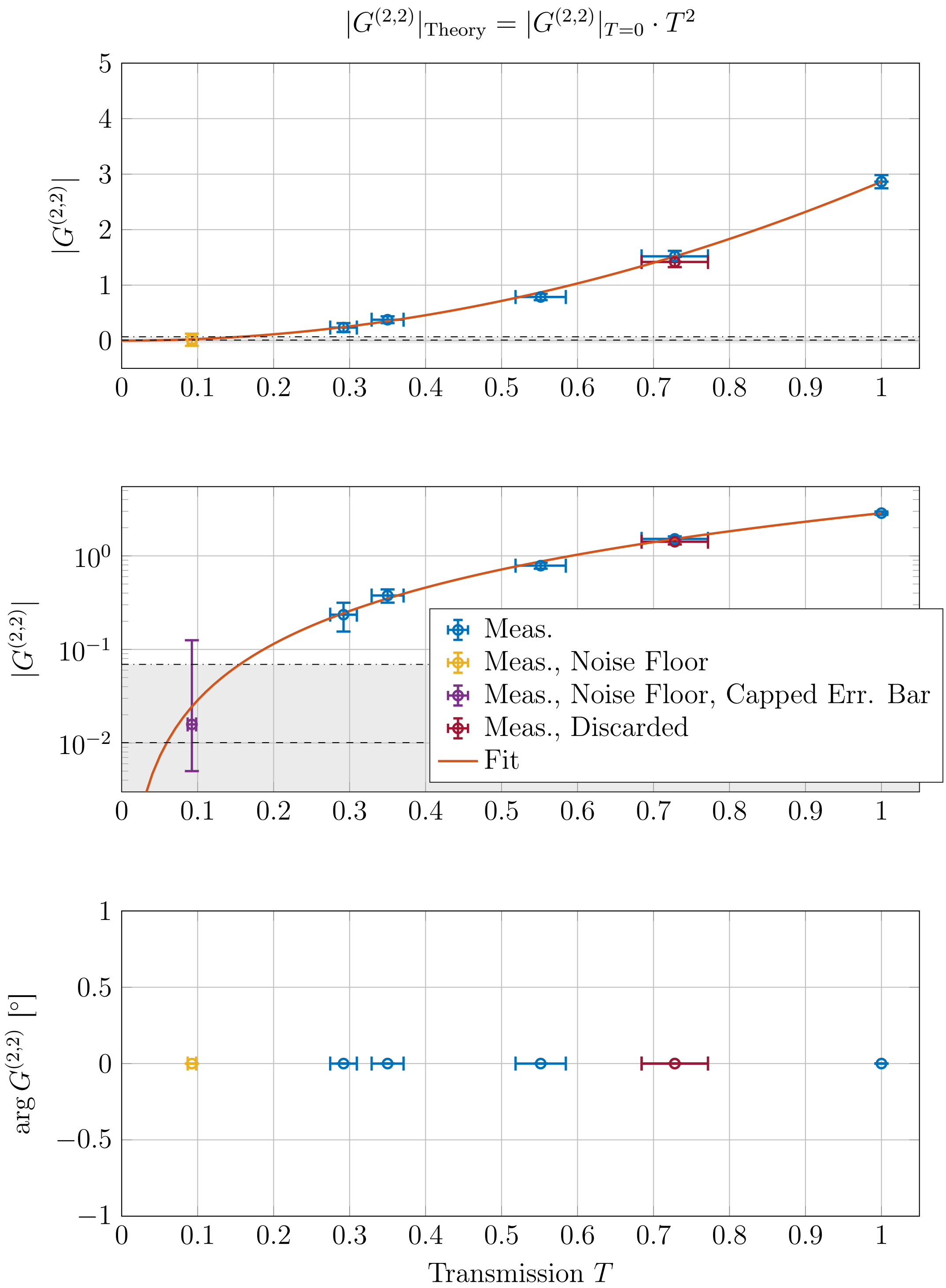

Figure C.8.: Bode plot of measured correlation moments $\mathcal{G}^{(2,2)}$ for a squeezed state and varied ND filter transmission T in signal beam. The grey area indicates the noise floor, with the dashed and dash-dotted line showing the expectation value and the upper confidence limit.

C.4. Correlation for Different Coherent States

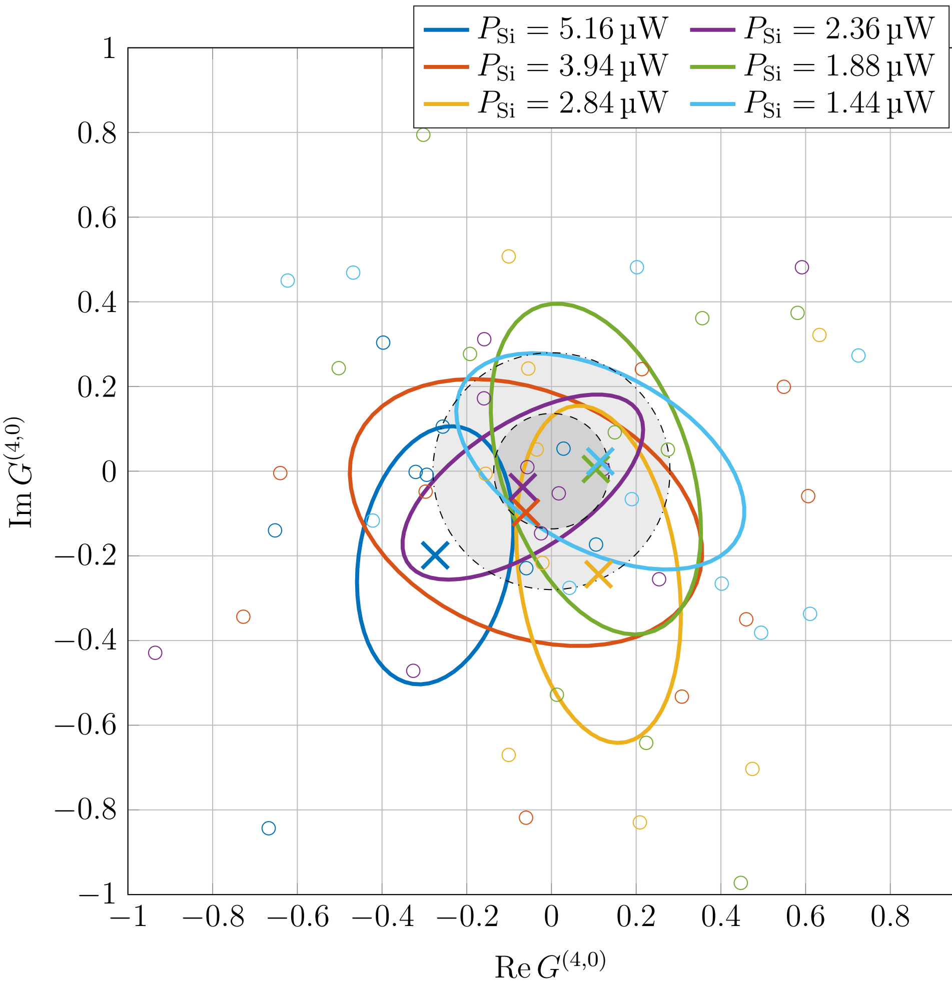

Figure C.9.: Scatter plot of measured correlation moments $\mathcal{G}^{(4,0)}$ for coherent states of varied power. Noise floor indicated by dark- and light grey circles at origin (expectation value and upper confidence limit).

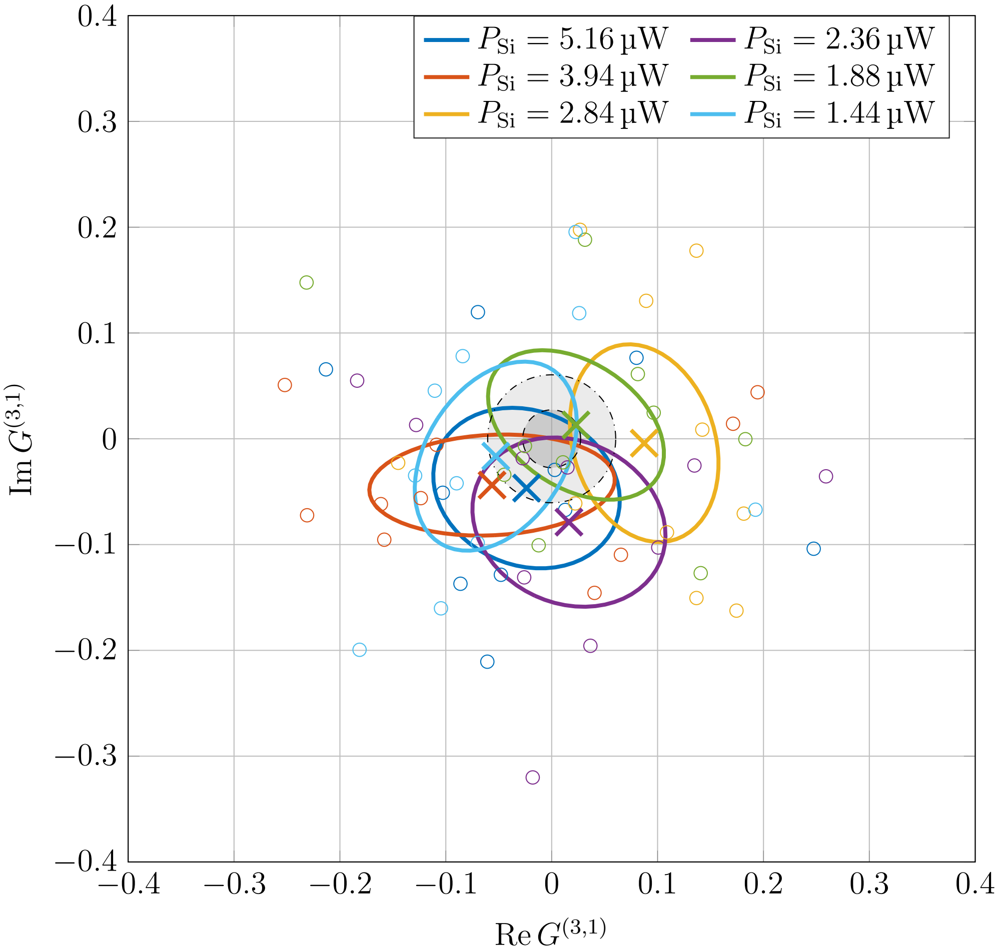

Figure C.10.: Scatter plot of measured correlation moments $\mathcal{G}^{(3,1)}$ for coherent states of varied power. Noise floor indicated by dark- and light grey circles at origin (expectation value and upper confidence limit).

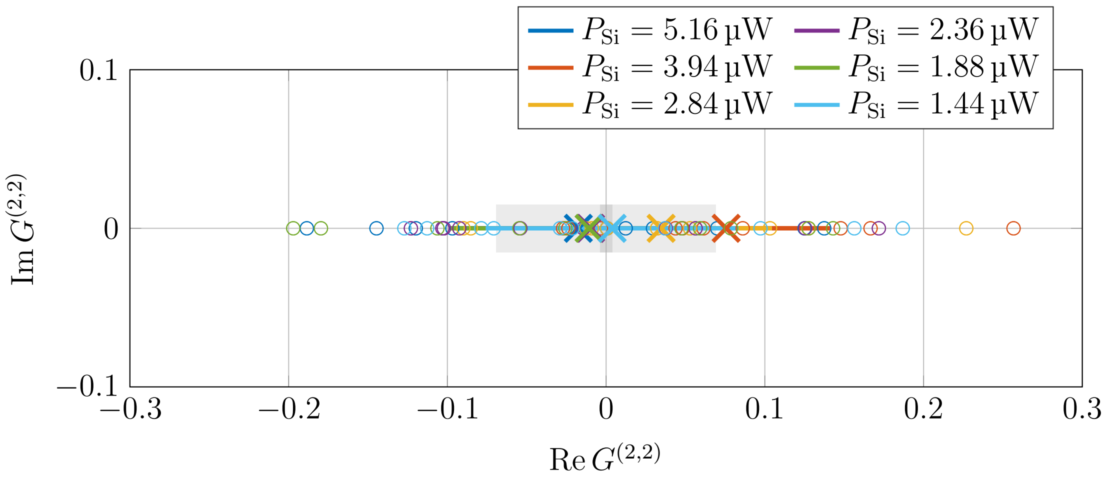

Figure C.11.: Scatter plot of measured correlation moments $\mathcal{G}^{(2,2)}$ for coherent states of varied power. Noise floor indicated by dark- and light grey rectangles at origin (expectation value and upper confidence limit). The noise floor is purely real and only drawn in 2D for better visibility.

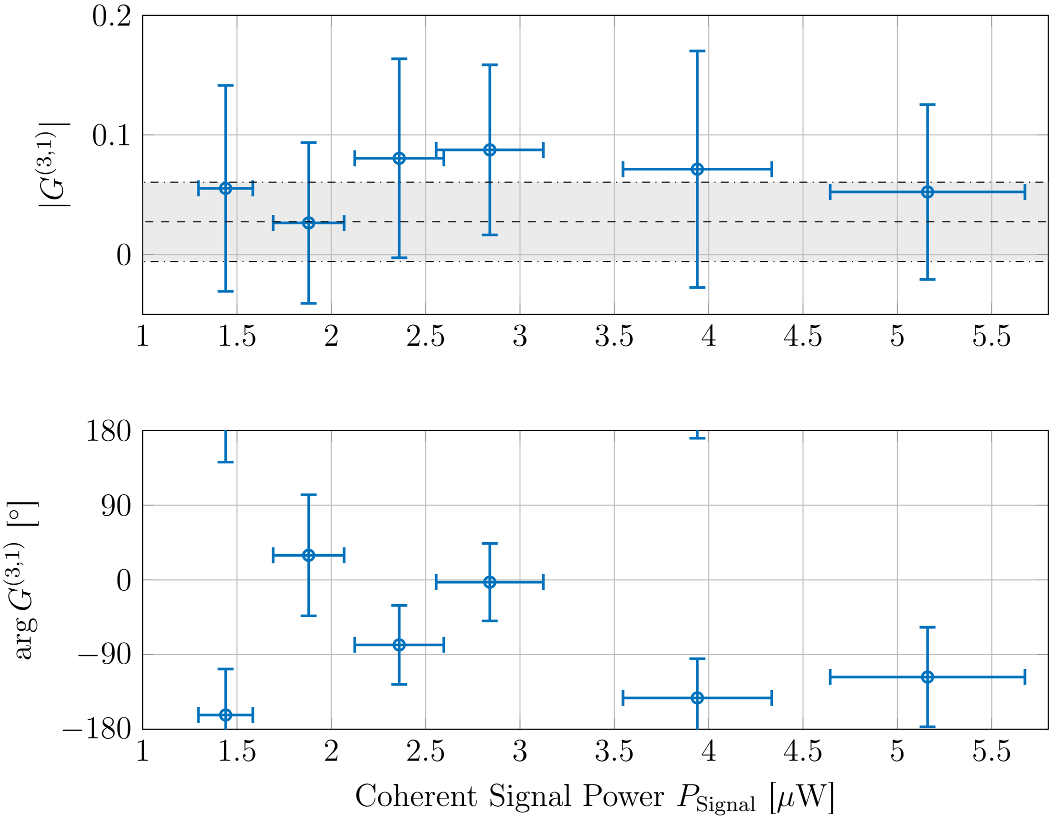

Figure C.12.: Bode plot of correlation moments $\mathcal{G}^{(3,1)}$ measured for coherent states of varied power. Phases wrap around ±180° margins. The grey area indicates the noise floor, with the dashed and dash-dotted line showing the expectation value and confidence limits.

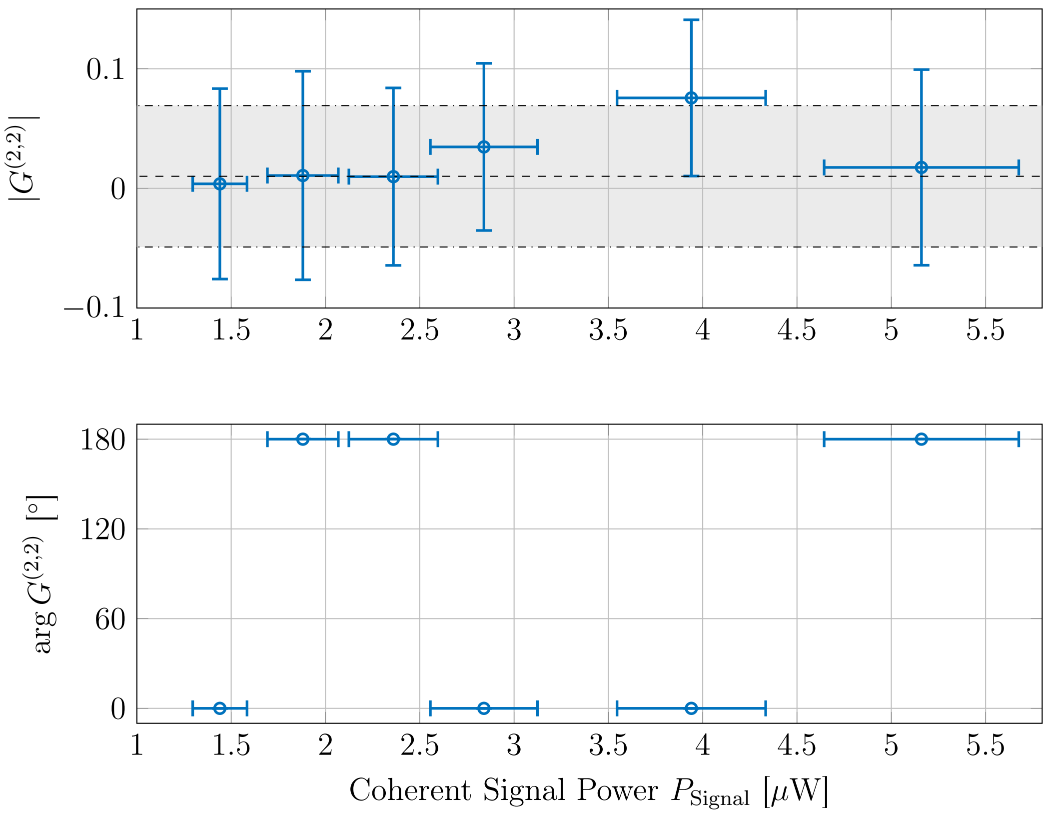

Figure C.13.: Bode plot of correlation moments $\mathcal{G}^{(2,2)}$ measured for coherent states of varied power. The grey area indicates the noise floor, with the dashed and dash-dotted line showing the expectation value and confidence limits.

D. Normally Ordered Quadrature Powers from BHD Measurements

In the theory on BHC (Sec. 2.6.1) we saw that the directly measured correlations between sets of detectors could be constructed into a function $F^{(k)}(\varphi)$, which is proportional to the normally ordered k-th moment of the quadrature operator, $\langle : \chi^k : \rangle$. We could then find the sought after even and odd ordered correlation functions from the normally ordered quadrature moment. Alternatively, however, we can find the normally ordered quadrature moments, and hence the correlation moments, directly from quadrature moments, which can be obtained from BHD measurements. We thank Andrii A. Semenov from the Bogolyubov Institute for Theoretical Physics in Kyiv for this suggestion. For the first order the quadrature operator is identical to the normally ordered quadrature operator

$$\hat{\chi}(\varphi) = \hat{a}e^{-i\varphi} + \hat{a}^\dagger e^{i\varphi} \equiv \, : \hat{\chi}(\varphi) : . \tag{D.1}$$

The normally ordered square of the quadrature operator is quickly found as

$$: \hat{\chi}^2(\varphi) : = \hat{\chi}^2(\varphi) - 1, \tag{D.2}$$

where we have used the commutator relation. Similar the third and fourth power of the quadrature operator in normal order are found as

$$: \hat{\chi}^3(\varphi) : = \hat{\chi}^3(\varphi) - 3\hat{\chi}(\varphi) \tag{D.3}$$

$$: \hat{\chi}^4(\varphi) : = \hat{\chi}^4(\varphi) - 6\hat{\chi}^2(\varphi) + 3. \tag{D.4}$$

Bibliography

[Aas+13] J. Aasi et al. “Enhanced Sensitivity of the LIGO Gravitational Wave Detector by Using Squeezed States of Light”. In: *Nature Photonics* 7.8 (Aug. 2013), pp. 613–619.

[Abb+16] B. P. Abbott et al. “Observation of Gravitational Waves from a Binary Black Hole Merger”. In: *Physical Review Letters* 116.6 (Feb. 11, 2016), p. 061102.

[AT92] G. S. Agarwal and K. Tara. “Nonclassical Character of States Exhibiting No Squeezing or Sub-Poissonian Statistics”. In: *Physical Review A* 46.1 (July 1, 1992), pp. 485–488.

[Agu+15] E. Agudelo, J. Sperling, W. Vogel, S. Köhnke, M. Mraz, and B. Hage. “Continuous Sampling of the Squeezed-State Nonclassicality”. In: *Physical Review A* 92.3 (Sept. 18, 2015), p. 033837.

[Ana11] Analog Devices Inc. *AD829 High Speed, Low Noise Video Op Amp Data Sheet*. 2011.

[BR19] Hans-Albert Bachor and Timothy C. Ralph. *A Guide to Experiments in Quantum Optics*. Third edition. Weinheim: Wiley-VCH, 2019. 565 pp.

[Bla01] Eric D. Black. “An Introduction to Pound–Drever–Hall Laser Frequency Stabilization”. In: *American Journal of Physics* 69.1 (Jan. 1, 2001), pp. 79–87.

[Boy08] Robert W. Boyd. *Nonlinear Optics*. 3rd ed. Amsterdam ; Boston: Academic Press, 2008. 613 pp.

[BW70] David C. Burnham and Donald L. Weinberg. “Observation of Simultaneity in Parametric Production of Optical Photon Pairs”. In: *Physical Review Letters* 25.2 (July 13, 1970), pp. 84–87.

[Car+00] H. J. Carmichael, H. M. Castro-Beltran, G. T. Foster, and L. A. Orozco. “Giant Violations of Classical Inequalities through Conditional Homodyne Detection of the Quadrature Amplitudes of Light”. In: *Physical Review Letters* 85.9 (Aug. 28, 2000), pp. 1855–1858.

[Cas+21] Catxere A. Casacio, Lars S. Madsen, Alex Terrasson, Muhammad Waleed, Kai Barnscheidt, Boris Hage, Michael A. Taylor, and Warwick P. Bowen. “Quantum-Enhanced Nonlinear Microscopy”. In: *Nature* 594.7862 (June 2021), pp. 201–206.

[Cav81] Carlton M. Caves. “Quantum-Mechanical Noise in an Interferometer”. In: *Physical Review D* 23.8 (Apr. 15, 1981), pp. 1693–1708.

[CLA01] N. J. Cerf, M. Lévy, and G. Van Assche. “Quantum Distribution of Gaussian Keys Using Squeezed States”. In: *Physical Review A* 63.5 (Apr. 18, 2001), p. 052311.

[Dav+96] K. M. Davis, K. Miura, N. Sugimoto, and K. Hirao. “Writing Waveguides in Glass with a Femtosecond Laser”. In: *Optics Letters* 21.21 (Nov. 1, 1996), pp. 1729–1731.

[DW87] Frank Diedrich and Herbert Walther. “Nonclassical Radiation of a Single Stored Ion”. In: *Physical Review Letters* 58.3 (Jan. 19, 1987), pp. 203–206.

[Dre+83] R. W. P. Drever, J. L. Hall, F. V. Kowalski, J. Hough, G. M. Ford, A. J. Munley, and H. Ward. “Laser Phase and Frequency Stabilization Using an Optical Resonator”. In: *Applied Physics B* 31.2 (June 1, 1983), pp. 97–105.

[Fos+00] G. T. Foster, L. A. Orozco, H. M. Castro-Beltran, and H. J. Carmichael. “Quantum State Reduction and Conditional Time Evolution of Wave-Particle Correlations in Cavity QED”. In: *Physical Review Letters* 85.15 (Oct. 9, 2000), pp. 3149–3152.

[Fos+02] G. T. Foster, W. P. Smith, J. E. Reiner, and L. A. Orozco. “Time-Dependent Electric Field Fluctuations at the Subphoton Level”. In: *Physical Review A* 66.3 (Sept. 16, 2002), p. 033807.

[Fra+61] P. A. Franken, A. E. Hill, C. W. Peters, and G. Weinreich. “Generation of Optical Harmonics”. In: *Physical Review Letters* 7.4 (Aug. 15, 1961), pp. 118–119.

[Fra+06] Alexander Franzen, Boris Hage, James DiGuglielmo, Jaromír Fiurášek, and Roman Schnabel. “Experimental Demonstration of Continuous Variable Purification of Squeezed States”. In: *Physical Review Letters* 97.15 (Oct. 13, 2006), p. 150505.

[Ger+09] S. Gerber, D. Rotter, L. Slodička, J. Eschner, H. J. Carmichael, and R. Blatt. “Intensity-Field Correlation of Single-Atom Resonance Fluorescence”. In: *Physical Review Letters* 102.18 (May 4, 2009), p. 183601.

[GK05] Christopher C. Gerry and Peter L. Knight. *Introductory Quantum Optics*. Cambridge, UK: Cambridge University Press, 2005.

[Gla63a] Roy J. Glauber. “The Quantum Theory of Optical Coherence”. In: *Physical Review* 130.6 (June 15, 1963), pp. 2529–2539.

[Gla63b] Roy J. Glauber. “Coherent and Incoherent States of the Radiation Field”. In: *Physical Review* 131.6 (Sept. 15, 1963), pp. 2766–2788.

[Göt22] Julian Göttsch. “Experimental Growth of Schrödinger Kitten States”. PhD thesis. Universität Hamburg, 2022.

[Gro+07] Nicolai B. Grosse, Thomas Symul, Magdalena Stobińska, Timothy C. Ralph, and Ping Koy Lam. “Measuring Photon Antibunching from Continuous Variable Sideband Squeezing”. In: *Physical Review Letters* 98.15 (Apr. 13, 2007), p. 153603.

[Gro+13] H. Grote, K. Danzmann, K. L. Dooley, R. Schnabel, J. Slutsky, and H. Vahlbruch. “First Long-Term Application of Squeezed States of Light in a Gravitational-Wave Observatory”. In: *Physical Review Letters* 110.18 (May 1, 2013), p. 181101.

[Hag+07] B. Hage, A. Franzen, J. DiGuglielmo, P. Marek, J. Fiurášek, and R. Schnabel. “On the Distillation and Purification of Phase-Diffused Squeezed States”. In: *New Journal of Physics* 9.7 (July 2007), p. 227.

[HJG52] R. Hanbury Brown, R. C. Jennison, and M. K. Das Gupta. “Apparent Angular Sizes of Discrete Radio Sources: Observations at Jodrell Bank, Manchester”. In: *Nature* 170.4338 (Dec. 1952), pp. 1061–1063.

[HT54] R. Hanbury Brown and R. Q. Twiss. “LXXIV. A New Type of Interferometer for Use in Radio Astronomy”. In: *The London, Edinburgh, and Dublin Philosophical Magazine and Journal of Science* 45.366 (July 1, 1954), pp. 663–682.

[HT56a] R. Hanbury Brown and R. Q. Twiss. “Correlation between Photons in Two Coherent Beams of Light”. In: *Nature* 177.4497 (Jan. 1956), pp. 27–29.

[HT56b] R. Hanbury Brown and R. Q. Twiss. “A Test of a New Type of Stellar Interferometer on Sirius”. In: *Nature* 178.4541 (Nov. 1956), pp. 1046–1048.

[Hei27] W. Heisenberg. “Über den anschaulichen Inhalt der quantentheoretischen Kinematik und Mechanik”. In: *Zeitschrift für Physik* 43.3 (Mar. 1, 1927), pp. 172–198.

[HOM87] C. K. Hong, Z. Y. Ou, and L. Mandel. “Measurement of Subpicosecond Time Intervals between Two Photons by Interference”. In: *Physical Review Letters* 59.18 (Nov. 2, 1987), pp. 2044–2046.

[Jäg15] Steve Jäger. “Konstruktion, Aufbau und Charakterisierung einer Quetschlichtquelle”. M.Sc. Thesis. Aug. 28, 2015.

[Jan32] K.G. Jansky. “Directional Studies of Atmospherics at High Frequencies”. In: *Proceedings of the Institute of Radio Engineers* 20.12 (Dec. 1932), pp. 1920–1932.

[Jan33] Karl G. Jansky. “Radio Waves from Outside the Solar System”. In: *Nature* 132.3323 (July 1933), pp. 66–66.

[Ken27] E. H. Kennard. “Zur Quantenmechanik einfacher Bewegungstypen”. In: *Zeitschrift für Physik* 44.4 (Apr. 1, 1927), pp. 326–352.

[Kie+09] T. Kiesel, W. Vogel, B. Hage, J. DiGuglielmo, A. Samblowski, and R. Schnabel. “Experimental Test of Nonclassicality Criteria for Phase-Diffused Squeezed States”. In: *Physical Review A* 79.2 (Feb. 27, 2009), p. 022122.

[KDM77] H. J. Kimble, M. Dagenais, and L. Mandel. “Photon Antibunching in Resonance Fluorescence”. In: *Physical Review Letters* 39.11 (Sept. 12, 1977), pp. 691–695.

[Kow+05] A. M. Kowalevicz, V. Sharma, E. P. Ippen, J. G. Fujimoto, and K. Minoshima. “Three-Dimensional Photonic Devices Fabricated in Glass by Use of a Femtosecond Laser Oscillator”. In: *Optics Letters* 30.9 (May 1, 2005), pp. 1060–1062.

[Kri+08] Leonid A. Krivitsky, Ulrik L. Andersen, Ruifang Dong, Alexander Huck, Christoffer Wittmann, and Gerd Leuchs. “Electronic Noise-Free Measurements of Squeezed Light”. In: *Optics Letters* 33.20 (Oct. 15, 2008), pp. 2395–2397.

[Kri+09] Leonid A. Krivitsky, Ulrik L. Andersen, Ruifang Dong, Alexander Huck, Christoffer Wittmann, and Gerd Leuchs. “Correlation Measurement of Squeezed Light”. In: *Physical Review A* 79.3 (Mar. 18, 2009), p. 033828.

[Küh+17] B. Kühn, W. Vogel, M. Mraz, S. Köhnke, and B. Hage. “Anomalous Quantum Correlations of Squeezed Light”. In: *Physical Review Letters* 118.15 (Apr. 10, 2017), p. 153601.

[Lai+22] K. Laiho, T. Dirmeier, M. Schmidt, S. Reitzenstein, and C. Marquardt. “Measuring Higher-Order Photon Correlations of Faint Quantum Light: A Short Review”. In: *Physics Letters A* 435 (May 30, 2022), p. 128059.

[LO05] Brahim Lounis and Michel Orrit. “Single-Photon Sources”. In: *Reports on Progress in Physics* 68.5 (Apr. 2005), p. 1129.

[Mad+12] Lars S. Madsen, Vladyslav C. Usenko, Mikael Lassen, Radim Filip, and Ulrik L. Andersen. “Continuous Variable Quantum Key Distribution with Modulated Entangled States”. In: *Nature Communications* 3.1 (Sept. 25, 2012), p. 1083.

[Mai60] T. H. Maiman. “Stimulated Optical Radiation in Ruby”. In: *Nature* 187.4736 (Aug. 1960), pp. 493–494.

[Man79] L. Mandel. “Sub-Poissonian Photon Statistics in Resonance Fluorescence”. In: *Optics Letters* 4.7 (July 1, 1979), pp. 205–207.

[Mar+16] Kevin Marshall, Christian S. Jacobsen, Clemens Schäfermeier, Tobias Gehring, Christian Weedbrook, and Ulrik L. Andersen. “Continuous-Variable Quantum Computing on Encrypted Data”. In: *Nature Communications* 7.1 (Dec. 14, 2016), p. 13795.

[MR97] D. F. McAlister and M. G. Raymer. “Ultrafast Photon-Number Correlations from Dual-Pulse, Phase-Averaged Homodyne Detection”. In: *Physical Review A* 55.3 (Mar. 1, 1997), R1609–R1612.

[Mic+00] P. Michler, A. Kiraz, C. Becher, W. V. Schoenfeld, P. M. Petroff, Lidong Zhang, E. Hu, and A. Imamoglu. “A Quantum Dot Single-Photon Turnstile Device”. In: *Science* 290.5500 (Dec. 22, 2000), pp. 2282–2285.

[Miu+97] K. Miura, Jianrong Qiu, H. Inouye, T. Mitsuyu, and K. Hirao. “Photowritten Optical Waveguides in Various Glasses with Ultrashort Pulse Laser”. In: *Applied Physics Letters* 71.23 (Dec. 8, 1997), pp. 3329–3331.

[Nat04] National Instruments. *NI 6132/6133 Specifications*. 2004.

[Nat11] National Instruments. *NI FlexRIO FPGA Module Installation Guide and Specifications*. 2011.

[Nat15] National Instruments. *NI 5751/5751B Device Specifications*. 2015.

[Nat17] National Instruments. *PXI-5152 Specifications*. 2017.

[Nat24] National Instruments. *LabVIEW FPGA Module User Manual*. 2024.

[Nee+06] J. S. Neergaard-Nielsen, B. Melholt Nielsen, C. Hettich, K. Mølmer, and E. S. Polzik. “Generation of a Superposition of Odd Photon Number States for Quantum Information Networks”. In: *Physical Review Letters* 97.8 (Aug. 25, 2006), p. 083604.

[OSu+08] Malcolm N. O'Sullivan, Kam Wai Clifford Chan, Vasudevan Lakshminarayanan, and Robert W. Boyd. "Conditional Preparation of States Containing a Definite Number of Photons". In: *Physical Review A* 77.2 (Feb. 5, 2008), p. 023804.

[OHM87] Z. Y. Ou, C. K. Hong, and L. Mandel. "Detection of Squeezed States by Cross Correlation". In: *Physical Review A* 36.1 (July 1, 1987), pp. 192–196.

[Our+06] Alexei Ourjoumtsev, Rosa Tualle-Brouri, Julien Laurat, and Philippe Grangier. "Generating Optical Schrödinger Kittens for Quantum Information Processing". In: *Science* 312.5770 (Apr. 7, 2006), pp. 83–86.

[Ric96] Th. Richter. "Determination of Field Correlation Functions from Measured Quadrature Component Distributions". In: *Physical Review A* 53.2 (Feb. 1, 1996), pp. 1197–1199.

[Rob29] H. P. Robertson. "The Uncertainty Principle". In: *Physical Review* 34.1 (July 1, 1929), pp. 163–164.

[ST19] Bahaa E. A. Saleh and Malvin Carl Teich. *Fundamentals of Photonics*. Third edition. Wiley Series in Pure and Applied Optics. Hoboken, NJ: Wiley, 2019. 2 pp.

[San+02] Charles Santori, David Fattal, Jelena Vučković, Glenn S. Solomon, and Yoshihisa Yamamoto. "Indistinguishable Photons from a Single-Photon Device". In: *Nature* 419.6907 (Oct. 2002), pp. 594–597.

[ST58] A. L. Schawlow and C. H. Townes. "Infrared and Optical Masers". In: *Physical Review* 112.6 (Dec. 15, 1958), pp. 1940–1949.

[Sch26] E. Schrödinger. "Der stetige Übergang von der Mikro- zur Makromechanik". In: *Naturwissenschaften* 14.28 (July 1, 1926), pp. 664–666.

[Sch+15] Carsten H. H. Schulte, Jack Hansom, Alex E. Jones, Clemens Matthiesen, Claire Le Gall, and Mete Atatüre. "Quadrature Squeezed Photons from a Two-Level System". In: *Nature* 525.7568 (Sept. 2015), pp. 222–225.

[SYM79] J. Shapiro, H. Yuen, and A. Mata. "Optical Communication with Two-Photon Coherent States–Part II: Photoemissive Detection and Structured Receiver Performance". In: *IEEE Transactions on Information Theory* 25.2 (Mar. 1979), pp. 179–192.

[SRV05] E. Shchukin, Th. Richter, and W. Vogel. "Nonclassicality Criteria in Terms of Moments". In: *Physical Review A* 71.1 (Jan. 26, 2005), p. 011802.

[SV06] E. Shchukin and W. Vogel. “Universal Measurement of Quantum Correlations of Radiation”. In: *Physical Review Letters* 96.20 (May 22, 2006), p. 200403.

[SV05] E. V. Shchukin and W. Vogel. “Nonclassical Moments and Their Measurement”. In: *Physical Review A* 72.4 (Oct. 12, 2005), p. 043808.

[Slu$^+$85] R. E. Slusher, L. W. Hollberg, B. Yurke, J. C. Mertz, and J. F. Valley. “Observation of Squeezed States Generated by Four-Wave Mixing in an Optical Cavity”. In: *Physical Review Letters* 55.22 (Nov. 25, 1985), pp. 2409–2412.

[Spa$^+$13] Nicolò Spagnolo, Chiara Vitelli, Lorenzo Aparo, Paolo Mataloni, Fabio Sciarrino, Andrea Crespi, Roberta Ramponi, and Roberto Osellame. “Three-Photon Bosonic Coalescence in an Integrated Tritter”. In: *Nature Communications* 4.1 (Mar. 19, 2013), p. 1606.

[SB01] Alexander M. Streltsov and Nicholas F. Borrelli. “Fabrication and Analysis of a Directional Coupler Written in Glass by Nanojoule Femtosecond Laser Pulses”. In: *Optics Letters* 26.1 (Jan. 1, 2001), pp. 42–43.

[SN10] Alexander Szameit and Stefan Nolte. “Discrete Optics in Femtosecond-Laser-Written Photonic Structures”. In: *Journal of Physics B: Atomic, Molecular and Optical Physics* 43.16 (July 2010), p. 163001.

[vLWG07] Peter van Loock, Christian Weedbrook, and Mile Gu. “Building Gaussian Cluster States by Linear Optics”. In: *Physical Review A* 76.3 (Sept. 21, 2007), p. 032321.

[Vog91] Werner Vogel. “Squeezing and Anomalous Moments in Resonance Fluorescence”. In: *Physical Review Letters* 67.18 (Oct. 28, 1991), pp. 2450–2452.

[Vog95] Werner Vogel. “Homodyne Correlation Measurements with Weak Local Oscillators”. In: *Physical Review A* 51.5 (May 1, 1995), pp. 4160–4171.

[Vog08] Werner Vogel. “Nonclassical Correlation Properties of Radiation Fields”. In: *Physical Review Letters* 100.1 (Jan. 11, 2008), p. 013605.

[VW06] Werner Vogel and Dirk-Gunnar Welsch. *Quantum Optics*. 3rd, revised and extended ed. Weinheim: Wiley-VCH, 2006.

[WM08] D. F. Walls and G. J. Milburn. *Quantum Optics*. 2nd ed. Berlin: Springer, 2008. 425 pp.

[Wei+96] Gregor Weihs, Michael Reck, Harald Weinfurter, and Anton Zeilinger. "Two-Photon Interference in Optical Fiber Multiports". In: *Physical Review A* 54.1 (July 1, 1996), pp. 893–897.

[Wu+86] Ling-An Wu, H. J. Kimble, J. L. Hall, and Huifa Wu. "Generation of Squeezed States by Parametric Down Conversion". In: *Physical Review Letters* 57.20 (Nov. 17, 1986), pp. 2520–2523.

[Yok+13] Shota Yokoyama, Ryuji Ukai, Seiji C. Armstrong, Chanond Sornphiphatphong, Toshiyuki Kaji, Shigenari Suzuki, Jun-ichi Yoshikawa, Hidehiro Yonezawa, Nicolas C. Menicucci, and Akira Furusawa. "Ultra-Large-Scale Continuous-Variable Cluster States Multiplexed in the Time Domain". In: *Nature Photonics* 7.12 (Dec. 2013), pp. 982–986.

[Yue76] Horace P. Yuen. "Two-Photon Coherent States of the Radiation Field". In: *Physical Review A* 13.6 (June 1, 1976), pp. 2226–2243.

[YC83] Horace P. Yuen and Vincent W. S. Chan. "Noise in Homodyne and Heterodyne Detection". In: *Optics Letters* 8.3 (Mar. 1, 1983), pp. 177–179.

Selbstständigkeitserklärung

Ich versichere hiermit an Eides statt, dass ich die vorliegende Arbeit selbstständig angefertigt und ohne fremde Hilfe verfasst habe. Dazu habe ich keine außer den von mir angegebenen Hilfsmitteln und Quellen verwendet und die den benutzten Werken inhaltlich und wörtlich entnommenen Stellen habe ich als solche kenntlich gemacht.

Rostock, 17. April 2025